UNIVERSIDADE TÉCNICA DE LISBOA

INSTITUTO SUPERIOR TÉCNICO

Velocity Reconstruction with the RICH detector of the AMS experiment

João Manuel Roseira Borges

(Licenciado)

Dissertação para obtenção do Grau de Mestre em Física

Orientador: Doutor Fernando José de Carvalho Barão

Constituição do Júri:

Presidente:

Doutor Mário João Martins Pimenta

Vogais:

Doutora Amélia Maio

Doutor João Seixas

Doutor Fernando José de Carvalho Barão

Lisboa, Novembro de 2003

Resumo

A experiência AMS visa instalar na estação espacial Internacional (ISS) um espectrómetro magnético de massa para estudar os raios cósmicos primários de energia média, fora da presença da atmosfera terrestre. Prevê-se que a experiência - presentemente ainda em fase de preparação - comece a funcionar pelo início de 2006. Esta experiência constitui um novo passo na investigação de domínios interdisciplinares entre a Astrofísica e a Física das Partículas Elementares.

O espectrómetro de AMS incluirá um detector de Cherenkov de imagem anelar (RICH - Ring Imaging Cherenkov), o qual visa medir com grande precisão a velocidade relativistíca das partículas com carga eléctrica que compõem os raios cósmicos; o objectivo é ter-se um erro de cerca de 0.1% no caso mais desfavorável.

Esta precisão na medida da velocidade será determinante para se levar a cabo o desejado refinamento nas medidas existentes da composição em espécies elementares e isotópicas do espectro dos raios cósmicos. Estas medições revestem-se de grande importância para a compreensão dos mecanismos de produção e propagação dos raios cósmicos que continuam envoltos em algum mistério.

O detector RICH também contribuirá para se alcançar a sensibilidade pretendida de 10^{-9} na procura de núcleos de antimatéria. Essa busca passa essencialmente pela medição do *ratio* de abundâncias $\frac{\overline{He}}{He}$. Esta pesquisa constitui aliás um dos principais objectivos da experiência, que poderia muito bem derivar o seu nome do acrónimo de "Antimatter Magnetic Spectrometer" em vez do oficial "Alpha Magnetic Spectrometer".

Nesta tese, apresenta-se um método de reconstrução da velocidade para este detector RICH de AMS. O método assenta no ajuste dum padrão (curva plana não análitica) aos pontos de detecção dos fotões de Cherenkov. Esse ajuste é baseado no método estatístico conhecido por *Máxima Verosimilhança*. A descrição do método encontra-se essencialmente feita no capítulo 3. O algoritmo foi codificado num

software de análise que foi testado com dados gerados por uma simulação, mas também com dados recolhidos por um protótipo do detector RICH. Esses resultados encontram-se expostos nos capítulos 4 e 5.

Palavras chave: RICH, ângulo/padrão/anel de Cherenkov, reconstrução, função Verosimilhnça, resolução de velocidade

Abstract

The AMS experiment - currently in preparation - will install a magnetic spectrometer in the International Space Station (ISS) by the year of 2006. This experiment will then be able to perform mass spectrometry of the electrically charged particles composing the primary cosmic rays of medium energy. This will be achieved by using the most complete spectrometer dedicated to cosmic rays, and for the first time, working out of the atmosphere's environment. Joining research fields like astrophysics and particle physics, AMS represents a new challenge to multidisciplinarity.

The AMS instrumentation includes a Ring Cherenkov detector (RICH). This detector has the role of measuring with very high accuracy the velocity of the charged particle cosmic rays; the goal is to achieve a relative error upper limit of 0.1%.

This high resolution will be determinant for the purpose of refining the knowledge of the elemental and isotopic spectrum composition of the cosmic rays. These spectrum measurements are important to develop the understanding of the production and propagation of the cosmic rays, still barely known. The RICH detector will also contribute to reach the AMS proposed sensitivity of 10^{-9} for the antimatter search. The relevance of this issue is such that even the acronym name AMS may as well stand for *Antimatter Magnetic Spectrometer* as for the official *Alpha Magnetic Spectrometer* - the ISS was before named the Alpha Space Station.

This thesis deals with the task of the velocity reconstruction on the RICH detector of AMS. A reconstruction algorithm was developed and is here presented. This reconstruction is based on a planar curve pattern fit to the hit points of the detected Cherenkov photons. The fit relies on the Statistical parameter estimation technique known as *Maximum Likelihood approach*. The algorithm is described on chapter 3. A reconstruction software has been codified with this algorithm and tested with both simulated and real data, these last taken by some of the earliest data runs of the RICH prototype. The results are exposed on chapters 4 and 5.

Keywords: RICH, Cherenkov angle/pattern/ring, reconstruction, Likelihood function, velocity resolution

Contents

Resumo **i**

Abstract **iii**

Contents **v**

List of Figures **vii**

List of Tables **xiii**

1 The AMS experiment **1**

1.1 Physics Goals of the AMS experiment 2

1.2 The instrumentation of AMS 5

2 The RICH detector of AMS **11**

2.1 The Cherenkov Radiation 11

2.2 Detector Setup - general properties 15

2.3 Cherenkov angle uncertainty in the RICH detector 22

2.3.1 chromaticity 24

2.3.2 radiator thickness and pixel size 30

3 The reconstruction algorithm **41**

3.1 The Reconstruction method 41

3.1.1 Pattern fit 41

3.1.2 Likelihood approach 49

3.2 Additional remarks and optimization of the reconstruction 57

3.2.1 The hits of the particle in the Light Guide 57

3.2.2 Photon emission point 59

3.3 Bayes Theorem and the Maximum Likelihood method 66

4 Application to the simulated Flight Setup 69

5 Analysis of data collected with the RICH prototype 77

5.1 The RICH Prototype setup 77

5.2 PMT signal and Noisy channels 80

5.3 Alignment of the prototype elements 84

5.3.1 Wire chambers inter-alignment 84

5.3.2 Alignment of the Wire chambers with the PMT matrix 88

5.4 Event selection 90

5.5 Reconstruction Results 95

5.5.1 The cosmic muons spectrum 95

5.5.2 Reconstructions selection (Kolmogorov test to the azimuthal hits distribution) 97

5.5.3 Velocity resolution results 103

5.6 Light Yield 109

Conclusions 117

A Refraction effect on the θ_c geometrical resolution 119

B Photon's crossed distance inside RICH radiator 121

References 123

List of Figures

1.1 Artistic view of the ISS Space Station with AMS aboard. 1
1.2 CR total energy spectrum [1] 2
1.3 Schematic draw of the AMS02 spectrometer mounted on the support structure (USS) 6
1.4 Exploded view of the AMS02 spectrometer. 7

2.1 Illustration of the Cherenkov shock wave effect 12
2.2 Dependence of the Cherenkov angle with the velocity 13
2.3 Plot of the sensitivity factors ratio $\frac{\tan\theta_c\,(n=1.334)}{\tan\theta_c\,(n=1.03)}$. 14
2.4 Perspective and side-view of the RICH detector 15
2.5 The R7600-M16 Hamamatsu PMT. 18
2.6 R7600-M16 PMT quantum efficiency spectrum. 18
2.7 PMT housing plus light guide. 19
2.8 Schematic draw of the RICH light guides 19
2.9 RICH acceptance versus AMS acceptance 20
2.10 Fraction of reflected and detected photons. 21
2.11 Fraction of the photons reaching the detection matrix suffering Rayleigh scattering photons, for two different clarities. 23
2.12 Spatial illustration of the background noise on the PMT readout matrix, due to the Rayleigh scattering 24
2.13 Chromatic dispersion of the NaF radiator. 25
2.14 Wavelength spectrum of the Cherenkov photons (at emission and detection). 26
2.15 The effect of the chromaticity on NaF 27
2.16 The chromatic dispersion of the 1.03 Aerogel radiator. 27
2.17 The effect of the chromaticity on AgL (n=1.03) 28

2.18 Illustration of the dependence of the chromaticity uncertainty on the velocity (equivalent to the mean Cherenkov angle) for the NaF radiator. 28
2.19 RMS for the θ_c chromaticity spectra versus velocity 29
2.20 Illustration of the reconstructed chromatic uncertainty as a larger uncertainty than the intrinsic one. 29
2.21 Cherenkov ring width due to the radiator thickness in case of vertical incidence. 30
2.22 Dispersion of the detected points for the Cherenkov photons at the detection level plane (1-D and 2-D) 33
2.23 Uncertainty of the reconstructed Cherenkov angle ($\theta_c^{\rm rec}$) due to geometrical uncertainty sources only as function of the particle velocity. . 34
2.24 Uncertainty on the Cherenkov reconstructed angle for a vertical incidence of the particle 35
2.25 Single hit relative error on the reconstructed velocity 36
2.26 Effect of the radiator thickness in the case of non-vertical incidence. . 37
2.27 Triangle used to compute the width of the Cherenkov ring due to the radiator thickness 38
2.28 Thickness of the ring as function of the azimuthal angle φ 39
2.29 Average ring thickness as function of the particle polar angle and as function of the Cherenkov angle. 39

3.1 Schematic illustration of the fit. Pattern associated with $\theta_c = \theta_2$ describes better the detected points than θ_1 pattern. 41
3.2 Illustration of the photon tracing 42
3.3 Illustration of the two frames involved in the photon tracing 43
3.4 Two patterns for the same particle kinematics, corresponding to Aerogel and NaF radiators 44
3.5 Illustration of two possible distances between the hits and the Cherenkov pattern 45
3.6 Graphic of the azimuthal distance pattern-hit (1) 46
3.7 Graphic of the azimuthal distance pattern-hit (2) 47
3.8 A visual illustration of the hits spreading in the RICH PMT matrix of AMS 48

3.9 Hits residuals (to expected pattern) for 5000 simulated events in all AMS acceptance 51
3.10 Residuals histogram (same of figure 3.9), here normalized to the unit, with the likelihood p.d.f. plotted on top of it. 54
3.11 "zoom out" to fig 3.10 54
3.12 (Top figure) Likelihood merit function for the event of fig. 3.6. (Bottom fig.) Chi-squared merit function for a cut-off of 5 *cm* for the same event. 56
3.13 The Cherenkov photons radiated in the light guides don't give rise to a geometrical and reconstructible pattern. 58
3.14 Effect of the particle hits on the pattern fit 58
3.15 Illustration of the emission point effect on θ_c reconstruction 59
3.16 Dependence of the systematic error (on reconstructed θ_c) on the emission point (AgL radiator) 60
3.17 Comparison between the dependence of the systematic error on ${\theta_c}^{rec}$ on the used Cherenkov vertex, and the nearly total independence of the statistical error. 61
3.18 Origin z coordinate distribution for the detected photons on the simulation (Aerogel radiator) 62
3.19 Dependence of the systematic error (on the reconstructed θ_c) on the used emission point (NaF radiator). 63
3.20 Comparison of the sensitivity of the systematic error absolute value with the insensitivity of the statistical error on the used emission point. 64
3.21 Origin z coordinate distribution for the detected photons on the simulation (NaF radiator) 65

4.1 Distributions of residuals for Aerogel and NaF, both normalized to the unit. 70
4.2 Residuals distribution for NaF with the adopted Likelihood p.d.f. superimposed. 70
4.3 Number of hits on reconstructed pattern 71
4.4 Reconstructed θ_c histograms – Heliums 10 GeV/c/nuc 72
4.5 Histograms of $(\theta_c^{\rm rec} - \theta_c^{\rm sim})$ for Heliums 10 GeV/c/nuc 72

4.6 *Single hit* θ_c resolutions for Heliums 10 GeV/c/nuc 73
4.7 *Single hit* β relative resolutions for Heliums 10 GeV/c/nuc 73
4.8 Reconstructed θ_c as function of momentum per nucleon 74
4.9 Systematic error on $\theta_c{}^{rec}$ versus momentum per nucleon of the particle. *Left Plot:* Aerogel radiator result. *Right Plot:* NaF result. . . . 75
4.10 Comparison of the single-hit θ_c resolutions and relative resolution on β for the two radiators in analysis. 75

5.1 Prototype and Flight setup PMT matrices. 77
5.2 Schema of the prototype setup 78
5.3 Pedestal ADC signal for 16 channels of PMT # 1 (pedestal run 11). . 81
5.4 Spatial analysis for the pixel PMT channel occupancy (or firing) frequency 82
5.5 PMT channel occupancy frequency analysis 83
5.6 Residuals distributions used to inter-align the 3 wire chambers on run 10 85
5.7 Illustration of the misalignment between the wire chambers. 86
5.8 Event display for event 217 of run 27 88
5.9 Event display for event 480 of run 27 89
5.10 χ^2 distribution of the linear fit to the particle tracks. 90
5.11 The prototype polar angle acceptance has its maximum about 4 to 5 Degree. 90
5.12 Distribution of the matching residuals between particle track and particle cluster. 91
5.13 Efficiency of the track-(particle signal) matching criterion 91
5.14 Highest pixel signal for the *matching* and *non matching* populations . 93
5.15 Highest integrated PMT signal for the *matching* and *non matching* populations 93
5.16 Efficiency of particle selecting criterion using highest pixel PMT signal 94
5.17 Efficiency of particle selecting criterion using highest integrated PMT signal 94
5.18 Cosmic Muons momentum spectrum at sea level (12^o North latitude) 95
5.19 Cosmic Muons velocity spectrum at sea level (12^o North latitude) . . 95
5.20 *Multi-radiator* configuration runs mapping 96

5.21 Two resulting muons velocity spectra, used to identify the tiles of the *Multi-radiator* configuration runs 97
5.22 Odd reconstructed rings. 98
5.23 A nice Cherenkov ring. 99
5.24 Distribution of the compatibility-Kolmogorov-test probabilities for the reconstructions of runs 12 and 27. 99
5.25 Two samples of the reconstructed velocity spectrum selected by a Kolmogorov probability lower than 5×10^{-4} and 5×10^{-3} (respectively for the histograms of left and right). 100
5.26 Increase of the compatibility with the reference spectrum as the Kolmogorov-test probability upper limit is increased. 101
5.27 Chi-square test result used to establish the Kolmogorov test probability cut value (bellow which value we reject a Cherenkov reconstruction). 102
5.28 Distributions of the number of hits for the reconstructed Cherenkov rings with low and high Kolmogorov test probability. 103
5.29 Single hit velocity resolution estimation for summed data of runs 12 and 27 (n=1.03(3cm thick.),drift=41.65cm) 104
5.30 Single hit velocity resolution estimation for summed data of runs 15 and 16 (n=1.05(2cm thick.),drift=41.65cm) 104
5.31 Single-hit resolutions for the analyzed aerogel runs. 105
5.32 Resolutions for the analyzed aerogel runs. 105
5.33 Pattern fit residuals distributions. Left: runs 12-27 (AgL 1.03 - MC plus data). Right: runs 15-16 (AgL 1.05 - MC plus data) 107
5.34 Number of hits for two acceptance-velocity configurations and respective Poisson fits(data runs 12-27). 110
5.35 Mean number of hits for different acceptances of run 12-27 (data) . . 111
5.36 Results for the light yield estimator for the different radiators. 111
5.37 Fits to the ring hits counting distributions for the data runs, using model of eq. 5.1. 112
5.38 Efficiency of having at least 3 hits (result for the different radiators obtained by the fit of eq. 5.1). 114
5.39 Palette of scatter-plots "Ring acceptance (in y scale) versus $\beta_{\rm rec}$" for all the data runs. 116

A.1 Effect of the refraction on the radius of the Cherenkov ring for a vertical particle incidence. 120
A.2 Effect of refraction on the θ_c geometrical resolution. 120

B.1 Distance crossed by a photon emitted at the top of the radiator inside it. 122

List of Tables

3.1 $\theta_c^{\rm rec}$ systematic error due to the emission point (Aerogel radiator) . . 61

3.2 θ_c systematic error due to the emission point (NaF radiator) 64

5.1 Summary of the cosmic runs processed for this thesis 79

5.2 Summary of the rejected channels during the cosmic runs 83

5.3 Prototype components misalignments during the cosmic runs. 87

5.4 Pattern fit residuals for the cosmic runs 107

5.5 Velocity single hit resolution estimation for the cosmic runs 108

5.6 Velocity resolution estimation for the cosmic runs 108

5.7 Light Yield table summary. 113

Chapter 1

The AMS experiment

The AMS (Alpha or Antimatter Magnetic Spectrometer) experiment [2, 3] is the first cosmic rays experiment taking place in terrestrial orbit with a magnetic spectrometer. Its purpose is to detect the primary cosmic rays outside of the atmosphere background environment. To achieve this goal, the AMS collaboration will install its detector aboard of the International Space Station (ISS) which orbits the earth at an average altitude of about 400 km.

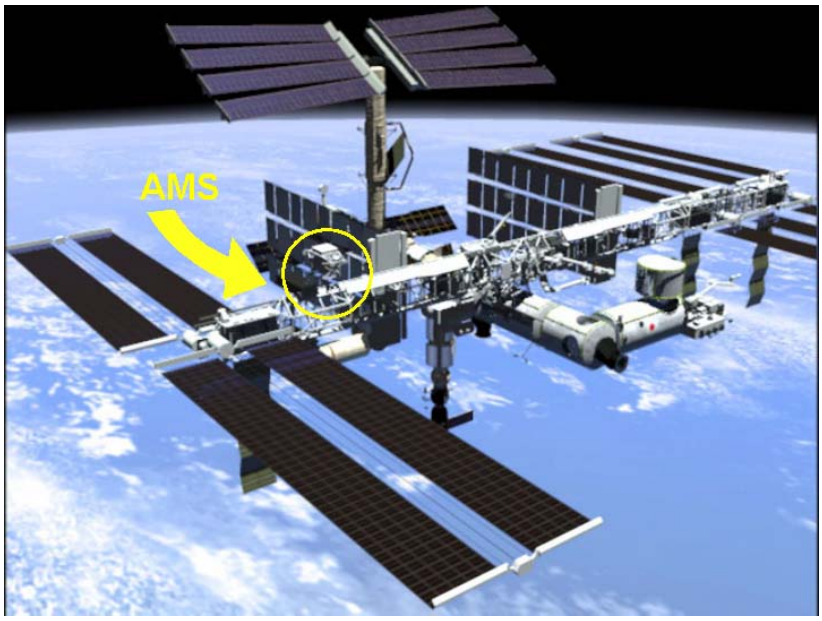

Figure 1.1: *Artistic view of the ISS Space Station with AMS aboard.*

The experiment time duration is foreseen to be at least 3 years, what is enough to set AMS as a new step in the cosmic rays experiments. The beginning of the

experiment is foreseen for the year of 2006.

The AMS experiment is currently being prepared by a vast international collaboration leaded by the Physics Nobel prize S. Ting. The experiment has also the fundamental support of the U.S. NASA corporation, that is responsible to carry the detector and to install it aboard of the ISS.

1.1 Physics Goals of the AMS experiment

Cosmic rays (CR) are fully ionized nuclei, protons being the most abundant – about 90% – followed by helium nuclei and electrons, with all the remaining elements and most of the isotopes also present. Energetic photons and neutrinos are also part of this cosmic flux.

The energy range spanned by these particles is one of the most amazing physical phenomena, where several magnitude orders are crossed since some hundreds of MeV up to $10^{20}\,eV$ as showed in figure 1.2.

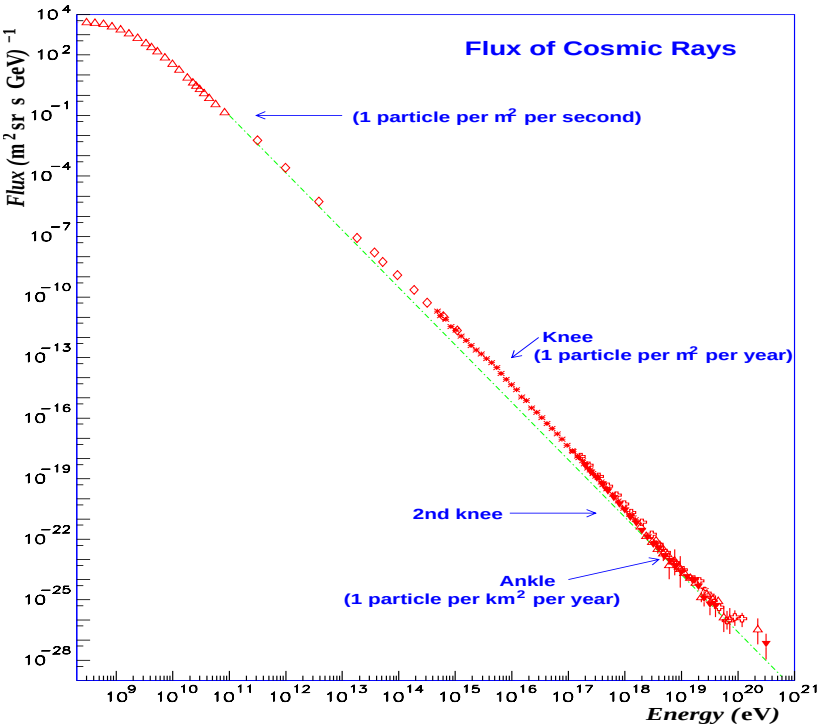

Figure 1.2: *CR total energy spectrum [1] .*

This flux is well described by a power law with a exponent around 2.7, except

for the region after the knee which is better fitted by a power of 3.2. Any physical mechanism pretending to explain the acceleration of the cosmic rays must meet this power law.

The precise origin of this cosmic rays flux is one of the questions to be enlightened, but it is believed there are different sources located inside our Galaxy, and for the end part of the energy spectrum, the origin may be extragalactic. There is also a low energy component coming from our sun, that AMS will not study.

As CR interact with the earth's atmosphere, all information about the primary particles is lost. To access to the primary spectrum it is necessary to send the spectrometer to space. That's what AMS pretends to perform in a more efficient way than previous experiments, essentially balloon borne. The Physics goals of this experiment can be summarized as:

- Searching for the existence or nonexistence of antimatter in the universe
- To contribute for the search of the dark matter.
- Not a less important question than the two previous items, yet maybe less spectacular, is to refine the knowledge of the cosmic rays spectrum composition.

The first item follows a continuous effort of several balloon experiments done expressly to study antimatter nuclei among the CR, like HEAT, BESS, CAPRICE and others (visit for instance the URL [4]).

In fact, the Big Bang model suggests that at the very beginning matter and antimatter should coexist. The evolution to a asymmetrical universe where only matter is observed is rather a problem asking for explanation. It has originated the baryogenesis theories, started with Sakharov in 1967 [5]. Different scenarios are described for the universe evolution, going from a universe with no antimatter at all, due to some matter-antimatter non equilibrium before the annihilation, to a universe globally symmetrical, with domains of matter and antimatter separated by great distances. There is still a great lack of experimental evidences to choose which one is the possible answer.

Different methods to search for this eventual antimatter can be adopted. An indirect evidence for the existence of antimatter domains contacting with matter

domains would be provided by the gamma radiation emitted by the mutual annihilation. This radiation would have a precise energy, and the non observation of such a radiation has excluded the hypothesis of such domains in a scale smaller than about 20 Mpc – the size of our local galaxies cluster [6].

By searching for the presence of antimatter nuclei among the cosmic rays that could have been emitted by antimatter domains, the AMS approach can be classified as a direct search for antimatter, just like the previously referred balloon experiments.

Indeed, the composition of cosmic rays includes some antiparticles like the antiprotons, but these are interpreted as being produced by the interactions of the CR with the interstellar medium. During its preparing phase, AMS has already performed a 10 days test flight aboard the space shuttle "Discovery" with a less equipped spectrometer and has detected 128 antiprotons. However, for heavier nuclei the production processes become so unlikely to occur that the detection of heavy antimatter ($|Z| \geqslant 2$) among the cosmic rays would constitute an irrefutable proof of the existence of antimatter somewhere in the universe.

The dark matter problem arises from gravitational evidences for the existence of much more mass in the galaxies than the visible or luminous part made of stars, which by our previous knowledge should be the dominant mass composition of the universe. A possible answer for this missing and dark matter problem may be found in Particle Physics. Some extension theories of the Standard Model foresee the existence of exotic and weakly interacting particles (WIMPS). From all these, it is believed that one of the most promising candidates is the supersymmetric Neutralino which is electrically neutral and expected to be rather massive. This particle can by its decay leave a kind of signature in some of the CR components (see [7]). At the present date, the deuterium spectrum is starting to be considered as a good candidate to perform this search ([8]).

The third main topic of the AMS goals will provide essential information to a better understanding of the cosmic rays physics, starting from their origin up to their propagation along the Galaxy. In particular, the measurement of certain isotopic abundances ratios at energies and with a much larger statistics than before, can provide an evaluation of the parameters present in the transport equation of

the cosmic rays like for instance their confinement time in the galaxy. Such measurements will be helpful to decide between different propagation models, like the Leaky Box or the Halo diffusion models, which one is more correct.

Additional measurements like for instance the evaluation of the interstellar medium density crossed by the cosmic rays can also be accessed. Such results are interesting for the Astrophysics, since they can be compared to other measurements methods (see [9]). An improvement on the measurements of the relative abundances of elements and isotopes composing the cosmic rays spectrum is then a important goal.

Essential to all the goals of this experiment is the large statistics amount of data to be collected. This has to do with the rarity or the observational difficulty of the phenomena to be studied in the antimatter and dark matter cases. On the isotopic studies, the improvement of the precision on the pretended measures requires a large decrease of the statistical error that dominates the current measurements.

In terms of data collecting, the acquisition time period of AMS will represent a huge increase on the available statistics gathered so far. In fact, it will increase by a factor of 10^4 to 10^5 the amount of data collected during 40 years of balloon experiments (see ref [2, 3]). The importance of this statistics is considered to be critical to establish the existence or nonexistence of antimatter in the scenario of a large scale matter-antimatter symmetric universe (see [10]).

Finally, an experiment with such a scope and scale has necessarily a good discovery potential, and it would be surprising that nothing new comes up at the end of this experiment. In fact, as previously referred the AMS experiment had already a testing phase in 1998, known as AMS01 during the STS91 NASA mission, which has approximately reproduced the ISS orbit. And yet, with such a short time data acquisition compared to the final phase in the ISS -AMS02, this first experiment has already brought us unexpected results respecting to fluxes of low-energy protons, electrons and positrons trapped in the earth magnetic field (see [11]).

1.2 The instrumentation of AMS

First of all, it is not too much to emphasize that the task of building an instrument like the AMS spectrometer to be sent to space represents a real technical challenge for experimental Physics and engineering. NASA has the responsibility to establish

the standards for some aspects of the construction and tests.

The proposal of the AMS experiment to the U.S. DOE [2] has greatly depended on the development of new materials for the building of permanent magnets as one can verify by the fundamental attention dedicated to this central piece of the detector (see [3] for a concise view of the proposal). This is not surprising, because this piece is the main contribution for the weight budget of the spectrometer. In the meanwhile, the permanent magnet has gave place to a superconducting magnet which will be able to deliver a larger magnetic field and thus allow to reach greater energies/momentums in the CR measurements.

The AMS experimental apparatus (see figs. 1.3 and 1.4) is basically a high energy detector, although in a smaller scale size due to the obvious weight limitations of a spatial experiment. Even so, this is a large detector from the point of view of the previous cosmic rays experiments. In order to acquire a large statistics, besides the need of operating the experiment for a long period of time — at least 3 years, the detector must have a large acceptance. With an overall acceptance of about $0.5\,m^2 \cdot sr$, AMS will be the largest operated cosmic rays spectrometer [1].

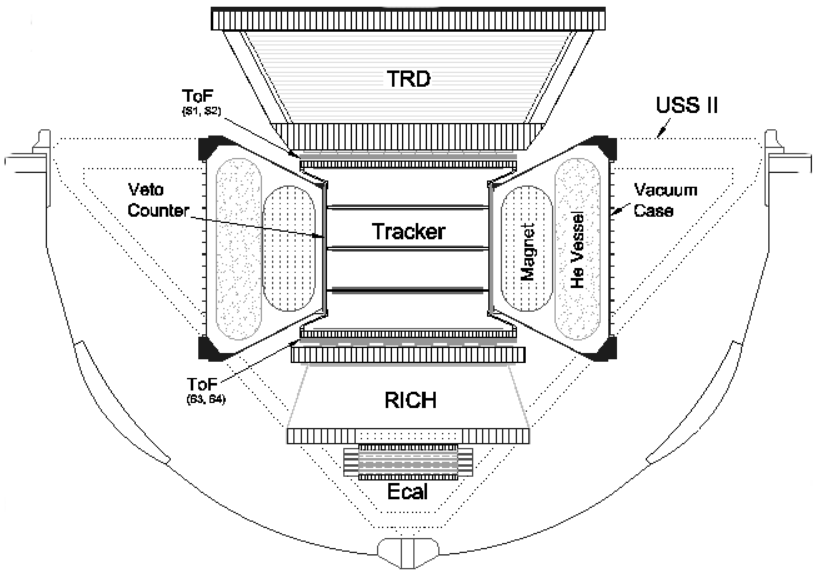

Figure 1.3: *Schematic draw of the AMS02 spectrometer mounted on the support structure (USS). The vertical size from the top of the TRD to the bottom of the ECAL is about 3m.*

[1] Compare it with the tiny acceptance of the cosmic rays telescopes equipping spacecrafts like for instance the Voyager missions, which is around $10^{-4}\,m^2 \cdot sr$!

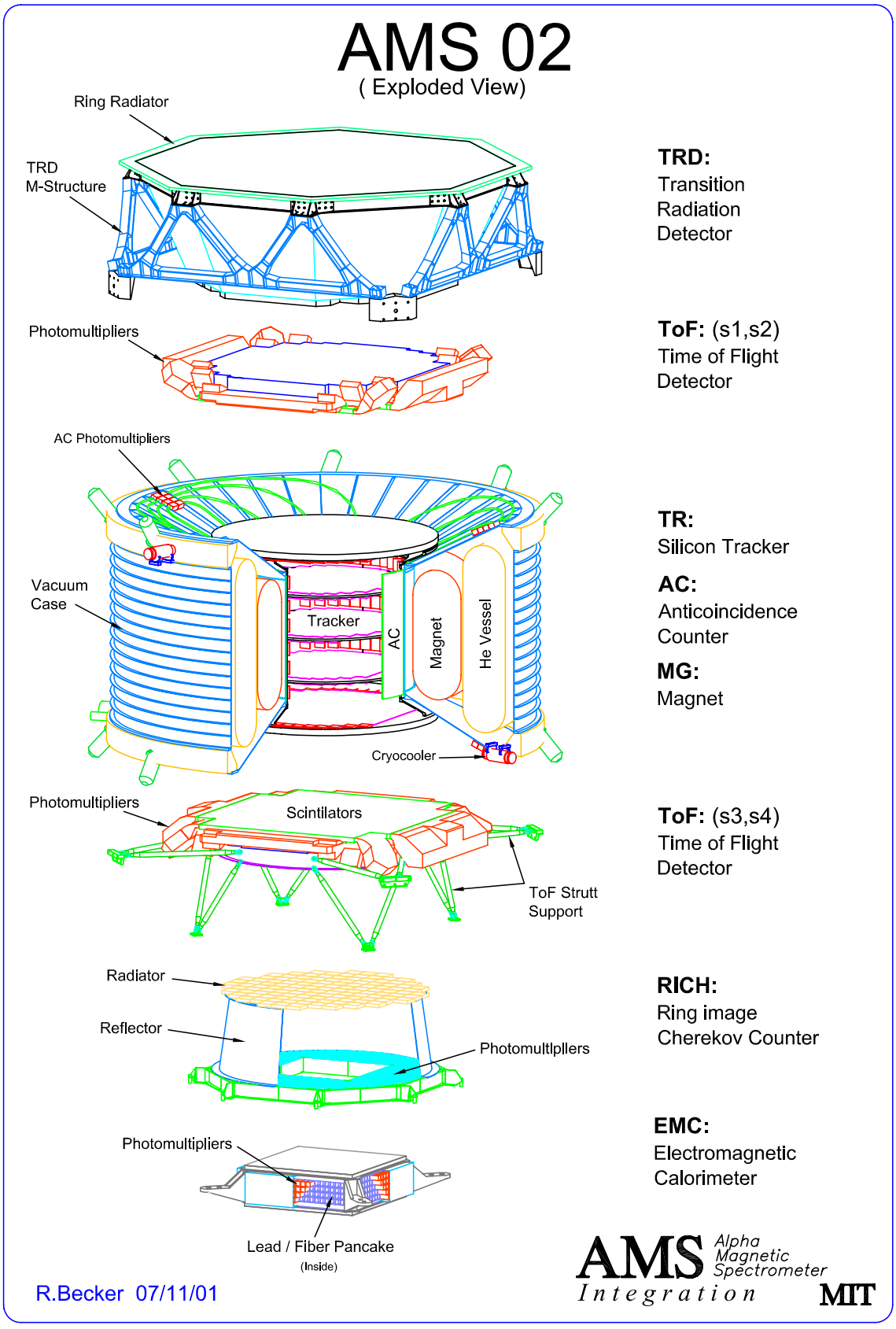

Figure 1.4: *Exploded view of the AMS02 spectrometer, where the subdetectors are well visible.*

The AMS spectrometer will be able to measure the velocity, charge — magnitude and sign, and also the momentum of the cosmic rays. Of particular interest is the particle identification, for which a charge and mass measurements must be performed for each particle crossing the spectrometer. We next describe summarily the collection of subdetectors that performs these measurements. In some cases, these subdetectors perform redundant measurements which is something desirable in a experiment where no maintenance can be done.

superconducting magnet

The superconducting magnet is the core piece of the spectrometer, providing the bending of the charged particles trajectories inside it. It provides an approximately dipolar magnetic field of about 0.9 T, transverse to vertical axis of the spectrometer. The analyzing power BL^2 of the AMS superconducting magnet [2] is about $0.8\,T\,m^2$. With this spectrometer – composed by the magnetic field plus a tracking system next described, it will be possible to measure the momentum of protons up to 1-2 TeV. The dipolar field is essentially given by two Helmhotz coils. There are 12 more smaller coils circumferentially disposed in order to reduce the stray field that could otherwise cause a torque on the ISS resulting from its interaction with the earth geomagnetic field. The superconducting coils are kept at a temperature near $1.8\,K$ by thermal contact with a surrounding vessel of liquid Helium.

Silicon Tracker

What a magnetic spectrometer is able of measuring directly is the particle rigidity:

$$R = \frac{pc}{Ze}\,,$$

where p is the momentum, Ze is the particle magnitude charge and c the light velocity in vacuum. The charged particles trajectories entering the approximately uniform magnetic field of the spectrometer, are deflected into an approximately circular trajectory along the transverse plane. The radius of this circle (r) is related to Rigidity by $r = \frac{R_T}{B}$, where R_T is the rigidity of the normal momentum component

[2] This is the design parameter related to the resolution on the measurement of the particle momentum: $\frac{\delta P}{P} \propto \frac{1}{BL^2}$

to the magnetic field B. For the estimation of this radius, the tracking of the particle is thus needed.

In AMS, the tracking is accomplished by eight silicon strips planes located inside the core of the whole spectrometer. This detector inherits the technology developed for the micro-vertex detectors of the ALEPH and L3 experiments operated at the LEP collider at CERN. This detector gives a spatial resolution of about $10\mu m$ (average between bending and non bending directions coordinates). This subdetector also does a charge measurement by $\frac{dE}{dx}$ measures. This way the particle momentum and charge are unfolded from the rigidity measurement.

Anticoincidence or Veto counter System

This system is composed by scintillators forming a barrel around the tracker. Its purpose is to reject events where secondary particles (δ rays or even showers) are produced inside the tracker and also to prevent events crossing AMS from the sideways.

Time of Flight detector – TOF

This unit gives the fast trigger of the experiment, establishing for instance the AMS lower threshold, such as to reject the low energy particles coming in the solar wind of a few MeV. It also gives a measurement of the time of flight of the particle across the detector, thus allowing a first velocity measurement. Redundant deposition energy measurements are also possible, allowing thus for a second charge determination.

The TOF detector is composed by four scintillator planes, two above the silicon tracker and two bellow it. Its time resolution is of the order of 130-140 ps, leading to a velocity resolution of about 3%.

While the previous described detectors are in some way a kind of upgrade relatively to the first phase AMS01, the remaining three units are entirely new detectors.

Transition Radiation detector – TRD

This subdetector works on the principle that a particle crossing between two different dielectric mediums emits radiation on the X rays domain. The intensity of

this radiation is proportional to the Lorentz factor $\gamma = 1/\sqrt{1-\beta^2}$. It is then well adapted to perform e/p separation,i.e. to separate positrons from protons and electrons from antiprotons, in the ultra relativistic region, where both the TOF and RICH detectors are no longer giving the best resolutions.

Ring Imaging Cherenkov detector – RICH

This detector is a proximity focusing kind of Ring Imaging Cherenkov counter. It will have the role of measuring the velocity with an accuracy of 10^{-3} for singly charged particles. This detector is also capable of a charge measurement.

Its functioning principle makes it capable of distinguishing upwards from downwards particles, complementing the capacity of the TOF. This is essential to reject albedo particles that otherwise can mimic antiparticles coming from the outer space. Having a central role on the work of this thesis, the RICH detector will be focused with some more detail in the next chapter.

Electromagnetic Calorimeter – ECAL

The AMS ECAL located under the RICH detector is a very compact 3-D imaging calorimeter. Is has a thickness of about 16.5 radiation lengths. It is mostly intended to perform e/p separation up to energies of about 1 TeV, by measuring the energy with a resolution of about 2% for 30 GeV. With the ECAL, AMS will also be able to perform some high energy photons physics.

Chapter 2

The RICH detector of AMS

2.1 The Cherenkov Radiation

The physical principle of a RICH detector relies on the Cherenkov radiation, that we next summarily describe.

The observation of a blue glowing radiation in radioactive solutions was reported several times since the beginning of the 20^{th} century by different people, like Marie Curie but also others. At the time it was thought this was some fluorescence phenomena.

It was only in the thirties that this radiation has been exhaustively studied by the Russian experimentalist Pavel *Čerenkov*, who has fully characterized this radiation.

The radiation production mechanism was theoretically explained in a purely classical electrodynamics framework by his colleagues Il'ja M. Frank and Igor'E. Tamm in a paper of 1937 [12]. For this co-work, the Nobel prize has been delivered to the three in 1958 [1]. It is interesting to note that this Nobel award comes after Chamberlain and its team discovery of the antiproton, made possible by the use of a differential Cherenkov detector, which has also worth them a Nobel prize in 1954.

In vacuum, the only way for a electric charge to emit radiation is to be accelerated, but in a dielectric medium, this changes drastically. A charged particle can emit electromagnetic radiation at uniform velocity if its velocity v exceeds the light velocity in that medium, i.e. if $v > \frac{c}{n}$, where n is the refractive index related to the

[1] In Tamm's Nobel lecture - available at the Nobel foundation web-site (`http://www.nobel.se`)- you can find an interesting historical perspective of the development of their work.

dielectric constant of the medium [2] by $n = \sqrt{\epsilon}$. The picture for this emitted radiation is quite similar to the one given to illustrate the sound shock waves produced by supersonic planes. The radiation emission occurs in a spatial coherent direction that is called the Cherenkov angle (see fig. 2.1). This angle (θ_c) is related to the particle velocity by the following relation:

$$\cos\theta_c = \frac{1}{n\beta}, \tag{2.1}$$

where the particle velocity is expressed in c units; $\beta = \frac{v}{c}$. This is the relation exploited in the RICH detectors, where a measure of θ_c is made, leading this way to the particle velocity β. It must be added that the energy lost by the particle in this radiation emission process is completely negligible and so it doesn't affect its velocity.

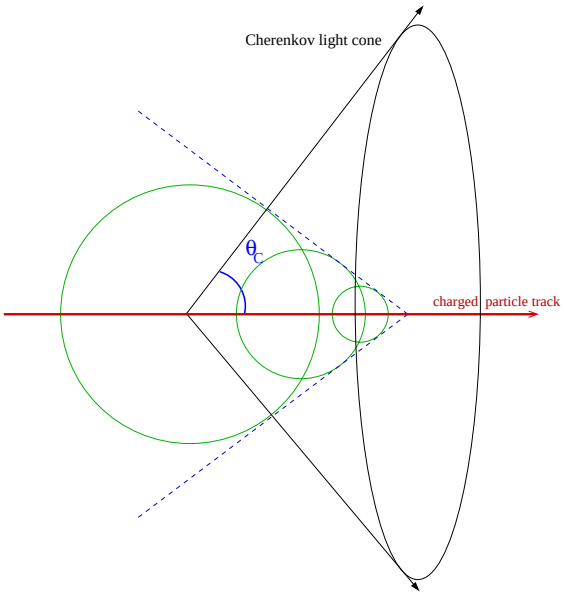

Figure 2.1: *The constructive interference of successive emitted spherical waves gives rise to a shock wave propagating in a direction related to the velocity of the source. The azimuthal symmetry leads to the formation a light cone with θ_c semi-aperture.*

Also of great importance is the intensity of the emitted radiation, here given in number of photons (N) by

$$\frac{dN}{dE} \propto Z^2\ L\left(1 - \frac{1}{\beta^2 n^2}\right), \tag{2.2}$$

where E is the spectrum energy of the emitted photons, Z is the electric charge magnitude of the considered particle, L is the length crossed by the charged particle

[2] Sometimes this is also called the relative electric permittivity

inside the dielectric material, usually called the radiator, and the remaining terms have already been introduced. Expressing eq. (2.2) in units of wavelength, one gets the following dependence:

$$\frac{dN}{d\lambda} \propto Z^2 \, L \left(1 - \frac{1}{\beta^2 n^2}\right) \frac{1}{\lambda^2}. \tag{2.3}$$

In figure 2.2, we show the dependence of the Cherenkov radiation angle with the velocity of the particle, also translated in a scale of momentum per nucleon, sometimes a more convenient units scale (right plot). The 3 curves correspond to 3 different material refractive indexes of possible interest for the AMS RICH setup. Refractive index 1.334 corresponds to a NaF radiator (Sodium Fluoride crystal), while 1.03 and 1.05 correspond to different Silica Aerogel radiators. These materials will be discussed in some more detail in next section.

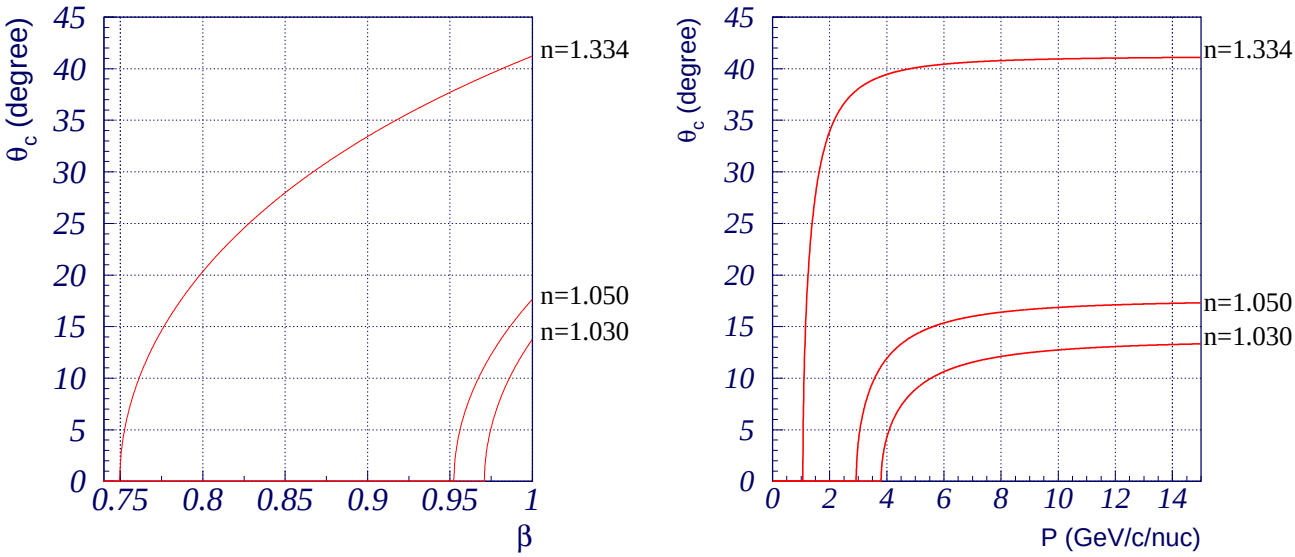

Figure 2.2: *The dependence of the Cherenkov angle with the velocity. With a very fair approximation (due to the slight difference between the masses of the proton and the neutron), one can also use the momentum per nucleon as an scale independent of the particle specie.*

Note the very different operating ranges allowed by these different materials. While a NaF radiator allows for velocity measurements above $\beta \sim 0.75$, for an Aerogel radiator of 1.05 refractive index it begins only for $\beta \sim 0.95$, and for a radiator of 1.03 index, this threshold becomes a value about 0.97.

As the accuracy of the velocity measurement will be a central concern of this work, we can start by introducing it by the reading of this velocity-Cherenkov angle plot. It is obvious that the sensitivity of the Cherenkov reconstructed angle to the particle velocity is higher in the Aerogel case than on the NaF. This conclusion follows from the difference between the curves slopes. For a given Cherenkov angle width, the corresponding subtended velocity width is quite larger on the NaF than on the Aerogel. The formal statement is given by the following expression:

$$\begin{aligned} \frac{\delta\beta}{\beta} &= \tan\theta_c \ \delta\theta_c \\ &= \sqrt{(n\beta)^2 - 1} \ \delta\theta_c, \end{aligned} \tag{2.4}$$

following directly from eq. (2.1).

The factor $\tan\theta_c$ represents then a sensitivity factor that is compared in the plots of figure 2.3, by means of the ratio for two different refractive indexes — n=1.03 and n=1.334. So, starting from a similar accuracy on the Cherenkov reconstructed angle for these two radiators, as it turns out to be the case (see ending part of section 2.3), we expect the relative resolution on the velocity to be about a factor 4 times better in the 1.03 refractive index case.

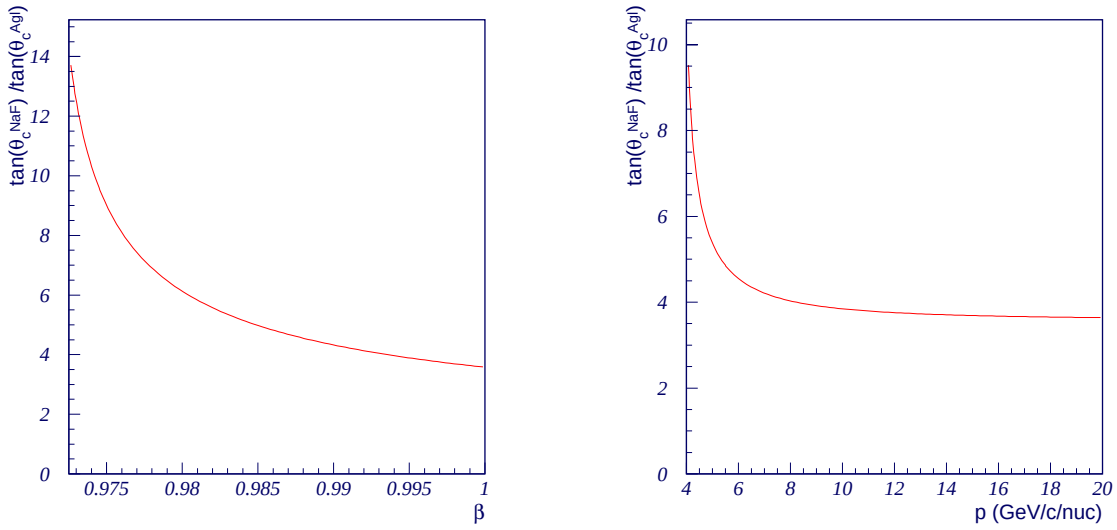

Figure 2.3: *Plot of the sensitivity factors ratio* $\dfrac{\tan\theta_c\,(n=1.334)}{\tan\theta_c\,(n=1.03)}$.

2.2 Detector Setup - general properties

Generally speaking, the AMS RICH detector can be split in 3 main composing parts, as depicted in figure 2.4, namely :

i) A Cherenkov radiator

ii) A vacuum expansion volume for the Cherenkov light cone surrounded by a conical reflector, in order to increase the collection of the Cherenkov light.

iii) A photodetection matrix at the bottom.

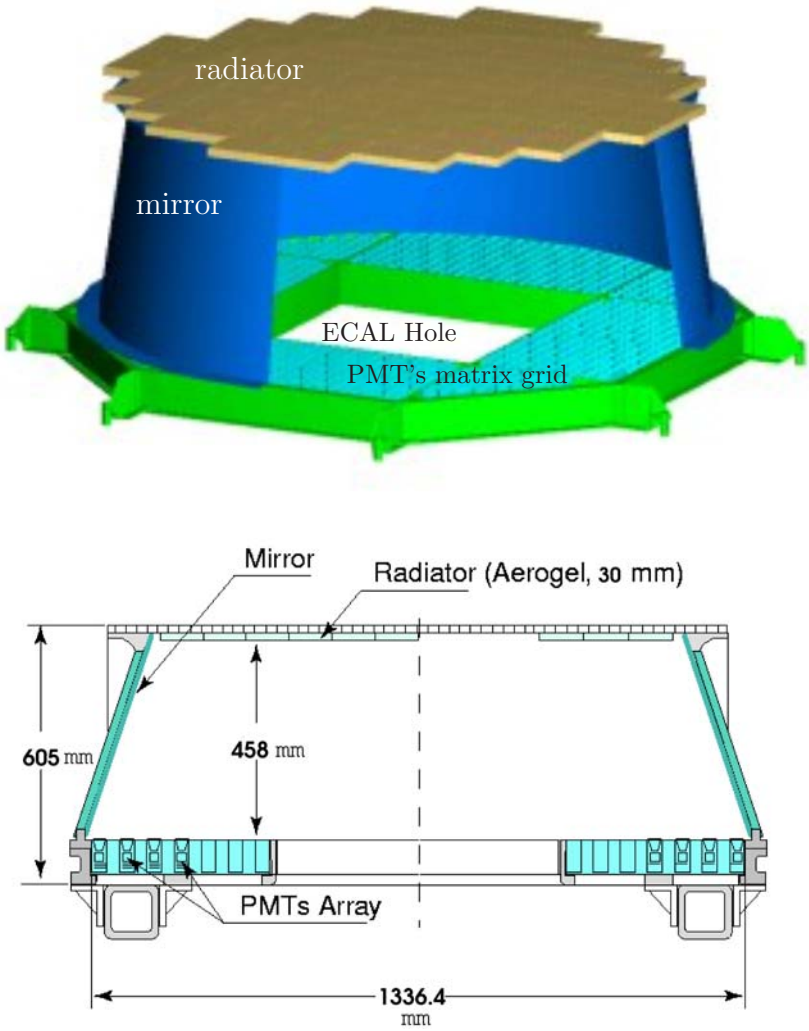

Figure 2.4: *Perspective and side-view of the RICH detector. For a more detailed top view of the PMT readout matrix, see fig. 5.1.*

the radiator

The choice of the material for the radiator has been strongly constrained by the fact that it must operate in the outer space. In these conditions, a solid material is preferred to any other gaseous or liquid kind of radiator by its higher robustness and simpler construction.

In the domain of solid radiators, the choice is not very large. Between the more classical materials, the lower refractive index is proportioned by the sodium fluoride crystal (NaF), with $n \simeq 1.334$. This allows to cover a very large dynamics range, since its velocity threshold is rather low — $\beta_{thr} \simeq 0.75$. On the other hand, being a rather high refractive index, it has the problem of internal total reflection of the photons in the radiator-vacuum transition. The critical angle is about 48.5 degree, which is very close of the Cherenkov angle for $\beta \simeq 1$ particles (~ 41.5 degree). As the cosmic rays have in general a non vertical incidence on the radiator, this means that there is always some part of the photons that is lost by this internal reflection. This feature decreases strongly the rather high light yield of this material.

This material has nevertheless already been used with satisfactory results in a cosmic rays balloon experiment (CAPRICE) including a RICH detector (see [13]). Another possibility is offered by silica Aerogel. This material is a kind of solid foam of silica (SiO_2) and trapped air. This makes it a very low density material. The refractive index of this material relates to its density by the following relation:

$$n = 1 + k\,\rho\,,$$

with k being an adimensional constant of the order of 0.2 and ρ the density of the Aerogel [14]. This material can be produced in a wide range of refractive indexes [15], from about 1.004 to 1.1. The Aerogel manufacturers provide it in blocks (or tiles) of around 15 per 15 cm, and with thicknesses up to 3 cm.

Aerogels of different manufactures and manufacturers have been tested for the final detector — some of them are studied in chapter 5. The choice is still not completely fixed but it points to a 1.03 refractive index [3], reason why we focused on this value along this work.

Comparatively to the NaF radiator, this material presents the following advantages, like a lower weight, which is an important issue when the weight budget is

[3] at least at the starting time of this work.

so constrained like in AMS. It also gives the possibility to take the isotopic mass separation farther up than with a NaF radiator – see ref. [16], due to a better velocity resolution like discussed in last section. Due to its low refractive index, it doesn't suffer from the total internal refraction at the radiator exit for any particle incidence direction.

The case of a NaF radiator will nonetheless also be recursively considered. The AMS collaboration has lately decided to consider a final design including both radiators, allowing the experiment to take advantage from the two different characteristics of such radiators, namely by allowing the experiment to complement the dynamic operating ranges of each radiator. The design consists in a central square of NaF surrounded by Aerogel. This design has the additional advantage to partially overcome the central ECAL dead area, which is a real problem for the most inner particle impact points in the Aerogel case (see ref. [16]).

The Aerogel structure, containing microscopic air pockets, is responsible for the Rayleigh scattering of the light crossing it, that confers to this material a typical bluish color tone.

The loss of directionality for some fraction of the Cherenkov photons constitutes a drawback of this material, as it creates a given amount of background signal that must be deal as we will see in chapter 3, section 3.1.2.

For this material, the radiation light yield is about 50 photons/cm for charges $Z = 1$ and $\beta \sim 1$. Due to the light guides and the PMT efficiencies and in some extent to the loss of photons into the non active area above the ECAL, that light yield is decreased to a mean value of around 5 detected photons.

the photodetection matrix

The detection of the Cherenkov photons is done by a matrix of 680 photomultiplier tubes (PMT's). The chosen PMT was the model R7600-M16 from Hamamatsu Inc. This is a 16 channels model, each pixel being a square with $4.5 \times 4.5\, mm^2$ dimension; see fig. 2.5.

It has a borosilicate glass window and a bialkali photocatode. Its spectral response ranges between 250 and 600 nm, reaching a maximum efficiency of about 20% and giving an average efficiency of about 14%; see figure 2.6.

To overcome the dead area of the PMT, a light guide unit has been developed.

Figure 2.5: *The R7600-M16 Hamamatsu PMT.*

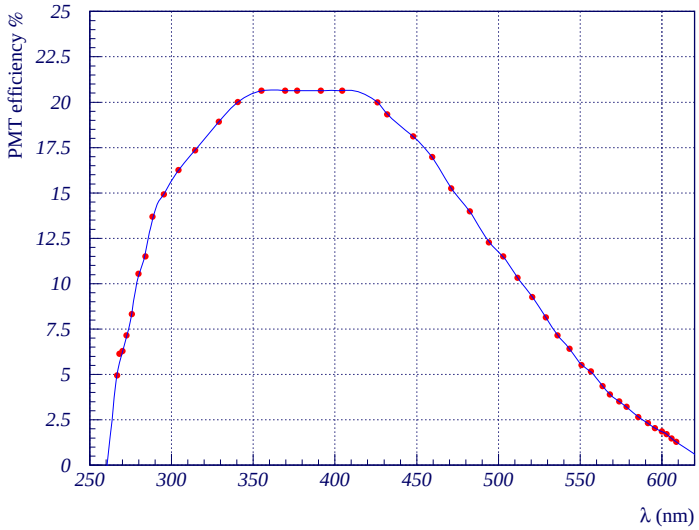

Figure 2.6: *R7600-M16 PMT quantum efficiency spectrum [17]. The curve line is a polynomial interpolation between the 44 reference points.*

The light guide unit is a pyramidal polyhedron composed of 16 solid Plexiglass pieces, one per each of the PMT pixels (see fig. 2.8), with a top pixel size of $8.5mm \times 8.5mm^2$. The assembling of the PMT with the light guide is illustrated in figure 2.7.

In fact, some dead space will still exist between adjacent light guides due to the need of shielding the PMT's from the magnetic field of the above superconducting magnet. So a gap of $3\,mm$ is left between successive light guides.

But the major dead area on the PMT's matrix arises from the presence of the electromagnetic calorimeter (ECAL) placed bellow. Because of this, the design of the matrix includes a central non active area — an approximate square of about $63 \times 63cm^2$ empty of any PMT's.

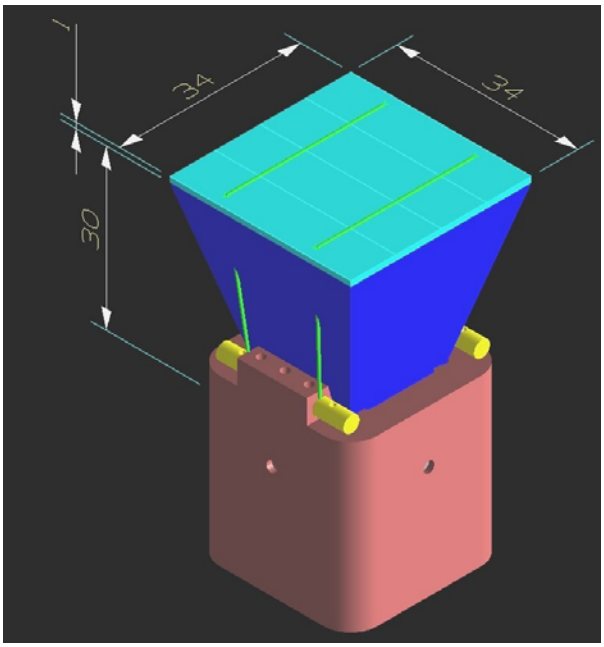

Figure 2.7: *PMT housing plus light guide.*

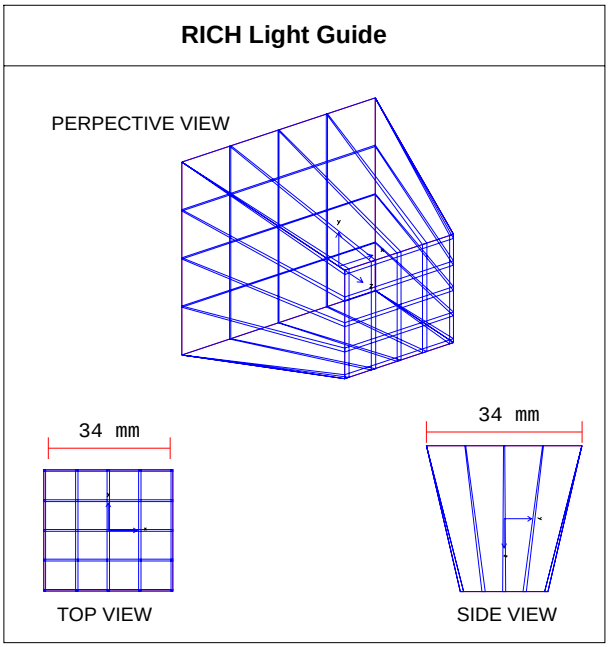

Figure 2.8: *Schematic draw of the RICH light guides.The 16 pieces are held together by a thin layer on the top. This allows the 16 pieces to be separated by air, in order to conduct light by internal reflections.*

General properties of the RICH detector

Next, we describe some important features of the RICH detector.

A simulation of the RICH detector ([18]) has been used for the development and testing of the reconstruction algorithm presented in this thesis [4]. This simulation is based on the (FORTRAN) GEANT 3 libraries supported by CERN. The next figures and results are based on this simulation.

A cosmic particle is inside the AMS acceptance if it crosses the whole tracker. We equally speak of a RICH accepted event if the particle crosses the RICH radiator. By a look to the schematic setup of AMS, given in figure 1.3, we can foresee that some of these particles won't cross the RICH radiator. Figure 2.9 shows the angular acceptances of RICH and AMS in the polar angle of the particles. Only about 80% of the events accepted by the AMS spectrometer are also accepted by the RICH detector.

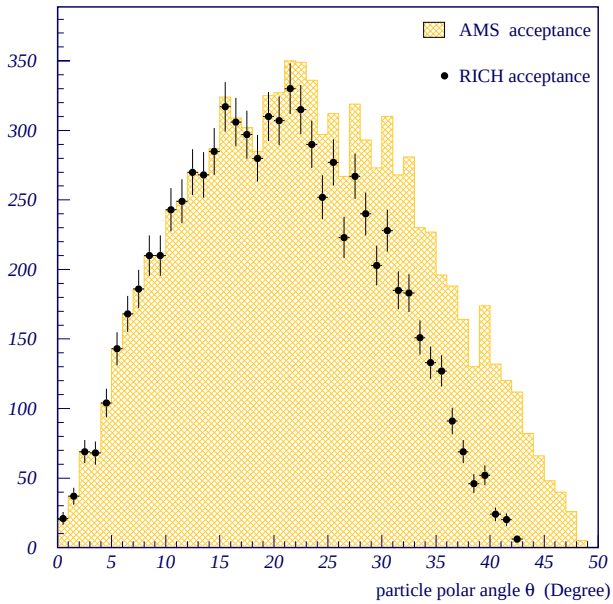

Figure 2.9: *RICH acceptance corresponds to nearly 80% of AMS acceptance. (The polar angle zero corresponds to the vertical direction)*

After the particle passes the RICH detector acceptance, it is equally important

[4] Thanks to a prototype already existent since the end of 2000, the algorithm has also been tested with real data. Chapter 5 presents this analysis.

that the Cherenkov radiated photons are not lost outside the detection area. This is the reason why the RICH setup includes a conical mirror around the expansion volume. Figure 2.10 plots the fraction of the photons that reaches the PMT readout matrix by suffering some reflection on this mirror in the case of particles with ultra-relativistic velocities ($\beta \sim 1$) with all the directions inside RICH acceptance.

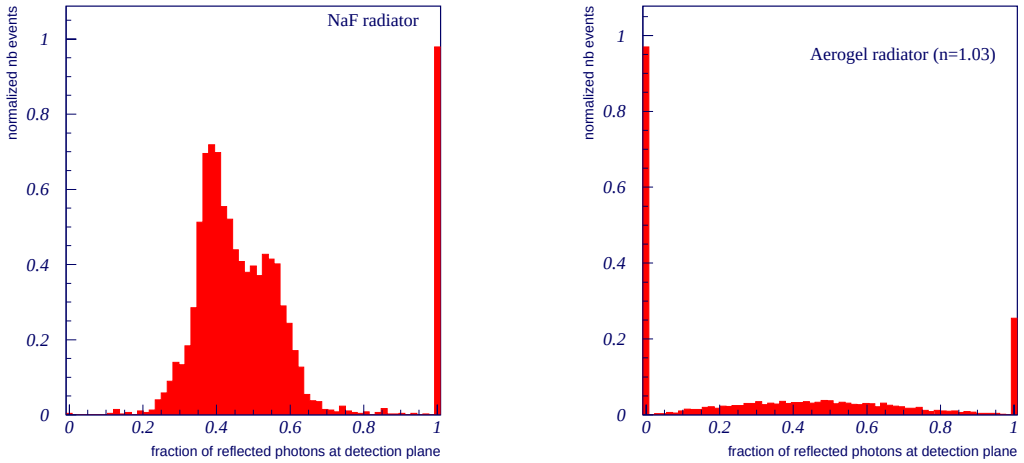

Figure 2.10: *Fraction of reflected and detected photons. Comparison for radiators NaF and Aerogel (n=1.03). These plots have been obtained for Cherenkov cones of maximal aperture ($\beta \simeq 1$) and a mirror reflectivity of 85%.*

The NaF radiator gives a very large Cherenkov cone – about 41 degree – and this is why there is always reflected photons, with a mean value of about 50% of the Cherenkov ring passing through the mirror. The peak of fully reflected Cherenkov cones accounts only for about 1% of the events.

With the same kinematic conditions, the Aerogel gives a much more larger spread distribution (right histogram). This is because for a Cherenkov cone with 14 degree of semi-aperture, there is a strong dependence on the particle track variables — direction and impact point on the radiator. This causes the fraction of detected and reflected photons to vary from zero in about 40% of the events, up to one in only 10% of the events. In any case, the *ring acceptance*, i.e. the fraction of the Cherenkov ring that is collected in the active area, is compulsorily increased.

On the Aerogel radiator case, another important question is about the fractional quantity of photons reaching the PMT matrix without being dispersed by the Rayleigh scattering of the radiator. The Rayleigh scattering makes photons to

lose their original direction. Being interested only on the photons along the original direction, one can speak of a transmittance (t) as a measure of the fraction of the non scattered photons at the exit of the radiator. This transmittance is a function of the photon's crossed length inside the radiator, according to the following relation

$$t(x, \lambda) = \exp(-Cx/\lambda^4), \tag{2.5}$$

where x is the radiator crossed length and λ is the photon wavelength (see ref. [15] for instance) [5]. The constant coefficient C is then a measure of the radiator transmittance and it is usually called the clarity coefficient of the radiator. This designation is somehow unfortunate and we should rather reserve it for the inverse quantity $\frac{1}{C}$. Nevertheless, with this convention the greater this clarity coefficient is, the lower we have for the transmittance.

The ratio $\frac{\lambda^4}{C}$ can be understood as an interaction length. Figure 2.11 shows that for a clarity coefficient of $0.0042\mu m^4 cm^{-1}$, which is an optimistic value, the fraction of detected photons that have been scattered has its most probable value around 12%, while for a more standard value of $0.009\mu m^4 cm^{-1}$, this fraction rises to about 22% . Figure 2.12 gives a fair illustration of the effect of the Rayleigh scattering for different clarities.

Next section treats the issue of the achievable resolution with the RICH detector of AMS.

2.3 Cherenkov angle uncertainty in the RICH detector

From the Cherenkov relation 2.1, one derives the relative velocity resolution. This can be expressed by the following relation

$$\frac{\delta\beta}{\beta} = \tan\theta_c \delta\theta_c \ ,$$

where the uncertainty on the Cherenkov angle ($\delta\theta_c$) accounts for the next listed sources .

[5] When one also includes the absorption effects, only relevant at great wavelengths an additional coefficient comes up giving $t(x, \lambda) = A\exp(-Cx/\lambda^4)$

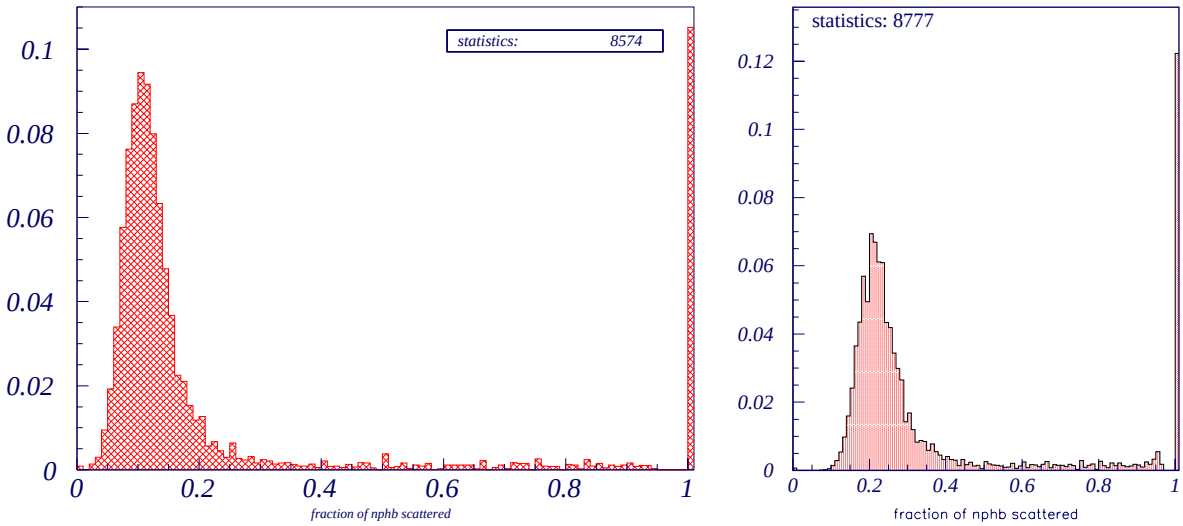

Figure 2.11: *Fraction of the photons reaching the detection matrix suffering Rayleigh scattering photons, for two different clarities (these are 0.0042 and 0.009 μm^4 cm^{-1} for the left and right figures respectively).*

(i) *Chromaticity*

For each single precise value of the charged particle velocity, the chromaticity of the radiator gives rise to a (narrow) Cherenkov angle spectrum, instead of a precise value for this variable.

(ii) *radiator thickness*

Being a proximity focusing RICH (as opposite to the optical focusing type used in the accelerator experiments), the radiator thickness introduces a spreading of the photons on the Cherenkov ring.

(iii) *PMT Pixel size*

The pixel dimensions of the PMT readout matrix also establishes a limit to the accuracy to which one can access to the hitting positions of the photons, used for the geometrical reconstruction of the Cherenkov angle.

Some authors explicit the chromaticity source by writing $\frac{\delta\beta}{\beta} = \tan\theta_c \delta\theta_c \oplus \frac{\delta n}{n}$. If the refraction is not taken into account, the two formulations are equivalent. Even so, as the only measured variable is θ_c, we think it is more natural to express the uncertainty of β as depending on the uncertainty of θ_c only, including all effects inside $\delta\theta_c$.

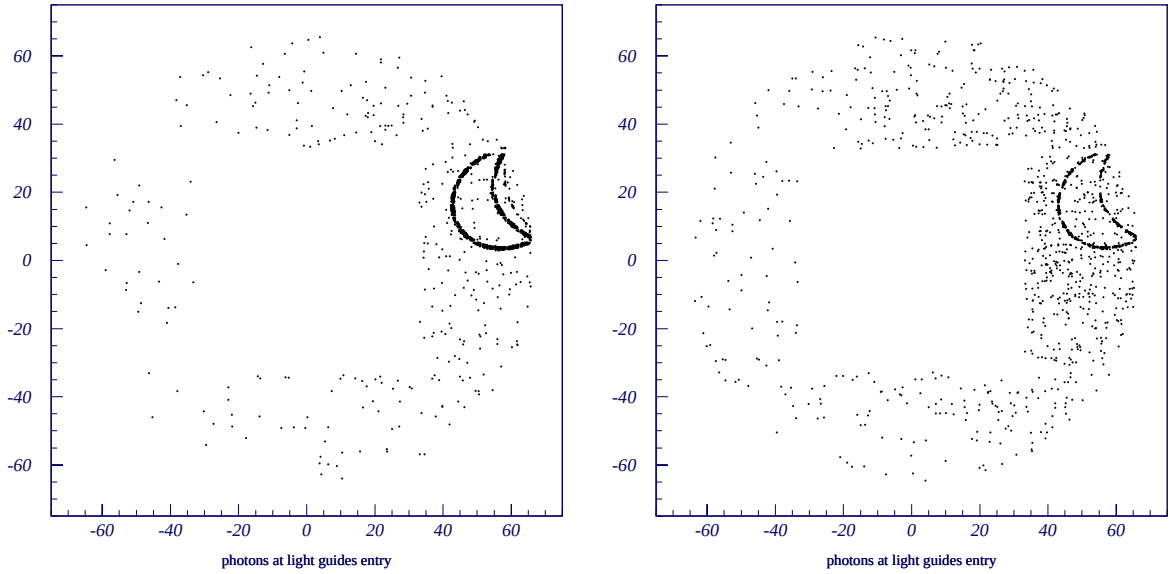

Figure 2.12: *Spatial illustration of the background noise on the PMT readout matrix, due to the Rayleigh scattering. One can clearly see the increase of the background noise as the radiator clarity changes from the left value ($0.004\,\mu m^4 cm^{-1}$) to the much worst value of the right plot ($0.05 \mu m^4 cm^{-1}$). Plots were obtained for 200 protons with velocity* $\beta = 0.999$.

Noting the independence of these sources,we can write down

$$\delta\theta_c = \delta\theta_c^{\text{chro}} \oplus \delta\theta_c^{\text{geo}} ,$$

where $\delta\theta_c^{\text{chro}}$ accounts for the intrinsic chromaticity (i) and $\delta\theta_c^{\text{geo}}$ accounts for the uncertainty sources of geometrical nature (ii) and (iii). In the following, we try to give a impression of the relative importance of these sources.

2.3.1 chromaticity

Any refractive medium is characterized by a chromatic dispersion relation, i.e., the refractive index depends on the wavelength of the radiation crossing the medium by some relation $n(\lambda)$. Starting by the NaF case, where this effect is of greater importance, compared to the Aerogel case, we show its chromatic dispersion in figure 2.13.

There is so a wavelength dependence for the Cherenkov angle of the emitted photons. Therefore, the wavelength spectrum of the detected photons determines the resulting Cherenkov angle spectrum due to this radiator chromaticity. This

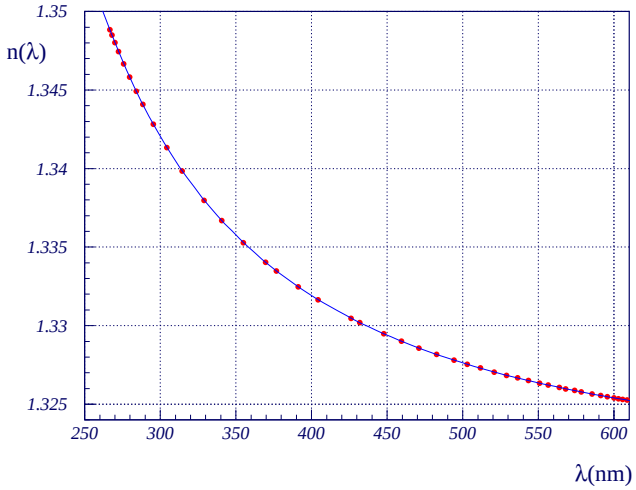

Figure 2.13: *Chromatic dispersion of the NaF radiator. A parametrization of this curve can be found in ref. [19].*

detected wavelength spectrum depends not only on the intrinsic Cherenkov radiation emission spectrum of eq. (2.3) but also on the PMT efficiency spectrum. There is still others minor effects such as the Rayleigh scattering wavelength dependence and the absorption wavelength spectrum of the plastic foil layer put bellow the radiator tiles that causes some modulation on this *detected wavelength spectrum*.

Considering only the convolution of the emission spectrum with the PMT efficiency spectrum of figure 2.6, we show what would be the wavelength spectrum of the detected photons in figure 2.14. For an easier appreciation of the change of form, these spectra are both normalized to unit.

So, the *chromaticity* has a direct implication on the Cherenkov angle resolution, since even for a fixed particle velocity, there is not a single value for the refractive index in the Cherenkov relation:

$$\theta_c(\lambda) = \arccos \frac{1}{\beta\ n(\lambda)}\ .$$

A little dedicated simulation has been done to explore this chromaticity effect. Basically, the simulation consists in generating photon's wavelengths according to the convolution of the production spectrum with the PMT efficiency spectrum, and by the use of an appropriated parametrization of the chromatic dispersion $n(\lambda)$, one just has to compute the Cherenkov angle according to the previous Cherenkov relation for a fixed value of β. An illustration of the resulting effect is given for instance in figure 2.15, where an asymmetric distribution of Cherenkov angles is obtained.

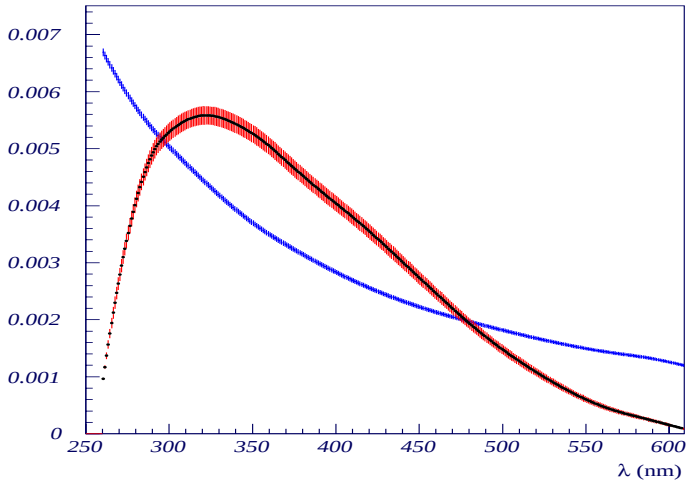

Figure 2.14: *Wavelength spectrum of the Cherenkov photons (at emission and detection). The production spectrum of Cherenkov photons is the monotonous decreasing curve ($\frac{dN}{d\lambda} \propto \frac{1}{\lambda^2}$). The convolution of this spectrum with the detection PMT efficiency spectrum gives rise to the second curve.* **Both spectra are normalized to unit.**

Note that the convolution with the PMT efficiency spectrum has here a nice effect which is to attenuate the chromaticity dispersion. Note also that despite the peak of $\Delta\theta_c$ being around -3.5 $mrad$, the mean value is very close to zero.

In conclusion, the width of this spectrum can be taken as the chromaticity term ${\delta\theta_c}^{\text{chro}}$ of page 24.

For Aerogel 1.03, the chromatic dispersion is graphically given in the plot of figure 2.16. Note that in this case the chromaticity amplitude is a factor of about 9 lower than in the NaF case, $\Delta n^{\text{AGL}} \sim 0.0027$ and $\Delta n^{\text{NaF}} \sim 0.024$. With this chromatic dispersion, and using the same velocity of $\beta \simeq 1$, the Cherenkov angle dispersion spectrum is the one of figure 2.17. Note that this distribution is narrower than in the NaF case.

Using the Cherenkov relation (eq. 2.1) for a fixed value of β, one derives the following relation dependence on the velocity for this chromaticity angle uncertainty.

$$\begin{aligned} \delta\theta_c^{\text{chro}} &= \frac{1}{\tan\theta_c}\,\frac{\delta n}{n} \\ &= \frac{1}{\sqrt{(n\beta)^2-1}}\,\frac{\delta n}{n} \end{aligned} \tag{2.6}$$

By using the referred dedicated simulation with different velocities one can illustrate in a very visual way this velocity dependence. In figure 2.18 one can clearly see

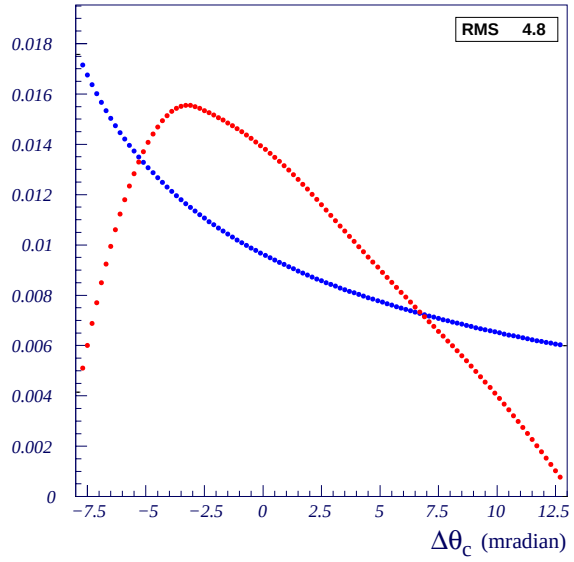

Figure 2.15: *The effect of the chromaticity on NaF. The monotonous spectrum results from chromatic dispersion only. The 2nd spectrum results from convoluting the PMT efficiency. The variable in histogram ($\Delta\theta_c$) represents the difference between the emission angle obtained for each wavelength (λ) and the nominal Cherenkov angle, i.e., the value of θ_c for the mean refractive index (1.334). The indicated R.M.S refers to the convoluted spectrum.* ***The two spectra are normalized to the unit****.*

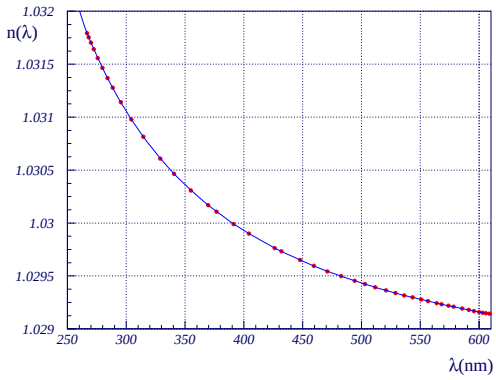

Figure 2.16: *The chromatic dispersion of the 1.03 Aerogel radiator. The reference values are obtained from a scaling done to the well known measured values of the fused Silica [19]. The line is a polynomial interpolation.*

the spread of the Cherenkov angle spectrum becoming narrower with the increase of the mean Cherenkov angle or equivalently speaking with the increase of the velocity. The evolution of the dispersion of these chromaticity spectra with the velocity is plotted in figure 2.19, with the fit of function referred in eq. (2.6) plotted on top.

Note that although the parameters δn from the fits in fig. 2.19 are smaller than the total amplitudes of the respective chromatic dispersions, the ratio between them

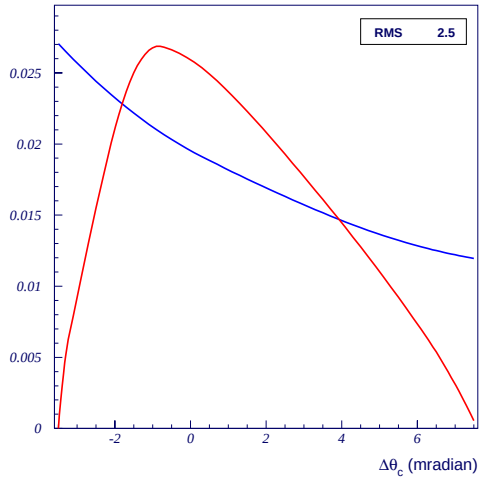

Figure 2.17: *The effect of the chromaticity on AgL (n=1.03). The monotonous spectrum results from chromatic dispersion only. The 2nd spectrum results from convoluting the PMT efficiency. $\Delta\theta_c = 0$ corresponds to n(λ)=1.03.The indicated R.M.S refers to the convoluted spectrum.* ***The two spectra are normalized to the unit.***

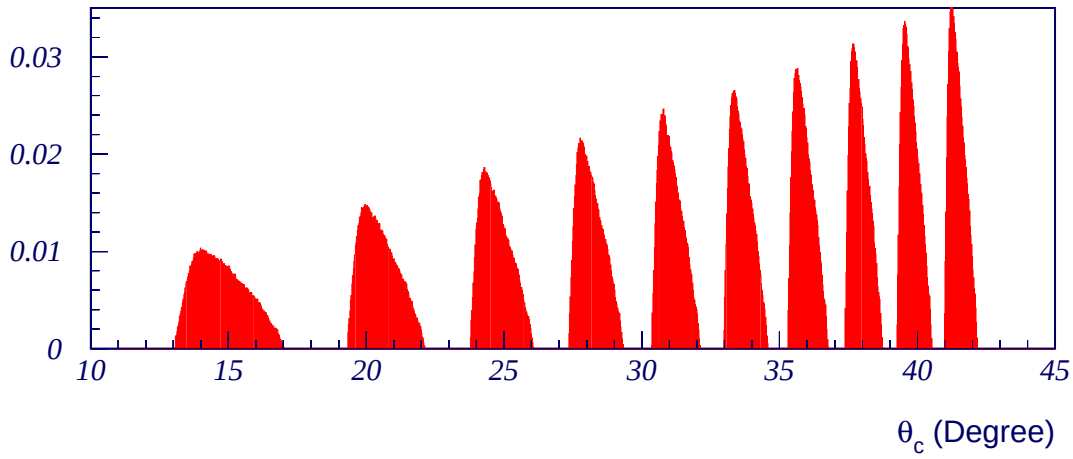

Figure 2.18: *Illustration of the dependence of the chromaticity uncertainty on the velocity (equivalent to the mean Cherenkov angle) for the NaF radiator.*

keeps being a factor of about 10.

Two final notes concerning this chromaticity issue need to be given before moving on to the geometrical uncertainty sources. In the first place, there is an extra modulation of the Cherenkov photons spectrum imposed by the supporting plastic foil underneath the radiator tiles that must be taken into account. This plastic foil basically absorbs almost completely the photons with wavelengths under $300\,nm$, resulting then in a narrower spectrum and consequently in a lower chromatic dispersion. This results in the decreasing of the previous δn values to 3.5×10^{-3} and

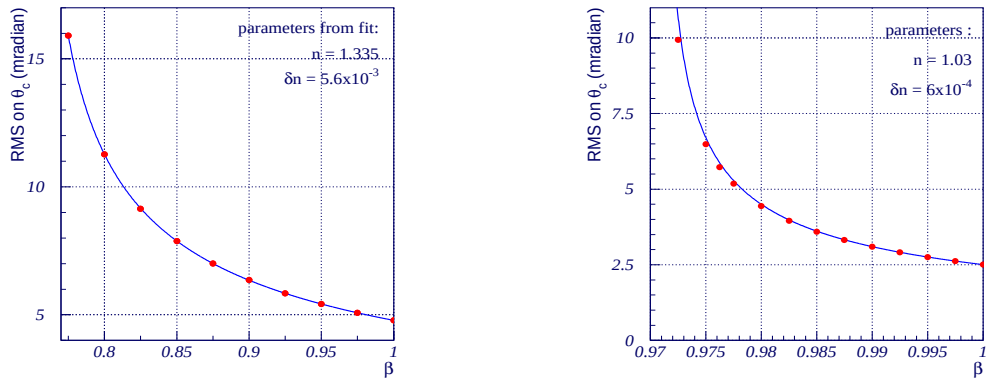

Figure 2.19: *RMS for the θ_c chromaticity spectra versus velocity.* Left: *NaF radiator.* Right: *Aerogel radiator. Dots correspond to the RMS of the chromaticity spectra. Line corresponds to the fitted function of eq. (2.6)*

4.1×10^{-4} for the NaF and Aerogel radiators respectively.

In the second place, we must observe that the reconstruction is going to give a larger dispersion of the Cherenkov photons angles than the intrinsic one just discussed. This is schematized in the following figure (fig. 2.20).

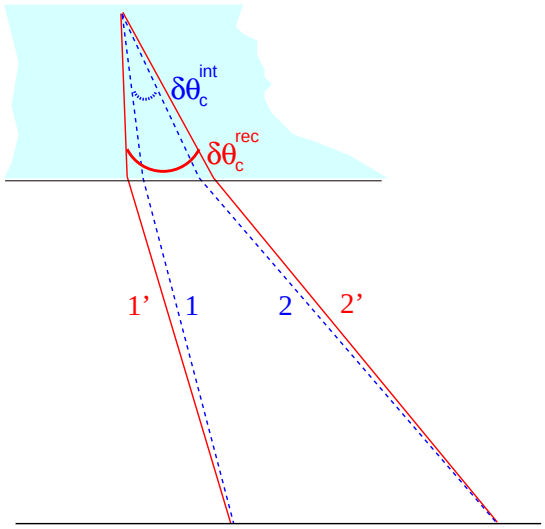

Figure 2.20: *Illustration of the reconstructed chromatic uncertainty ($\delta\theta_c^{rec}$) as a larger uncertainty than the intrinsic one ($\delta\theta_c^{int}$).*

The rays 1 and 2 represent the farther possibly apart Cherenkov photons due to the intrinsic chromatic dispersion $\delta\theta_c^{\text{int}}$. As the reconstruction procedure tries to trace-back let's say photon 2, it will not recover the precise photon track but rather the track depicted by 2', due to making use of the mean refractive index which is a lower value than the one 'felt' by photon 2. In an analogous way the lower Cherenkov angle of the photon 1 is reconstructed as an even lower angle - track 1'.

This leads to a chromatic dispersion $\delta\theta_c^{\text{rec}}$ that is larger then the intrinsic one ($\delta\theta_c^{\text{int}}$).

And so a small correction must be introduced to the chromaticity uncertainty source. By Snell's law, one has to correct the intrinsic uncertainty present on the photon direction θ_i before refraction by the factor

$$\frac{n\,\cos\theta_i}{\sqrt{1-(n\,\sin\theta_i)^2}}\,,$$

Taking the simple case of vertical incidence of the particle, where $\theta_i = \theta_c$, we introduce this multiplying correction factor in expression 2.6. This factor is very close to one for all velocities in the Aerogel case. But in the NaF case it rises up to a value of nearly 2 for $\beta \simeq 1$.

2.3.2 radiator thickness and pixel size

In a proximity focusing RICH detector, the word focusing is misleading, because there is not a real optical focusing of the photons. In fact, instead of a perfect ring, what we deal with is a series of concentric rings corresponding to Cherenkov cones with its apexes going from the top to the bottom of the radiator. This is illustrated in figure 2.21, for the most simple case of a vertical incidence of the particle .

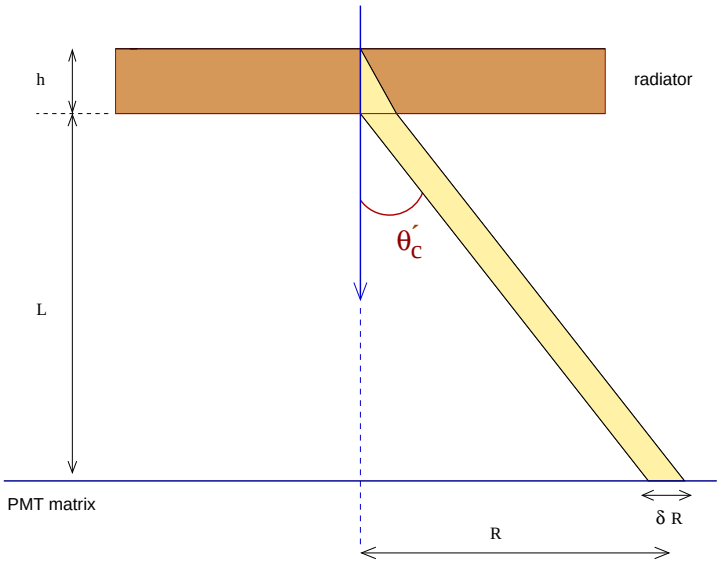

Figure 2.21: *Cherenkov ring width due to the radiator thickness in case of vertical incidence. θ_c' corresponds to the photon's angle after refraction. Note: the ring width doesn't depend on the refraction.*

The "focusing" in such a kind of RICH detector consists simply in managing that the expansion volume height L is much larger than the radiator thickness h, in

order to the ring *width* δR to be negligible compared to the ring radius R (see fig. 2.21), and so allowing to perform the geometrical reconstruction of the Cherenkov angle considering all the photons emitted at one same single point. In the AMS case, we have $L = 45.8cm$ and $h = 3cm$ for the Aerogel setup. In the NaF setup, $h = 0.5cm$.

So in principle, besides the chromatic error previously discussed, this radiator thickness is also a limiting source to the accuracy to which we can compute the Cherenkov emission angle.

In addition to this radiator thickness effect, there is also and mostly the granularity of the photons detector that creates a geometrical dispersion of the detected photons positions. Both these effects contribute to the uncertainty of the radius illustrated in fig. 2.21 (the *ring width* δR). In the next we evaluate the contribution of each one of these effects.

We base our discussion on the vertical particle incidence case of figure 2.21. In this case, we have the following *reconstruction* equation, relating for each photon its emission angle θ_c with a measurable radius R:

$$\frac{nL\tan\theta_c}{\sqrt{1+(1-n^2)\,\tan^2\theta_c}} + \frac{h}{2}\tan\theta_c = R \quad .$$

In this previous equation, n is the refractive index of the radiator and the refraction between the radiator-vacuum interface has been taken into account for its importance in the NaF case (see appendix A). The factor $\frac{h}{2}$ is due to the assumption of considering the photons emitted at the middle of the radiator.

We have then for each photon, a measure of R with a uncertainty δR due to the radiator thickness effect plus the pixel size (granularity of the photons detector unit). This uncertainty δR propagates to the Cherenkov angle, computed by solving eq. (2.7), according to the following expression:

$$\begin{aligned} \delta\theta_c^{\text{geo}} &= \cos^2\theta_c \quad \frac{\delta R}{n\,\mathcal{R}(\theta_c)\,L + h/2} \\ &= \cos^2\theta_c \quad \frac{\delta R^{\text{pixel size}} \;\oplus\; \delta R^{\text{rad.thick}}}{n\,\mathcal{R}(\theta_c)\,L + h/2} \quad . \end{aligned} \tag{2.7}$$

The coefficient $n\,\mathcal{R}(\theta_c)$ constitutes a correction factor due to the refraction (see appendix A). By considering the little triangle inside the radiator in fig. 2.21, it is

straightforward to write the ring width due to the radiator thickness as:

$$\delta R^{\text{rad.thick}}(\theta_c) = \frac{h \tan\theta_c}{\sqrt{12}} .$$

Note that as the ring width is originated inside the radiator, the refraction doesn't play any role in it, since it "curves" equally all the *photons rays*. The factor $\sqrt{12}$ is based on the assumption of a uniform emission along the radiator thickness. In the case of Aerogel, due to a not so high transparency this assumption is not entirely correct as we will see in section 3.2.2. The simulation can nevertheless be used in order to substitute the factor $\frac{h}{\sqrt{12}}$ by the R.M.S of the correct p.d.f. for the z coordinate of the photons coming out of the radiator. This is a minor effect, but if taken into consideration, the resulting values are then given by:

$$\frac{\delta R^{\text{rad.thick}}}{\tan\theta_c} = \begin{cases} 0.14\,cm \text{ for a NaF radiator of } 5\,mm \text{ thickness} \\ 0.75\,cm \text{ for a Aerogel radiator of } 3\,cm \text{ thickness} \end{cases}$$

The pixel contribution for the uncertainty δR arises from the independent uncertainties present on each coordinate of the detected point, $(\delta x\,, \delta y)$, as follows:

$$\delta R = \frac{x\delta x}{R} \oplus \frac{y\delta y}{R} .$$

As we have square pixels, $\delta x = \delta y$ and then we have:

$$\begin{aligned} \delta R^{\text{pixel size}} &= \delta x^{\text{pixel size}} = \delta y^{\text{pixel size}} \\ &= \frac{\text{pixel side}}{\sqrt{12}} = \frac{0.85\,cm}{\sqrt{12}} \approx 0.25\,cm\,. \end{aligned} \tag{2.8}$$

This result can be appreciated in the graphical form of the histograms on figure 2.22, that were obtained by doing a little dedicated simulation. The dispersion on each coordinate follows the left uniform distribution, being then transformed into the bell shaped distribution of the right plot when analyzing the dispersion in the two dimensions. The dispersion stays nevertheless the same as the result of eq. (2.8) states.

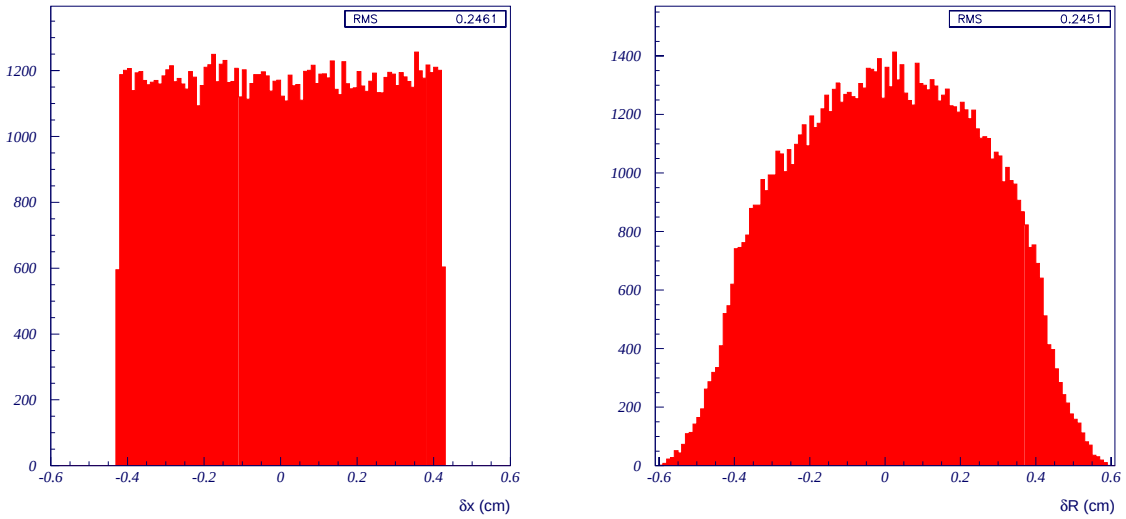

Figure 2.22: *Dispersion of the detected points for the Cherenkov photons at the detection level plane (1-D and 2-D). Note that despite the change of form on the distribution, the dispersion remains the same.*

It is interesting to give a physical interpretation to the factors of formula (2.7) in the limit of a null refraction,i.e., $n = 1$ and $\mathcal{R}(\theta_c) = 1$:

$$\delta\theta_c^{\text{geo}} = \cos^2\theta_c \quad \frac{\delta R}{L + h/2}\,.$$

The factor δR can be seen as representing the global granularity of the photons detector, i.e., pixel size plus radiator thickness effect. When multiplied by $\cos\theta_c$, it can be reinterpreted as an effective granularity, in the sense that $\delta R\,\cos\theta_c$ is the projection of the granular unit size '*seen*' by the photon.

The remaining factor $\dfrac{L + h/2}{\cos\theta_c}$ is simply the *photon's path* length and so eq. (2.7) is simply stating that the geometrical uncertainty for the Cherenkov reconstructed angle is directly proportional to this effective granularity and inversely proportional to the *photon's path* length. In the case of a NaF radiator, the refraction correction factor $n\,\mathcal{R}(\theta_c)$ applied in the denominator has the effect of decreasing the final geometrical uncertainty as it can be seen in the plot of fig. A.2 (appendix A).

Note at last there is a velocity dependence present in eq. (2.7) disguised by the θ_c dependence. For a better appreciation of each source term in expression 2.7 — pixel source and radiator thickness terms — we plot the resulting functions separately, together with their quadratic sum in figure 2.23.

Note that what is called the pixel contribution in the plot is the term $\cos^2\theta_c\times$

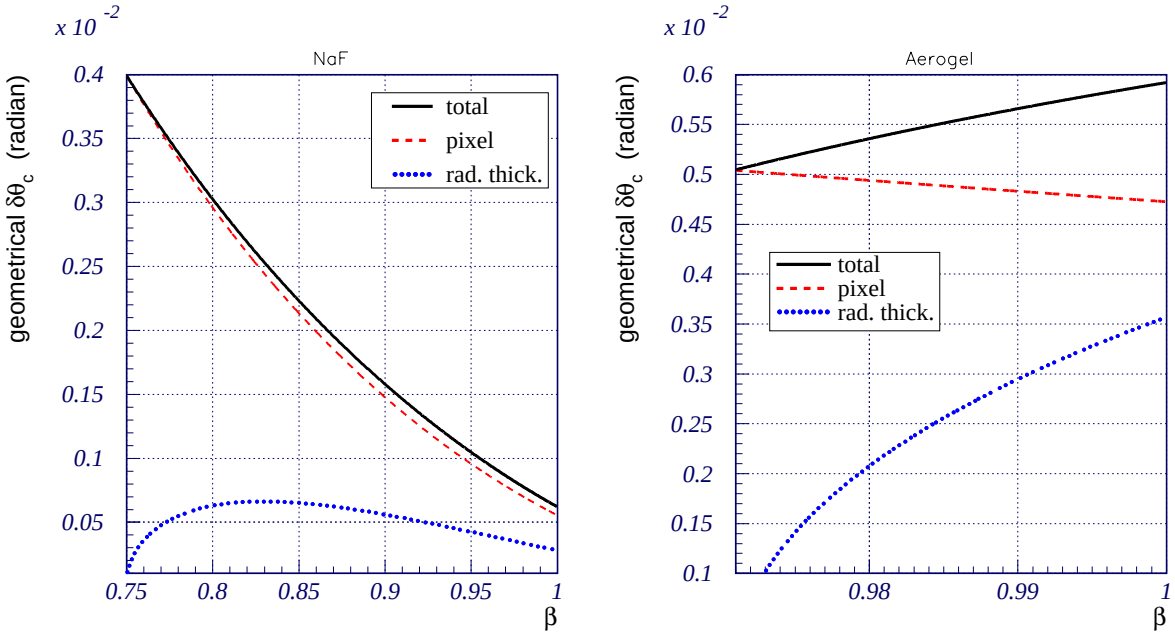

Figure 2.23: *Uncertainty of the reconstructed Cherenkov angle due to geometrical uncertainty sources only as function of the particle velocity. This result is obtained for the particle vertical incidence case. The two sources, pixel and radiator thickness, are represented.*

$\frac{\delta R^{\text{pixel size}}}{n\,\mathcal{R}(\theta_c)\,L + h/2}$ of eq. (2.7). The θ_c dependence therein explains why the pixel uncertainty contributions are different from the Aerogel to the NaF case.

In the same way, we call to the term $\cos^2\theta_c \frac{\delta R^{\text{rad.thick}}}{n\,\mathcal{R}(\theta_c)\,L + h/2}$ the radiator thickness contribution.

While the pixel contribution dominates in the $5mm$ NaF radiator, there is a significant contribution from the radiator thickness in the $3cm$ Aerogel case. Besides, the total geometrical error is much more large in the Aerogel than in the NaF case — 6 and 0.5 miliradian respectively.

The final uncertainty on the Cherenkov reconstructed angle is represented in the plots of figure 2.24, where the geometrical (pixel plus radiator thickness effect) and chromatic sources are separately depicted and summed. The scale of momentum per nucleon is in this case a better scale to compare the different curves obtained for the two radiators analyzed.

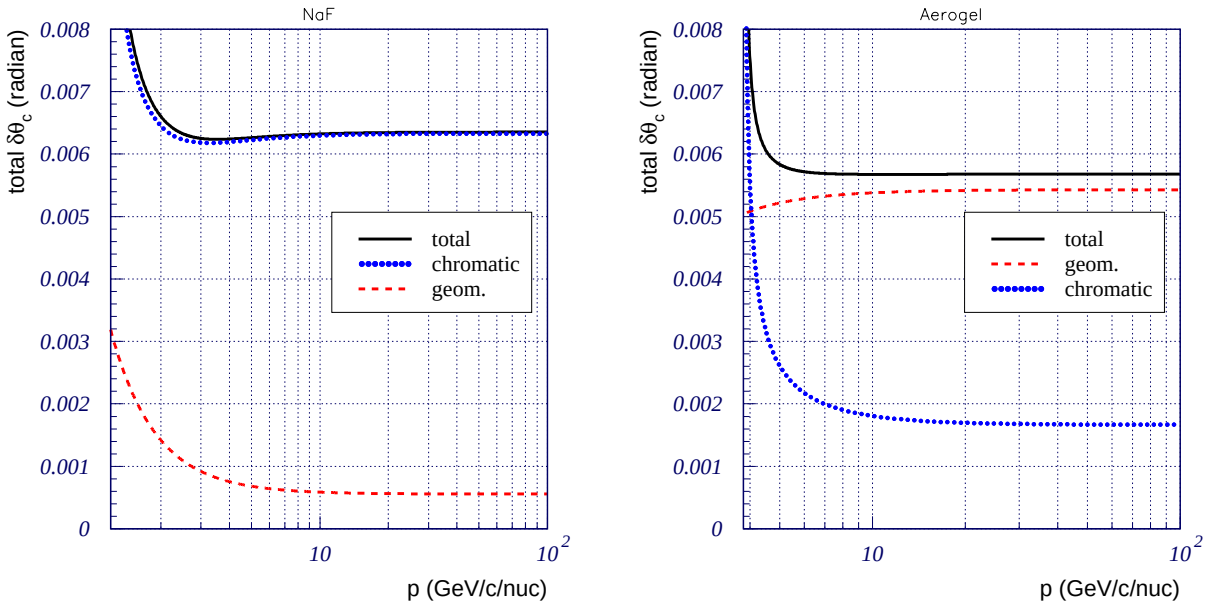

Figure 2.24: *Uncertainty on the Cherenkov reconstructed angle for a vertical incidence of the particle. The chromatic and geometrical components are separately plotted, together with their quadratic sum.*

The chromatic error completely dominates the final error in the NaF case. In the Aerogel, it is quite the inverse. It is interesting to note that we end up with two asymptotic errors quite comparable in both cases; slightly less than $6\,mrad$ for the Aerogel radiator and slightly more for the NaF radiator. We emphasize again that these values are the correct ones just in the case of particle vertical incidence. Some remarks on the geometrical effects of a non-vertical incidence are made in an addendum at the end of this chapter.

As stated in the beginning of this section, the error on the reconstructed velocity is given by:

$$\frac{\delta\beta}{\beta} = \tan\theta_c \, \delta\theta_c$$

It is this tangent dependence that completely separates the velocity resolutions for the two radiators setups here analyzed, giving the asymptotic resolutions of 1.4 and 5.6 for the Aerogel and NaF radiators respectively – see fig. 2.25. This is precisely the factor 4 discussed in the end of section 2.1.

As the Cherenkov reconstructed angle is a sort of average on the contributions of each detected photon on the Cherenkov pattern of the PMT matrix, the final error

will be lower than the single hit contribution just previously discussed [6]. Having N_{hits} detected photons on the reconstructed pattern, one expects the global error scaling according to:

$$\delta\theta_c(N_{\text{hits}}) = \frac{\delta\theta_c(\text{single hit})}{\sqrt{N_{\text{hits}}}}. \tag{2.9}$$

And so we have:

$$\begin{aligned} \text{For one hit} \;\rightarrow\; \frac{\delta\beta}{\beta}(\text{single hit}) &= \tan\theta_c\,\delta\theta_c\,(\text{single hit}) \\ \text{For } N_{\text{hits}} \text{ hits} \;\rightarrow\; \frac{\delta\beta}{\beta}(N_{\text{hits}}) &= \tan\theta_c\,\delta\theta_c(N_{\text{hits}}) \\ &= \frac{1}{\sqrt{N_{\text{hits}}}}\tan\theta_c\,\delta\theta_c\,(\text{single hit}) \end{aligned} \tag{2.10}$$

We will see the effect of this scaling with two different statistics sets provided by protons and heliums in chapter 4.

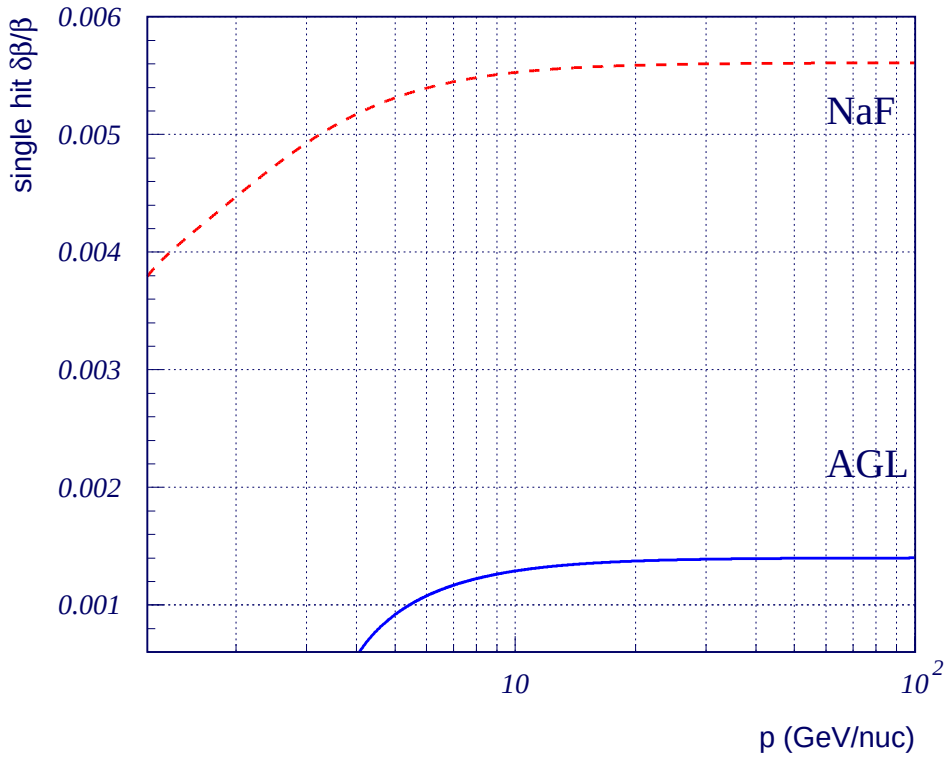

Figure 2.25: *Single hit relative error on the reconstructed velocity for the two radiators in analysis.*

[6] For any random variable, the error on the determination of its average scales with the number of used measurements (N), according to the proportionality factor: $\frac{1}{\sqrt{N}}$.

Non vertical incidence of the particle

In a cosmic rays experiment like AMS, particles come with varied directions — remember the polar angle distribution of fig. 2.9. In the more complex situation of a non vertical incidence, the polar angle of the Cherenkov photons vary with the azimuthal angle φ and so does the ring width δR on figure 2.26. Therefore, these two factors that enter equation (2.7) are to be changed in this more general situation[7]. In the remaining of this section, we'll give an idea of the change for the ring width due to the radiator thickness.

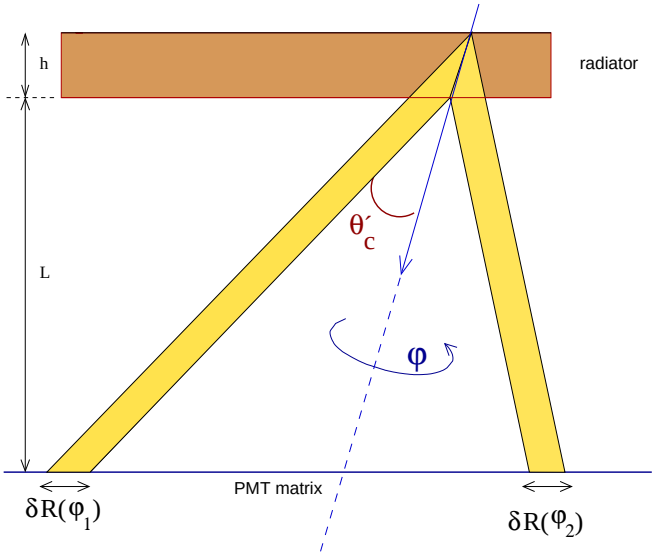

Figure 2.26: *In the situation of a non-vertical particle incidence, the thickness δR is a function of the azimuthal angle φ. We have for instance $\delta R(\varphi_1) > \delta R(\varphi_2)$. The effect of refraction is not reproduced in the draw.*

Besides the Cherenkov angle dependence existent in the vertical incidence situation, the polar angle of the particle direction (θ_p) and the azimuthal angle φ of the emitted photon also count to define the ring width, called H from now on.

Consider next figure 2.27, representing the particle track inside the radiator and a photon emitted at its top. Together with the radiator basis, these two line segments define a triangle to which we can apply the Cosines law to obtain the following relation:

[7]Remember that the polar angle of the photon at the detection matrix is implicit in eq. (2.7) and it is interpreted as defining an effective granularity.

$$H(\theta_c, \theta_p, \varphi) = \sqrt{d_p^2(\theta_p) + d_\gamma^2(\theta_c, \theta_p, \varphi) - 2\cos\theta_c \; d_p(\theta_p) \; d_\gamma(\theta_c, \theta_p, \varphi)} \; ,$$

where d_γ is the distance traveled by the photon inside the radiator and d_p is the corresponding distance for the particle. Each of these terms is given by [8]:

$$\begin{aligned} d_p(\theta_p) &= \frac{h}{\cos\theta_p}, \\ d_\gamma(\theta_c, \theta_p, \varphi) &= \frac{h}{\cos\theta_p \cos\theta_c + \sin\theta_p \sin\theta_c \cos\varphi}, \end{aligned} \tag{2.11}$$

where h is the radiator thickness.

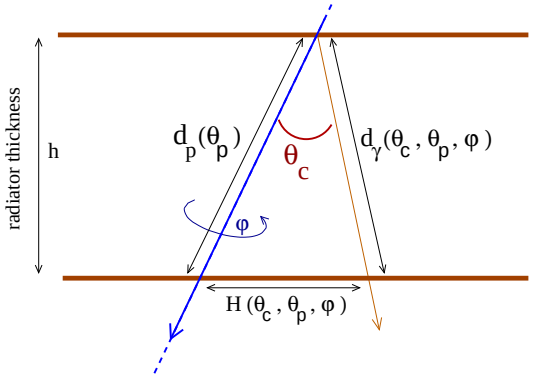

Figure 2.27: *Triangle used to compute the width of the Cherenkov ring due to the radiator thickness*

To have an idea of the azimuthal variation of the ring width, We can compute the function $H(\theta_c, \theta_p, \varphi)$ for a given particle direction (θ_p) and a given Cherenkov angle θ_c, and just letting free the azimuthal parameter φ to see how much this width function can change along the ring. That's what we plot in figure 2.28 for a polar angle $\theta_p = 20$ Degree and a Cherenkov angle corresponding to $\beta \sim 1$ and for the $3\,cm$ thickness Aerogel radiator.

We can eliminate the dependence on the internal variable φ by replacing $H(\theta_c, \theta_p, \varphi)$ by its average level, i.e. $< H(\theta_c, \theta_p) >= \frac{1}{2\pi} \int_0^{2\pi} H(\theta_c, \theta_p, \varphi)\, d\varphi$. Keeping β fixed, we can look at the remaining dependence on θ_p for this average thickness. This gives the left plot in figure 2.29.

We also can get an idea of what happens for the average ring width as a function of θ_c, with the particle direction fixed to the AMS mean value – $\theta_p = 20$ *Degree*. This is illustrated in the right plot of figure 2.29.

[8] Consult appendix B for a derivation of formula 2.11

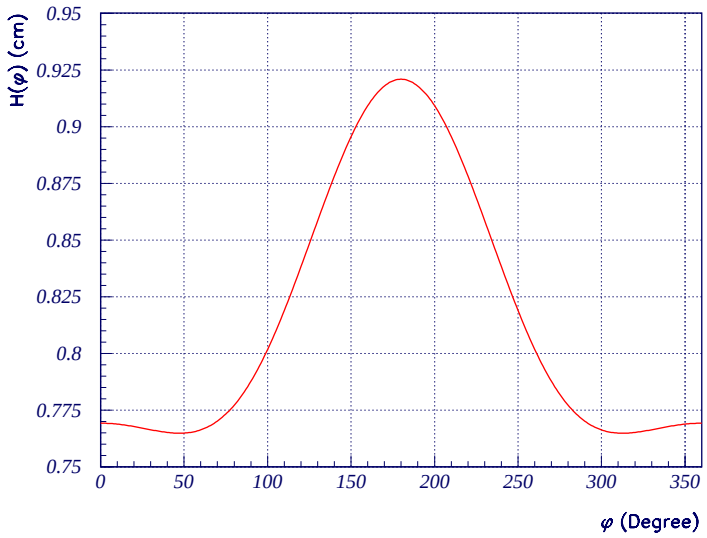

Figure 2.28: *Thickness of the ring as function of φ. This is for an Aerogel radiator of 3cm thickness, a particle velocity $\beta \sim 1$ and a polar angle $\theta = 20$ Degree.*

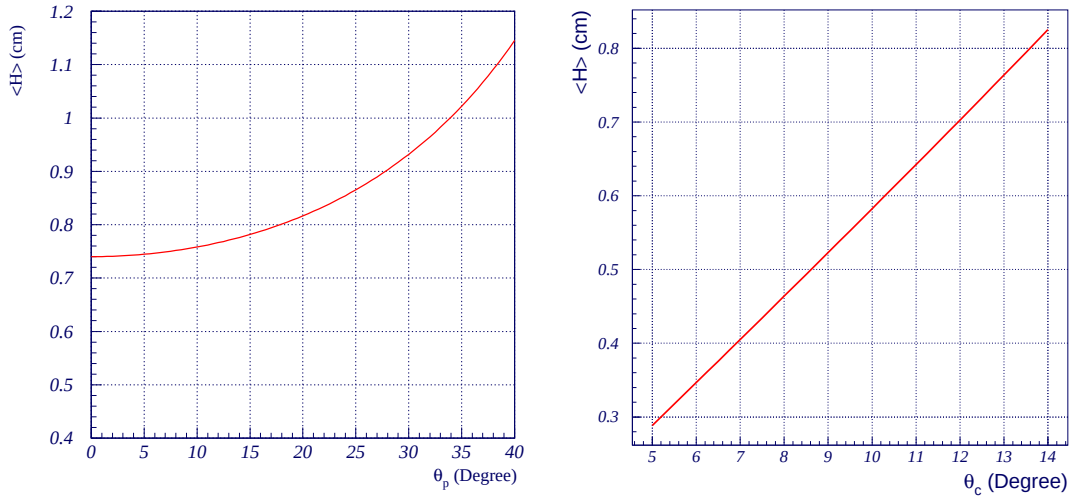

Figure 2.29: *Average ring thickness as function of the particle polar angle and as function of the Cherenkov angle. Left Plot: $\beta \sim 1$. Right Plot: $\theta_p = 20$ degree. The considered radiator is a Aerogel 3cm thickness.*

Note that the shown curves are computed by numerical integration, because the elliptic integral $\int H(\theta_c, \theta_p, \varphi)\, d\varphi$ is not expressible in terms of elementary functions.

The only purpose of the previous plots, in particular the left plot, is to show that it is reasonable to expect that some dependence on the particle polar angle θ_p can

exist for the resolution of the reconstructed Cherenkov angle.

Yet, this dependence is hard to work out exactly because of the non-analyticity of the obtained width function $H(\theta_c, \theta_p)$ and also because the propagation of this ring width error to the θ_c error is not the simple one of equation 2.7 anymore. This is why the effort to work out this eventual minor dependence on θ_p for the reconstructed θ_c was not pushed farther up.

However, as the ring width variation is not a big one, it shouldn't influence too much the result obtained for the vertical incidence case.

A last comment goes for why didn't the NaF radiator has been considered here. This is because in the NaF case, the previous integrations on φ should be done only inside a region of no internal total reflection.

Chapter 3

The reconstruction algorithm

3.1 The Reconstruction method

3.1.1 Pattern fit

The velocity measurement in a RICH detector is based on the Cherenkov relation that relates the particle velocity (β) with the Cherenkov angle (θ_c) and the refractive index of the radiator (n) :

$$\cos\theta_c = \frac{1}{n\beta} \tag{3.1}$$

On the other hand, the reconstruction of θ_c presented here, is based on a procedure that we can describe as the fit of a pattern curve to the detected hits; see fig. 3.1.

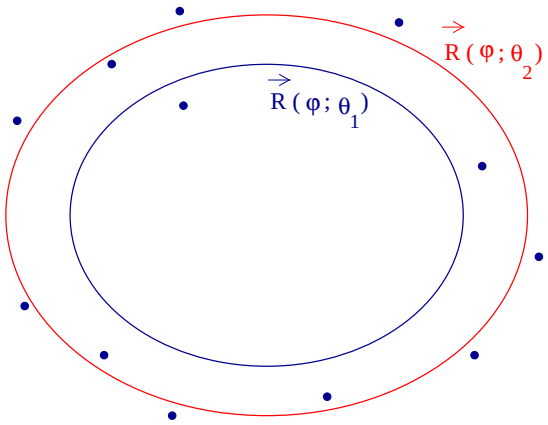

Figure 3.1: *Schematic illustration of the fit. Pattern associated with $\theta_c = \theta_2$ describes better the detected points than θ_1 pattern.*

This pattern can be regarded as a parametric function given by

$$\overrightarrow{R}_{pat}(\varphi\ ;\theta_c) = \{X_{pat}(\varphi;\theta_c), Y_{pat}(\varphi;\theta_c)\}, \quad 0 < \varphi < 2\pi$$

where $\{X_{pat}, Y_{pat}\}$ are the coordinates for the points of the curve parametrized by φ, and θ_c will play the role of the only free parameter for the fit.

The procedure developed to construct these patterns can be summarized as a parametric tracing of the trajectories of the Cherenkov photons in a simplified framework where all of them are emitted at a single point inside the radiator. In order to have a clearer picture of the pattern tracing procedure itself and for a better understanding of what follows to implement the fit, let us analyze it in some more detail.

A given kinematics configuration of the mother particle is described by 6 parameters: the spherical angular coordinates $\{\theta, \phi\}$ together with a point $P_v = \{x_v, y_v, z_v\}$ specify the trajectory. The velocity is given by θ_c. In our framework, all the photons will be emitted at P_v; see figure 3.2.

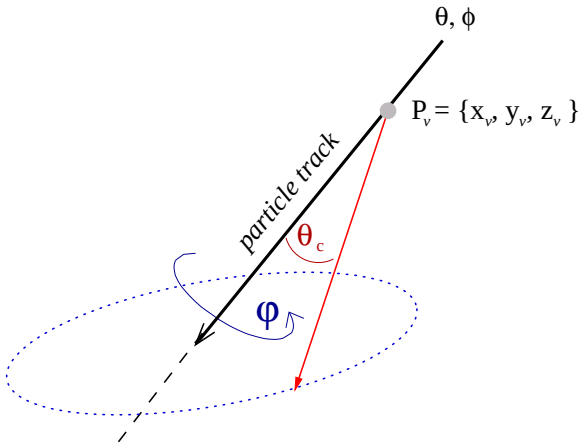

Figure 3.2: *Illustration of the photon tracing. Assigning values to the particle trajectory parameters* $\{x_v, y_v, z_v, \theta, \phi\}$*, each photon is parametrized by* θ_c *and the azimuthal angle* φ*.*

With the knowledge of the particle trajectory parameters, and for a given value of θ_c , each photon trajectory is parametrized by a single azimuthal parameter φ ($0 < \varphi < 2\pi$). The meaning of this azimuthal angle φ is well depicted in fig. 3.3. The photons trajectories are followed through the detector, up to their impact points in the detection matrix.

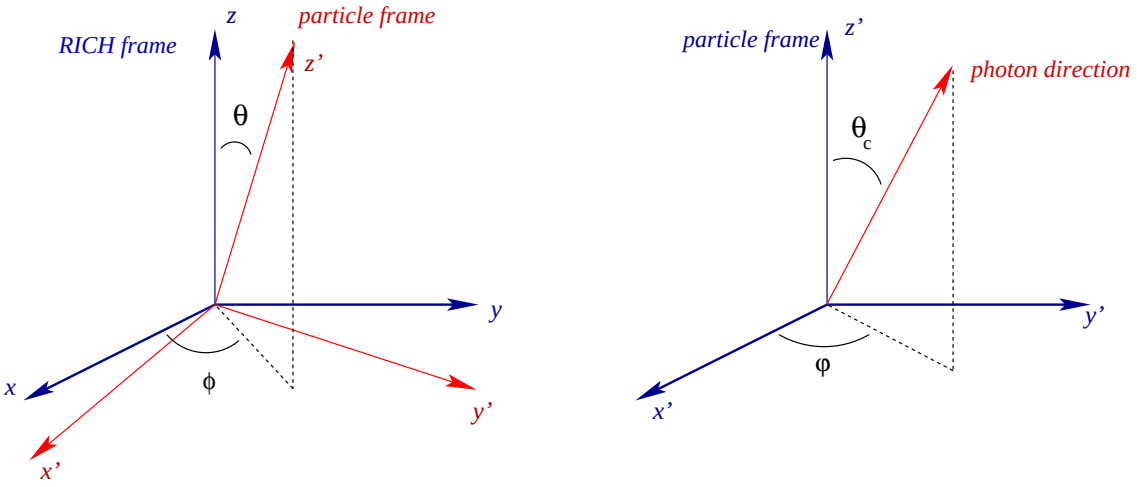

Figure 3.3: *Illustration of the two frames involved in the photon tracing. φ is the usual azimuthal angle for the photon direction, when expressed in the particle frame.*

It is the intersection of these trajectories with the detection matrix that constitutes our Cherenkov fitting pattern. Two of these patterns are illustrated in fig. 3.4 of next page.

This photon tracing takes into account refractions in the transition between the radiator and the vacuum of the expansion volume. Reflections in the conical mirror are also performed whenever necessary (in a high refractive index radiator like NaF, multiple reflections are usual). The tracing can thus be seen as a procedure that takes φ as the input and gives the corresponding detection point in the matrix $\{x_d, y_d\}$ as the output. For details on these calculations constituting the support of this tracing procedure, please consult thesis [16].

With such a tool in hands, one can compute the distances between the data points and a given pattern. The most natural *figure-of-merit function* for measuring the agreement between the data (hits positions) and our pattern for a given choice of θ_c could be a kind of Chi-squared function like:

$$\chi^2(\theta_c) = \sum_{i=1}^{N} {r_i}^2(\theta_c) \ , \ \text{where } r_i \text{ is the residual (distance) for point \# } i \qquad (3.2)$$

which is simply the sum of the squared residuals between the data points and the pattern of θ_c aperture.

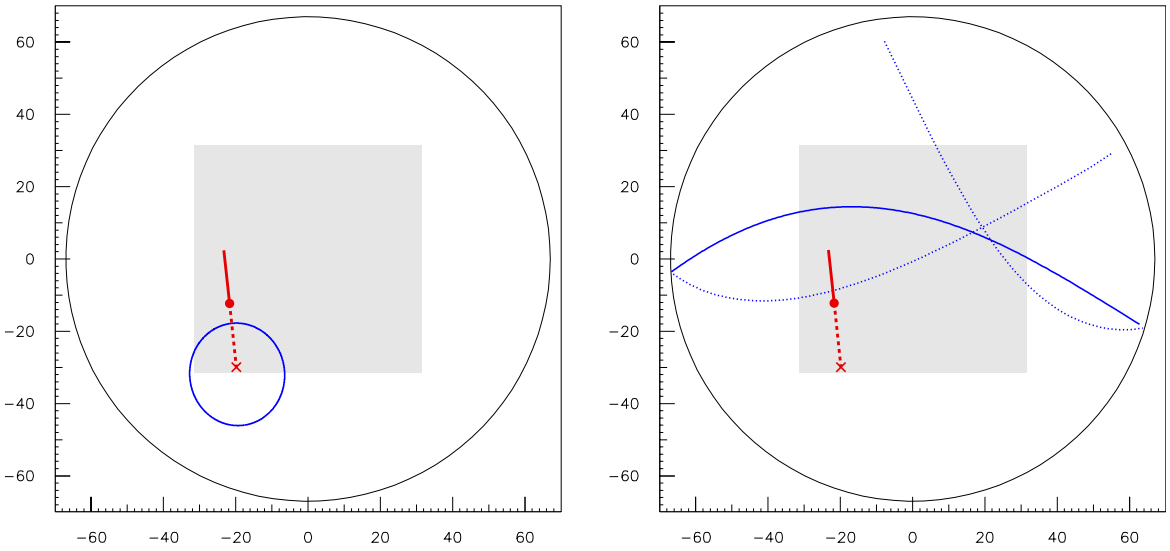

Figure 3.4: *Two patterns for the same particle kinematics (β = 0.9999 and θ = 20 Degree. The particle track projection is depicted by the dashed line. On top of it, the symbols • and × indicate the positions at the radiator top level and at the detection matrix level respectively.* Left *pattern corresponds to an Aerogel radiator with a refractive index n=1.03.* Right *pattern corresponds to a NaF radiator with n=1.334 . The shadowed central area indicates the dead area over the electromagnetic calorimeter of AMS (ECAL). The scale of this display is given in centimeters.*

This approach is directly inspired in the Minimum Least Squares fit method. The goal is to find the minimum of this function that turns out to be our estimation or reconstruction for θ_c. Before going on the exploration of our *merit function*, let us say something more about the computation of the distances r_i.

The first observation is that due to the effect of the refraction that is dependent on the incidence direction of the photon (that changes with φ), not to talk about the reflections in the conical mirror, one gets a pattern curve that contrarily to what could be has been suggested before, is not analytically expressible in any of the the following forms: be it *parametric* — $\overrightarrow{R}(\varphi)$ — or be it *Cartesian* — $f(\overrightarrow{R}) = 0$, where $\overrightarrow{R}$ denotes the points (x, y) of the pattern curve.

For this reason, the computation of the distance between any point and the pattern curve can not be done by using an analytical minimization technique like Lagrange multipliers one that we find in the calculus textbooks to solve some classical extrema problems with constraints.

The followed approach has thus been to define a distance function $d_i(\varphi)$ for each point P_i and for each θ_c; note that the remaining parameters on which the pattern curve depend on - $\{\theta, \phi, P_v\}$ - are known constants for each event fit.

It turns obviously out that this distance function is no more analytical than the pattern curve and so the distance has to be computed by numerical minimization! In the figures of pages 46 and 47 (figs 3.6 and 3.7), we can appreciate the aspect of such a distance function that corresponds to the length of different lines joining our hit point to the pattern. This way we clearly see that as θ_c changes along the minimization of $\chi^2(\theta_c)$, the distance function for each hit can change in a drastic manner; going from the easy situation of only one minimum to the algorithmically more complicated one of finding out the absolute minimum from several minima.

At this point a careful and critical observer could argue that the distance of the hit to the pattern, computed as previously described is not the physical quantity that should be considered. Let's see how.

Figure 3.5 depicts a photon track or better saying its projection on the detection matrix . $P_v^{'}$ is the projected emission point and P_d is the detection point . A schematic pattern is also represented. The distance that we compute in the above description is $d_{\min}$; it is the minimal distance between the photon hit point P_d and the pattern curve. The above referred critical observer can say that for the illustrated pattern the expected hit point would be A instead of B and thus the considered distance should be d_{phys} instead of $d_{\min}$.

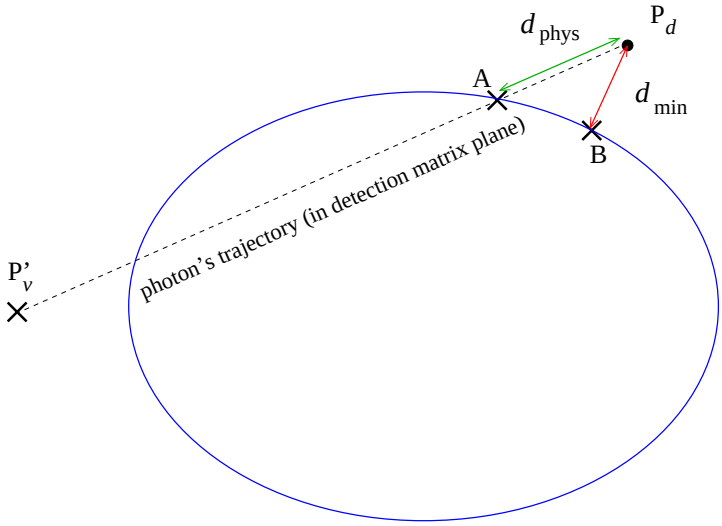

Figure 3.5: *Illustration of two possible distances between the hits and the Cherenkov pattern. d_{phys} is the distance from point P_d to the depicted pattern measured in the photon track projected direction. d_{min} is the minimum distance from P_d to the pattern.*

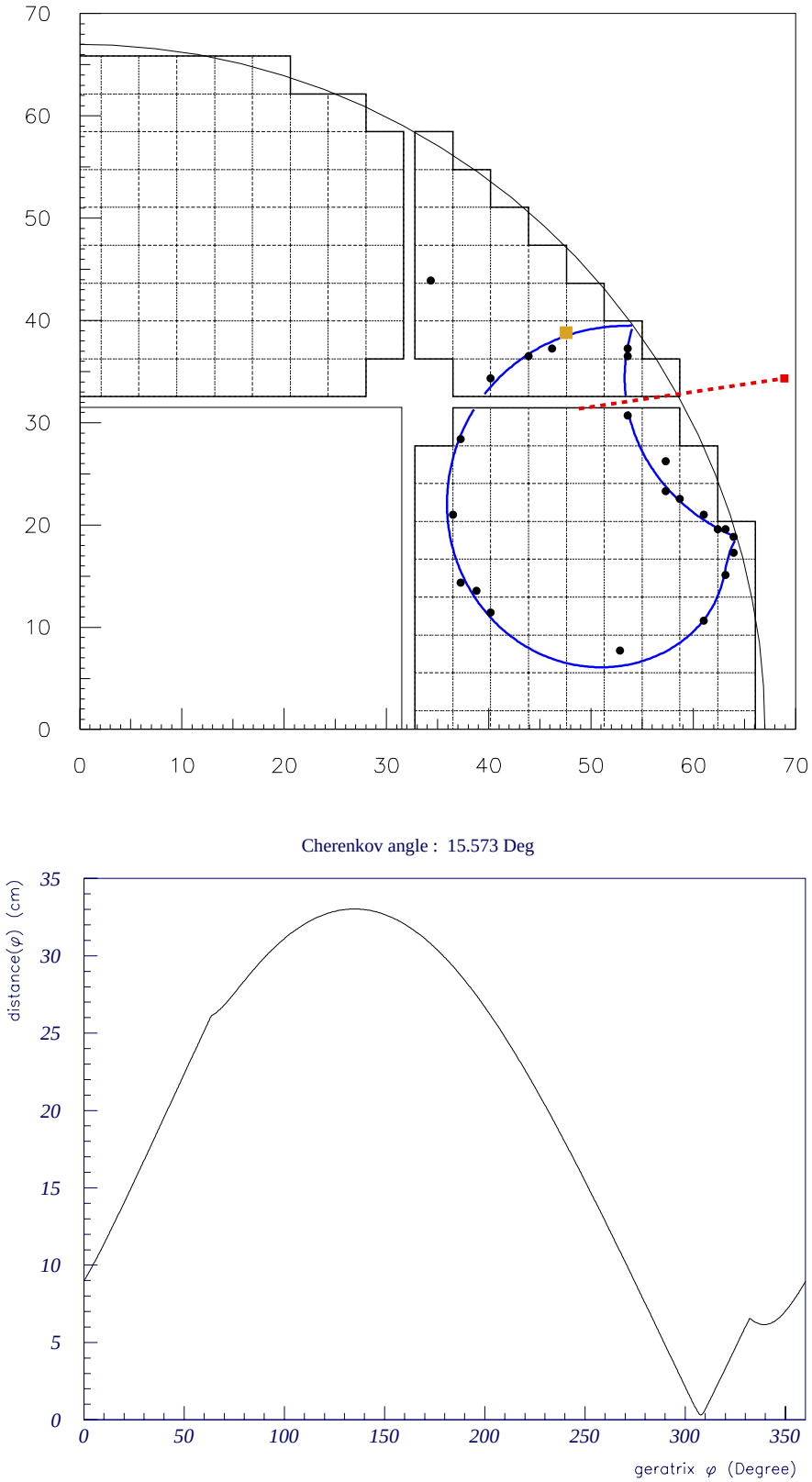

Figure 3.6: *For a simulated event depicted in the top figure (with an expected pattern* $\theta_c \sim 15.57$ *Degree), the azimuthal distance function to the pattern for the hit marked by a square (in lighter color) is given in the bottom plot.*

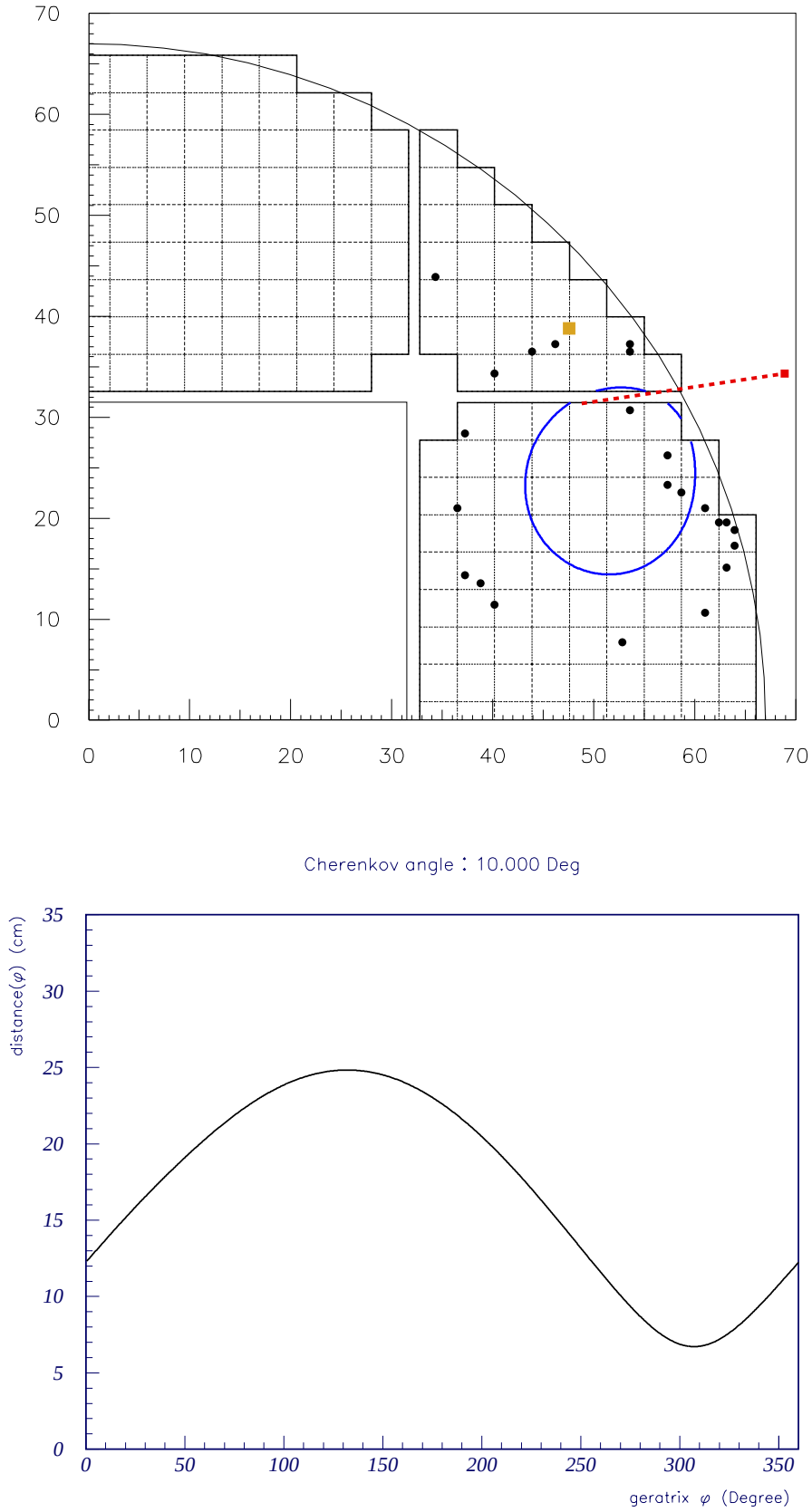

Figure 3.7: *For the same event and same hit of fig. 3.6, we indicate in the bottom figure the distance relative to the pattern of 10 Degree given of the top figure.*

The first answer to this careful reader is that given the small distances in question, the difference between the two above referred distances is negligible and so it must be for the corresponding merit functions. The second and most fundamental reason is that in this pattern framework, the natural concept to define is $d_{\min}$, because it has a clear and straight-forward computable meaning as opposite to d_{phys}.

Let us now return to our merit function $\chi^2(\theta_c)$ minimization. Due to the Rayleigh scattering and the occasional PMT noise, some hits come up far distant from the good hits and the expected pattern as one can see for instance in figure 3.8.

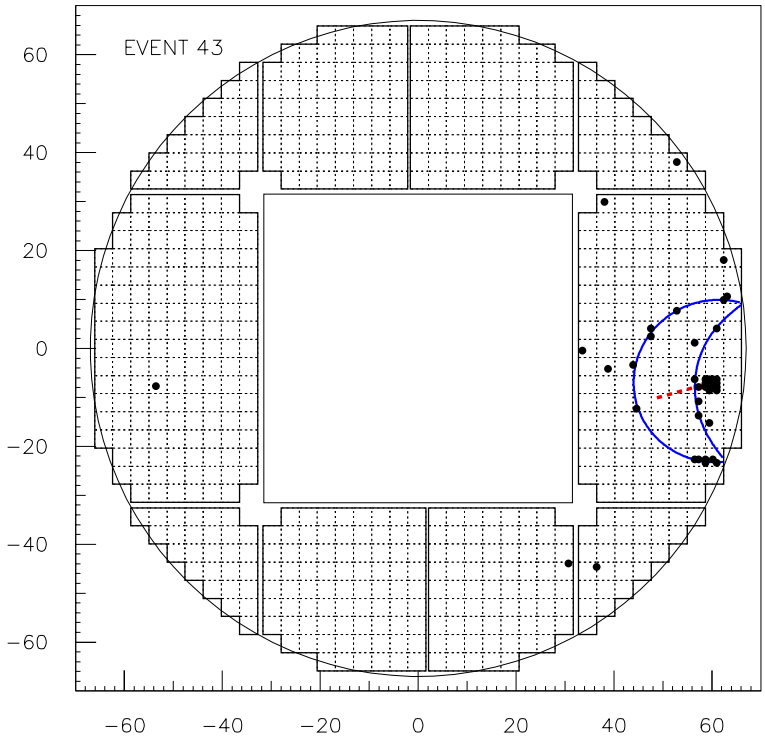

Figure 3.8: *A visual illustration the hits spreading in the RICH PMT matrix of AMS. This spread is essentially due to the scattering of light in Aerogel. This picture corresponds to a simulated helium with $\beta = 0.999$ in a 1.05 Aerogel radiator of clarity 0.009 $\mu m^4/cm$.*

In the language of Robust Statistics, these points are said to be *outliers* for the fit procedure that would completely bias the estimation if considered in the fit. A cut-off has thus to be introduced in the function of eq. (3.2), resulting in the following merit function:

$\sum_{i=1}^{N} {r_i}^2(\theta_c)H(r_i)$, where H is the usual step function defined by

$$H(x) = \begin{cases} 1 & \text{if } x < \text{cut-off value} \\ 0 & \text{otherwise} \end{cases}$$

This procedure works but suffers from a drawback that is inherent to the discontinuous character of the merit function now produced. As the free parameter θ_c changes along the fit, the set of hit points entering the computation also changes and this happens in the same abrupt way as our cut-off step function changes.

As everyone who has been involved with the task of numerical minimization knows, discontinuities are an unpleasant feature that can mimic a minimum for the minimization search algorithm. For who doesn't, see bottom plot of figure 3.12 on page 56.

The ideal would then be to weight the hits according to their distances to each trial θ_c pattern during the fit. An approach that does this in a natural way is the *maximum likelihood* approach in which one assigns a probability for each point entering the fit. Given a random variable x distributed according to a probability density function $f(x\,;\theta)$ with a known form but unknown parameter θ one can ask for the question "*what is the value* $\hat{\theta}$ *that best describes a set of of measurements for the* x *variable, say* $\{x_i\,, i = 1, N\}$". The answer to this question is given by the maximum likelihood estimate. This estimate is given by the value $\hat{\theta}$ that maximizes the product

$$\prod_{i=1}^{N} f(x_i\,;\theta)$$

that is here considered as a function on θ called the Likelihood function $\mathcal{L}(\theta)$[1].

3.1.2 Likelihood approach

In the framework of this *Likelihood approach*, the parameter to estimate is θ_c and the random variable x is replaced by the residual of a hit to the currently considered

[1]For the more curious reader about the probabilistic fundamentals of this technique, please consult the addendum "Bayes Theorem and the Maximum Likelihood method" at the end of this section.

θ_c pattern just as described before. Then we can write our likelihood function as

$$\mathcal{L}(\theta_c) = \prod_{i=1}^{N} \mathcal{P}\{r_i(\varphi(\theta_c))\} \tag{3.3}$$

where $\mathcal{P}$ is the p.d.f. followed by the residuals r_i. $\mathcal{P}(r(\theta_c))dr$ describes the probability of a hit being at distance R from the expected pattern associated to θ_c such as $r < R < r + dr$.

The minimization on φ, needed for the computation of each residual, is stressed out by writing the dependence on φ: $r_i(\theta_c) = r_i(\varphi(\theta_c))$. For numerical reasons, one minimizes the function $-\log \mathcal{L}(\theta_c)$ which is perfectly equivalent to the maximization of (3.3)[2].

Now the only missing ingredient is finding the correct p.d.f. $\mathcal{P}(r_i)$. By the look of figure 3.9 in next page, in which we show the histogram of the expected residuals — residuals computed relatively to the expected θ_c pattern — we can get a qualitative idea of the p.d.f. we need.

If it was not for the noise hits completely uncorrelated with the pattern, essentially due to the Rayleigh scattering (remember fig. 2.12 in chapter 2), a reasonable assumption would certainly be to consider the Gaussian distribution. Indeed, this Probability distribution underlies the likelihood formulation for the Least Squares fit method.

To take into account these far away hits, not described by the very low tail of a Gaussian, one can simply add a function $\mathcal{P}_{noise}(r)$, so that our global p.d.f. is given by

$$\mathcal{P}(r) = \mathcal{P}_{signal}(r) + \mathcal{P}_{noise}(r) \ .$$

This p.d.f. considers so the possibility for the hit being due to the real Cherenkov signal or being just noise. A choice that turns out to be fairly good for $\mathcal{P}_{noise}(r)$ is the constant function. Let's see how this comes up.

Starting from a mean number of hits N, one can decompose it in a mean number of signal hits S and a mean number of background hits B as follows,

$$N = S + B \qquad \text{or equivalently,} \qquad 1 = \frac{S}{N} + \frac{B}{N}. \tag{3.4}$$

[2]The logarithm operation doesn't change the place of the minimum $\hat{\theta}_c$. It is only performed to enlarge the curvature of the function near the minimum.

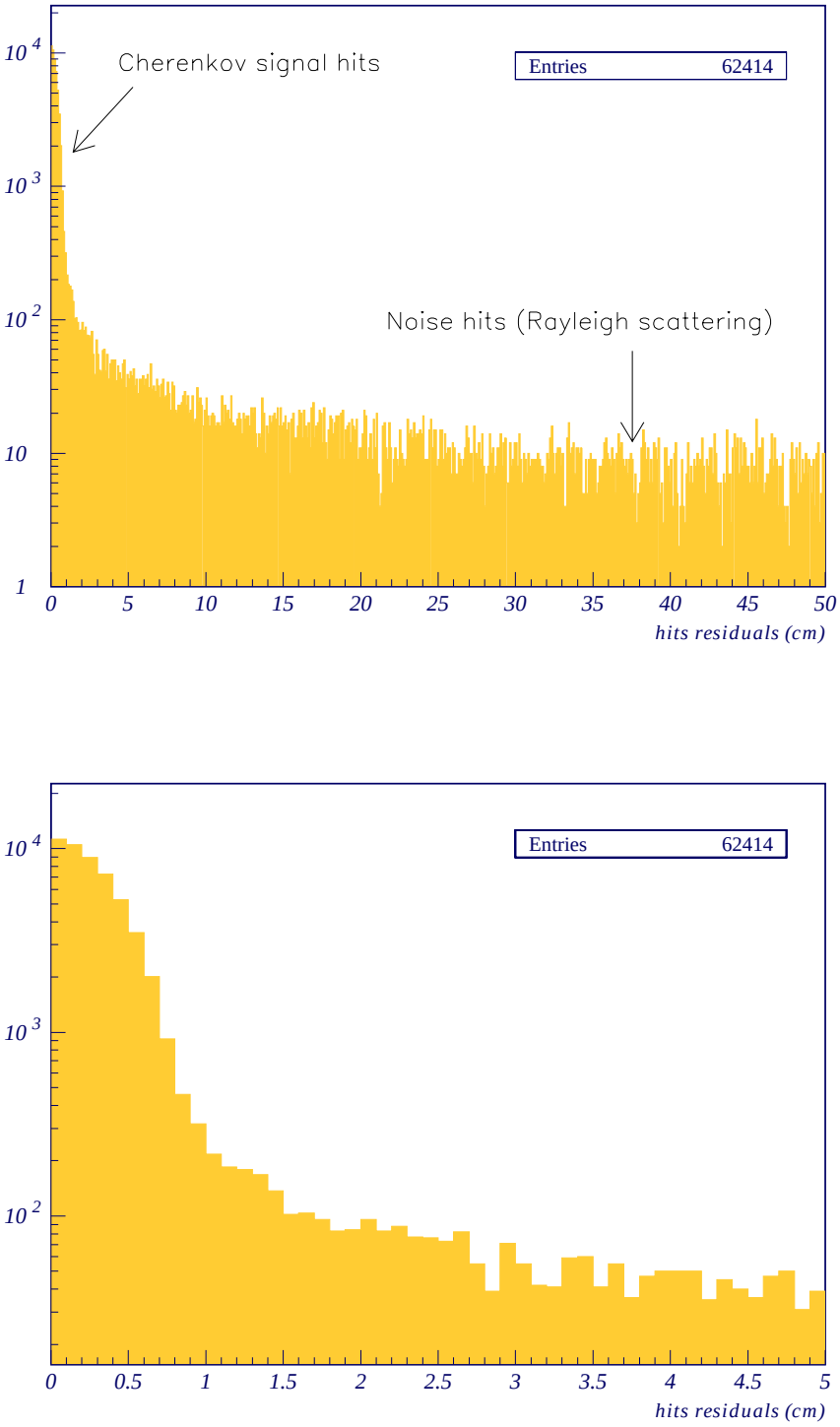

Figure 3.9: *Hits residuals (to expected pattern) for 5000 simulated events in all AMS acceptance. Top histogram shows how far the hits can be from the expected pattern. Bottom histogram is a "zoom out" from the top one.*

Now, the simplest assumption to do is to assign an 'individual' p.d.f. to each of these parts, signal and background, and simply write down the differential counterpart of eq. (3.4) as

$$\mathcal{P}_{total}(r) = \frac{S}{N}\,\mathcal{P}_{signal}(r) + \frac{B}{N}\,\mathcal{P}_{noise}(r)\ . \tag{3.5}$$

This total probability density function must be normalized to 1:

$$\int_0^D \mathcal{P}_{total}(r)dr = 1.$$

On the other hand, by using condition (3.4), we have the separate normalization conditions

$$\int_0^D \mathcal{P}_{signal}(r)dr = 1 \qquad \text{and} \qquad \int_0^D \mathcal{P}_{noise}(r)dr = 1\,, \tag{3.6}$$

where D represents the maximum distance from a hit to the pattern. This can be taken as representing a length that is about the diameter of the detection matrix ($D \sim 100\,cm$).

We can rewrite (3.5) in the following simpler form:

$$\mathcal{P}(r) = (1-b)\mathcal{P}_{signal}(r) + b\,\mathcal{P}_{noise}(r)\,, \tag{3.7}$$

where we have adopted the definition $b = \dfrac{B}{N}$. From now on, this parameter is called the mean background ratio or shortly background ratio.

For the signal, one makes the already referred choice of the Gaussian form[3]

$$\mathcal{P}_{signal}(r) = \frac{1}{\sigma}\sqrt{\frac{2}{\pi}}\ \exp\left[-\frac{1}{2}\left(\frac{r}{\sigma}\right)^2\right].$$

The normalization condition for $\mathcal{P}_{noise}$ constrains its functional form to be that of a simple constant function, which value ($\frac{1}{D}$) also comes out from it.
Absorbing the constants $(1-b)$ and b in the definition of the partial p.d.f's one

[3]The factor 2 relatively to the usual normalization coefficient is due to the strictly positive domain of integration. It also must be noted that in view of the condition $D >> \sigma$, the integration in (0, D) is equivalent to (0, $+\infty$).

finally gets

$$\mathcal{P}(r) = \mathcal{P}_{signal}(r) + \mathcal{P}_{noise} \tag{3.8}$$

$$\text{with} \quad \mathcal{P}_{signal}(r) = \frac{1-b}{\sigma}\sqrt{\frac{2}{\pi}}\exp\left[-\frac{1}{2}\left(\frac{r}{\sigma}\right)^2\right] \tag{3.9}$$

$$\text{and} \quad \mathcal{P}_{noise} = \frac{b}{D} \ . \tag{3.10}$$

Next, the p.d.f. parameters b, σ, D are evaluated, using again the same residuals distribution of fig. 3.9. The parameter D is taken as 100 cm, which corresponds to the domain on which 99.75% of the referred residuals fall into.

The background ratio b is evaluated using the more or less flat part of the distribution. We compute a mean level for this part and correct it by a factor 1.02 (corresponding to the fact that we have used only 98% of the distribution domain to integrate the background). The obtained value is about 17%.

The fitted Gaussian to the signal part of the distribution has a sigma width of about 0.3 cm. With these parameters, the resulting p.d.f. is plotted on top of the residuals distribution in figure 3.10.

Some comments are required to discuss some aspects of the p.d.f. that we have just constructed. By looking at the plot of fig. 3.10, one notices that the transition between the Gaussian part and the background is smoother in the residuals than it is allowed by our model. Secondly, it is clear that the background residuals distribution is not exactly flat if we look it up to its limit (fig. 3.11).

At this point, we should be conscious that our simple model to describe the residuals distribution certainly doesn't take into account certain secondary effects. The effect of the patterns with reflected branches can deform our assumptions in a non trivial way. The approximation of taking a single emission point for the Cherenkov photons instead of a extensive emission across all the radiator thickness may also distort this residuals distribution and so on.

Nevertheless, the important aspects of the residuals distribution, i.e., the Gaussian shaped signal and the magnitude of the background tail, are well reproduced. Besides, the regions where these mis-adjustments occur are 2 to 3 orders of magnitude less populated than the Gaussian region where our signal stands. So, even if a better description could be found, it would not be of a great importance, because the amount of added information would be negligible.

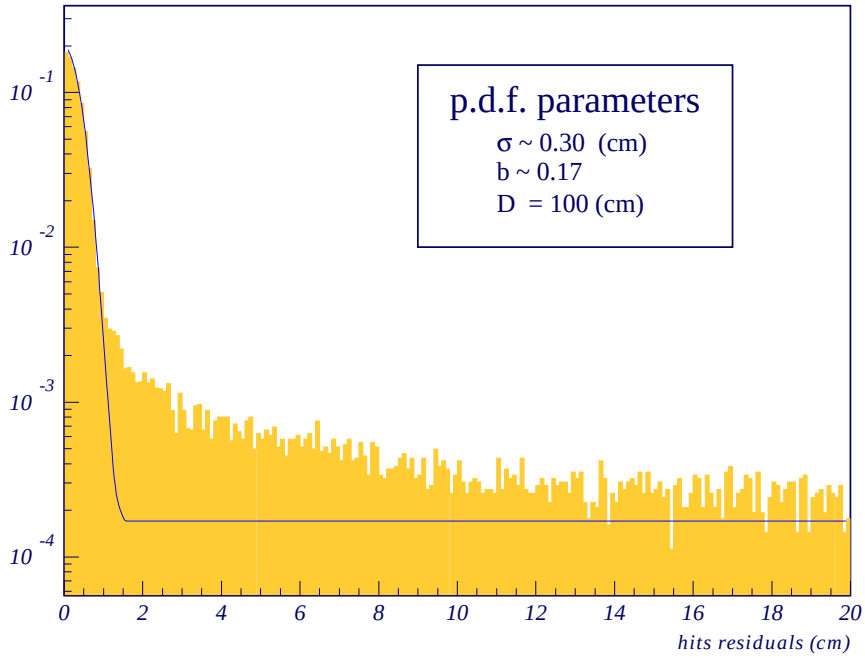

Figure 3.10: *Residuals histogram (same of figure 3.9), here normalized to the unit, with the likelihood p.d.f. plotted on top of it.*

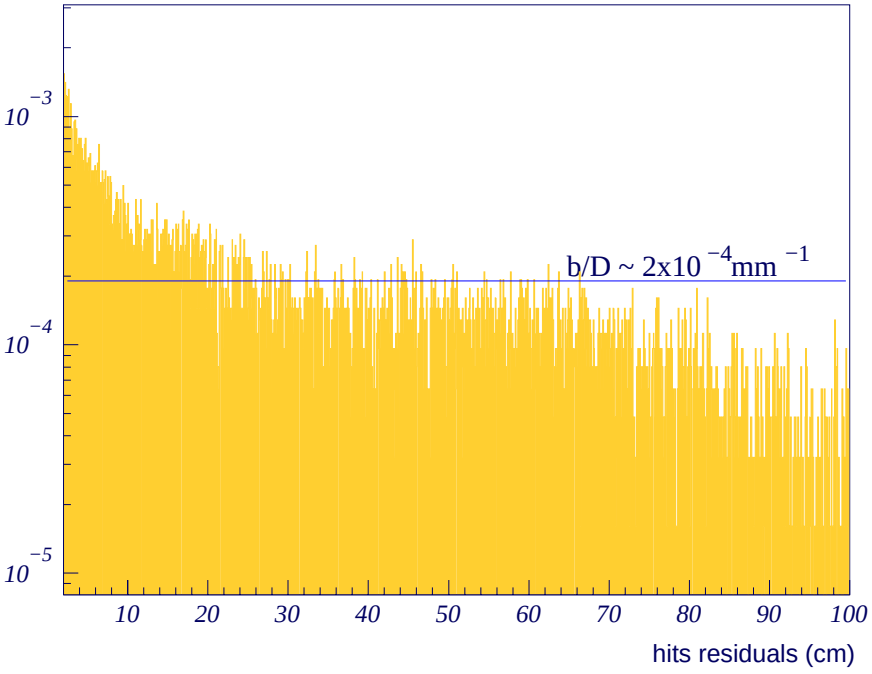

Figure 3.11: *"zoom out" to fig 3.10. We note here that our flat background assumption is an average.*

So, the flat model for the background can be considered to be enough for our purpose, that is to avoid a bias of the fit by using the remote hits with the same weight than the close ones.

Now another remark is that the values of the p.d.f parameters σ and b depend on factors characterizing the detector. The radiator clarity affects the background ratio parameter. The pixel size and the radiator thickness affects σ.

Another factor is the known precision for the particle track. Because the particle track constitutes the axis of the Cherenkov cone associated to the traced pattern, it is clear that an inaccuracy resulting from the finite precision present in real life, results in a not so accurate pattern as in the ideal situation of this simulation that doesn't include the smearing of the particle track.

However, it has been verified by a scanning kind of study, where these p.d.f. parameters were changed, that the result of the fit is not too much sensitive to these p.d.f parameters values [4].

Another point that is already worthwhile to mention is that this likelihood p.d.f. naturally gives us the distance "window" where the hits that entered the fit have a significant weight. This counting "window" is the 3 sigmas of the Gaussian (or 4 if one wants to use a more conservative posture about the value). Later on, we will speak of the hits on the Cherenkov reconstructed ring as being the hits in this residuals "window".

To conclude this section, we can see in the following figures an illustration of what has been the improvement in going from the minimum least squares technique to the maximum likelihood approach. In the top plot of figure 3.12, we can visualize what our merit function ($-\log \mathcal{L}(\theta_c)$) looks like for the event that we have already used to illustrate the distance functions for the hits (fig. 3.6). Despite the presence of several minima, the function is very smooth and presents a clear absolute minimum in the expected value of θ_c . For the case of the Minimum Least Squares merit function previously exposed, we would obtain the not so nice bottom plot.

As a final remark of the method description, it should be added that just like in the minimization to compute each hit distance to the pattern, we face again with the problem of finding the absolute minimum from a set of local minima. This turns

[4]See the presentation "Beta reconstruction Algorithms and Results on Prototype data" in the URL site `http://ams.cern.ch/AMS/analysis.html`

out to be the major computing difficulty, for a very exhaustive search algorithm has to be performed in order to be sure to have found the absolute minimum.

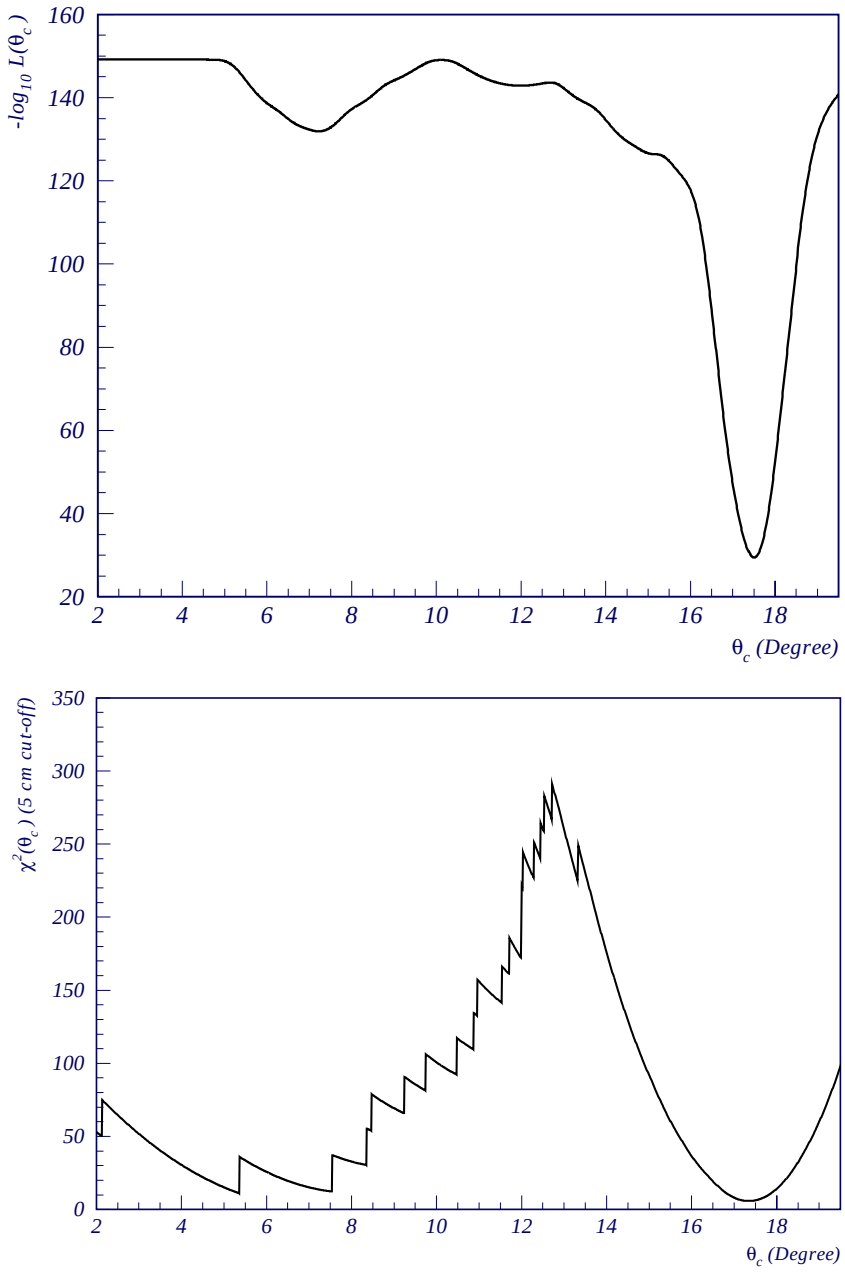

Figure 3.12: *(Top figure) Likelihood merit function for the event of fig. 3.6. (Bottom fig.) Chi-squared merit function for a cut-off of* 5 *cm for the same event.*

3.2 Additional remarks and optimization of the reconstruction

3.2.1 The hits of the particle in the Light Guide

Before proceeding to other questions of the reconstruction, let us point out an obvious but important remark. This has to do with the huge production of Cherenkov photons in the RICH light guides when these are crossed by the particle. Clusters of several hits in a very small area (about one PMT) comes ups, because of the high refractive index of these light guides ($n = 1.49$), which produces about 10 times more photons per unit length than Aerogel of mean refractive index 1.03 (and 6 times more than Aerogel 1.05). The point is we don't want to use these hits in our fit to the Cherenkov pattern. The reconstructed event Display of figure 3.14 shows what would be the effect of not taking this feature into account.

So, we reject the hits that are closer than 5cm from the particle impact point at the readout matrix (this is an extrapolated point, by using the track information, just like we did for the vertex of our tracing).

However, the reader can think of a role that could be conferred to these hits, namely, to confirm the track information used by the pattern tracing. In fact, in the analysis of the prototype data presented in chapter 5, we use such a procedure.

There is a practical issue related to the size of the particle cluster region. This has to do with the lower reconstructible Cherenkov angle. In the θ_c scan procedure that we use to guarantee the absolute minimization of the merit function, we restrict it to the domain of 6 Degree to 10% more than the maximum Cherenkov angle. This minimum value is the Cherenkov angle giving a pattern with an average radius of 5 cm.

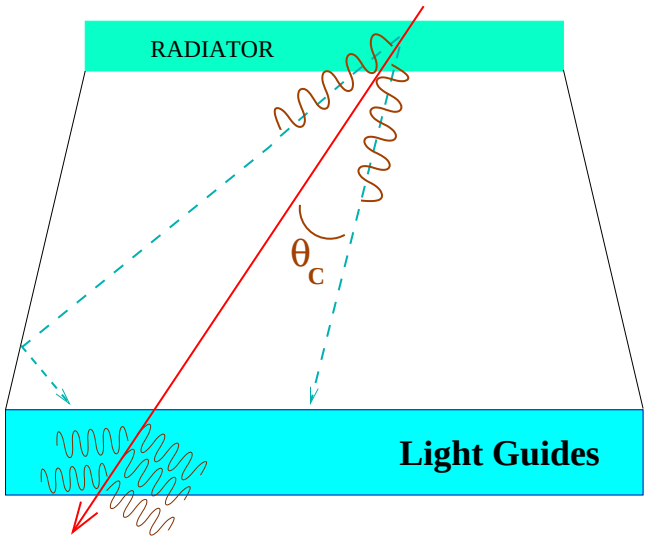

Figure 3.13: *The Cherenkov photons radiated in the light guides don't give rise to a geometrical and reconstructible pattern.*

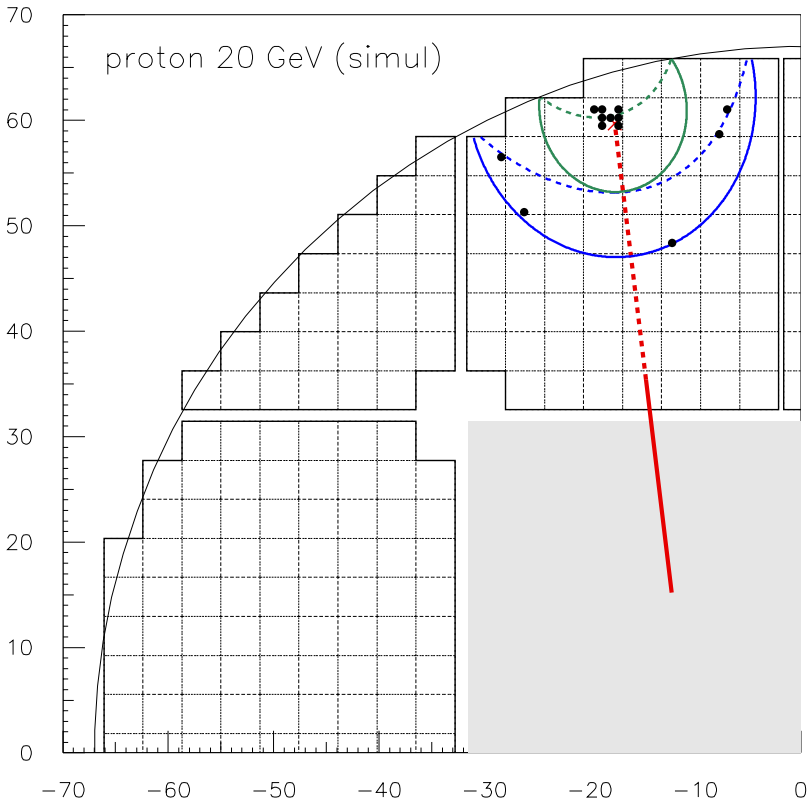

Figure 3.14: *Effect of the particle hits on the pattern fit. If the particle cluster hits were not removed from the points to fit, the reconstructed pattern would be the inner one, instead of the (well visible) expected one.*

3.2.2 Photon emission point

It is easy to expect that the choice of the origin for our photon tracing, i.e. the assumed photon emission point used to reconstruct the Cherenkov angle, is a parameter that introduces a systematic error if not well chosen. This is illustrated by the schematic draw of fig 3.15, where it is obvious than the lower this point is chosen the larger will be the reconstructed Cherenkov angle.

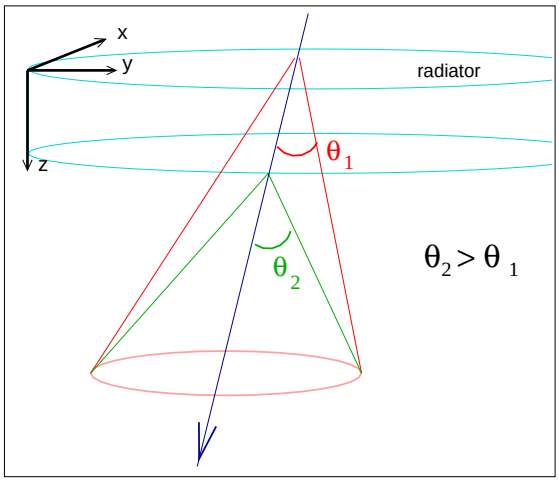

Figure 3.15: *Illustration of the emission point effect on θ_c reconstruction. Moving the emission point from the top to the bottom of the radiator necessarily leads to different reconstructed angles: θ_1 and θ_2.*

What we show in the following is the tunning study for this emission point parameter. The emission point being constrained to be along the particle track, we have just one degree of freedom, say the z coordinate or better the z coordinate divided by the radiator thickness (this way, our parameter varies between 0 and 1).

For this tunning study, the reconstruction was repeatedly ran upon a certain sample of simulated events inside all RICH acceptance, by just varying this parameter and taking a look into the resulting reconstruction. What we obtain is summarized in figure 3.16 and table 3.1. This was obtained for a simulation of an Aerogel radiator with a refractive index n=1.03, a clarity of 0.009 $\mu m^4\ cm^{-1}$ and $3cm$ thickness. We can see that the systematic error on the reconstructed θ_c changes linearly with the chosen emission point. Figure 3.17 allows a direct comparison between the systematic error (in absolute value) and the statistical error.

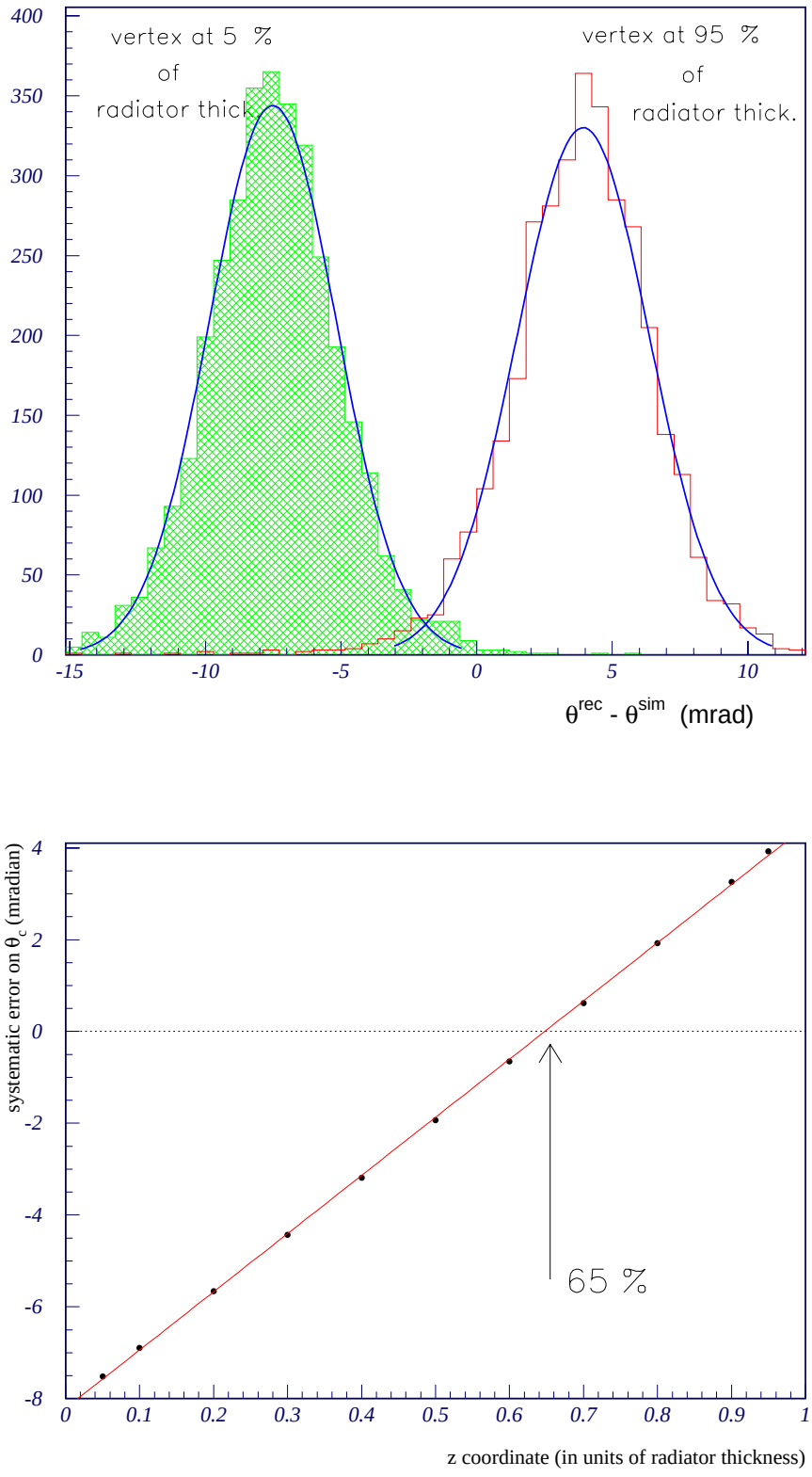

Figure 3.16: *Dependence of the systematic error (on reconstructed θ_c) on the emission point used for the pattern tracing. This result is for an Aerogel of 0.009 μm^4 cm^{-1} clarity*

.

Table 3.1: *The systematic error on the reconstruction of θ_c as a function of the chosen photon emission point in the case of a 3.0 cm thickness Aerogel radiator with a 0.009 $\mu m^4 cm^{-1}$ clarity coefficient. These values are better appreciated in fig. 3.17. Note that the statistical error is independent of this emission point.*

vertex z coord. (in % of radiator thichkness)	systematic error (mradian)	statistical error (mradian)
5	-7.51 ± 0.04	2.34 ± 0.03
10	-6.90 ± 0.04	2.35 ± 0.04
20	-5.66 ± 0.04	2.36 ± 0.04
30	-4.43 ± 0.04	2.35 ± 0.03
40	-3.19 ± 0.04	2.33 ± 0.03
50	-1.94 ± 0.04	2.32 ± 0.04
60	-0.66 ± 0.04	2.33 ± 0.03
70	0.62 ± 0.04	2.34 ± 0.04
80	1.92 ± 0.04	2.39 ± 0.04
90	3.26 ± 0.04	2.43 ± 0.04
95	3.93 ± 0.04	2.43 ± 0.04

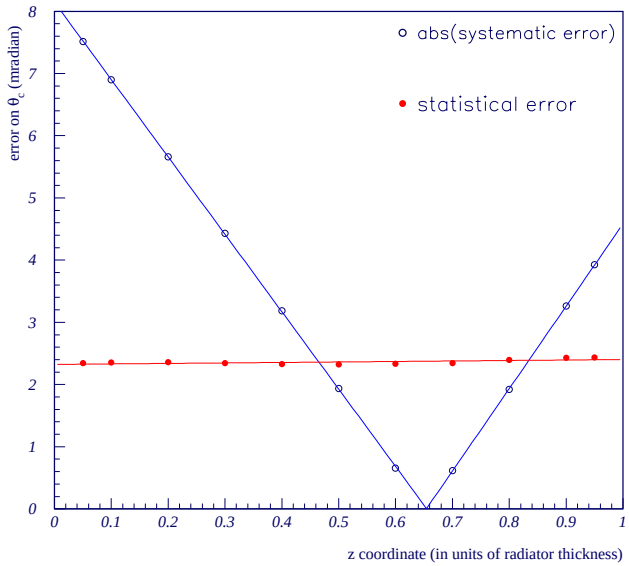

Figure 3.17: *Comparison between the dependence of the systematic error on $\theta_c{}^{rec}$ on the used Cherenkov vertex, and the nearly total independence of the statistical error. This result is for the Aerogel radiator.*

The question that now arises is: Why is not the middle point, z=50% of the radiator thickness, the optimal choice for the tracing and subsequent θ_c reconstruction?

In Aerogel, we know that due to the Rayleigh scattering, the radiator is not completely transparent to the photons. There is also an absorption component but much less important than the Rayleigh scattering. As the probability of the Rayleigh scattering increases with the radiator crossed length (remind expression 2.5), it is expectable that the photons emitted near of the radiator top are the most scattered and thus lost for the ring. This way, we expect the resulting distribution of the z origin coordinate for the detected photons being not uniform, but rather shifted to the lower part of the radiator. This can be easily checked in the simulation framework, where we can address to this coordinate variable for each detected photon. That's what is shown in the following histogram (fig.3.18).

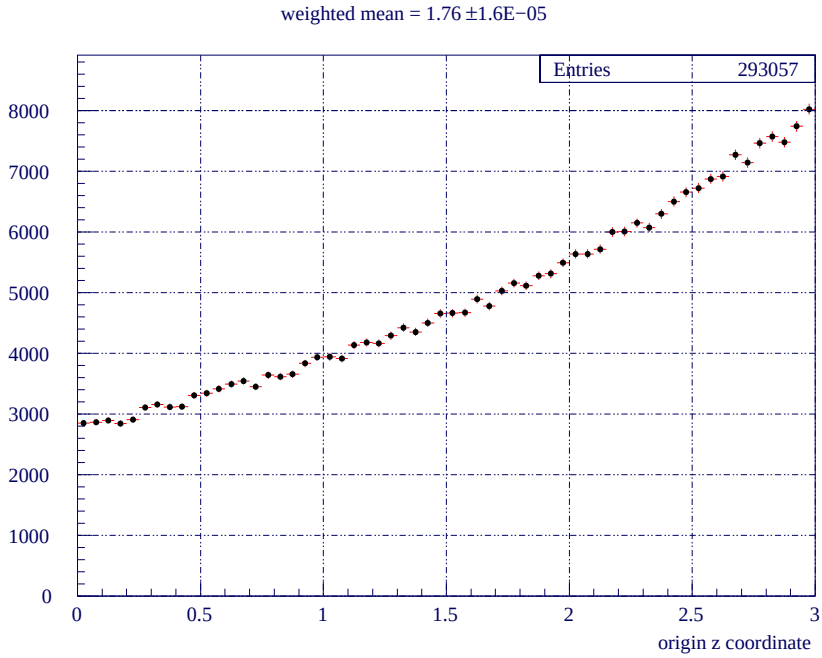

Figure 3.18: *Origin z coordinate distribution for the detected photons on the simulation (Aerogel radiator 3cm thickness, clarity* $= 0.0042\mu m^4\ cm^{-1}$*).*

The simulation points to an average value of the z origin coordinate about 59% of the radiator thickness. Comparing this value so obtained with the value that minimizes the systematic error, one can say that the vertex effect seems reasonably well understood.

Next, Let us see how it goes for a NaF radiator. The same tunning study is next reproduced giving the results of the following equivalent figures and tables.

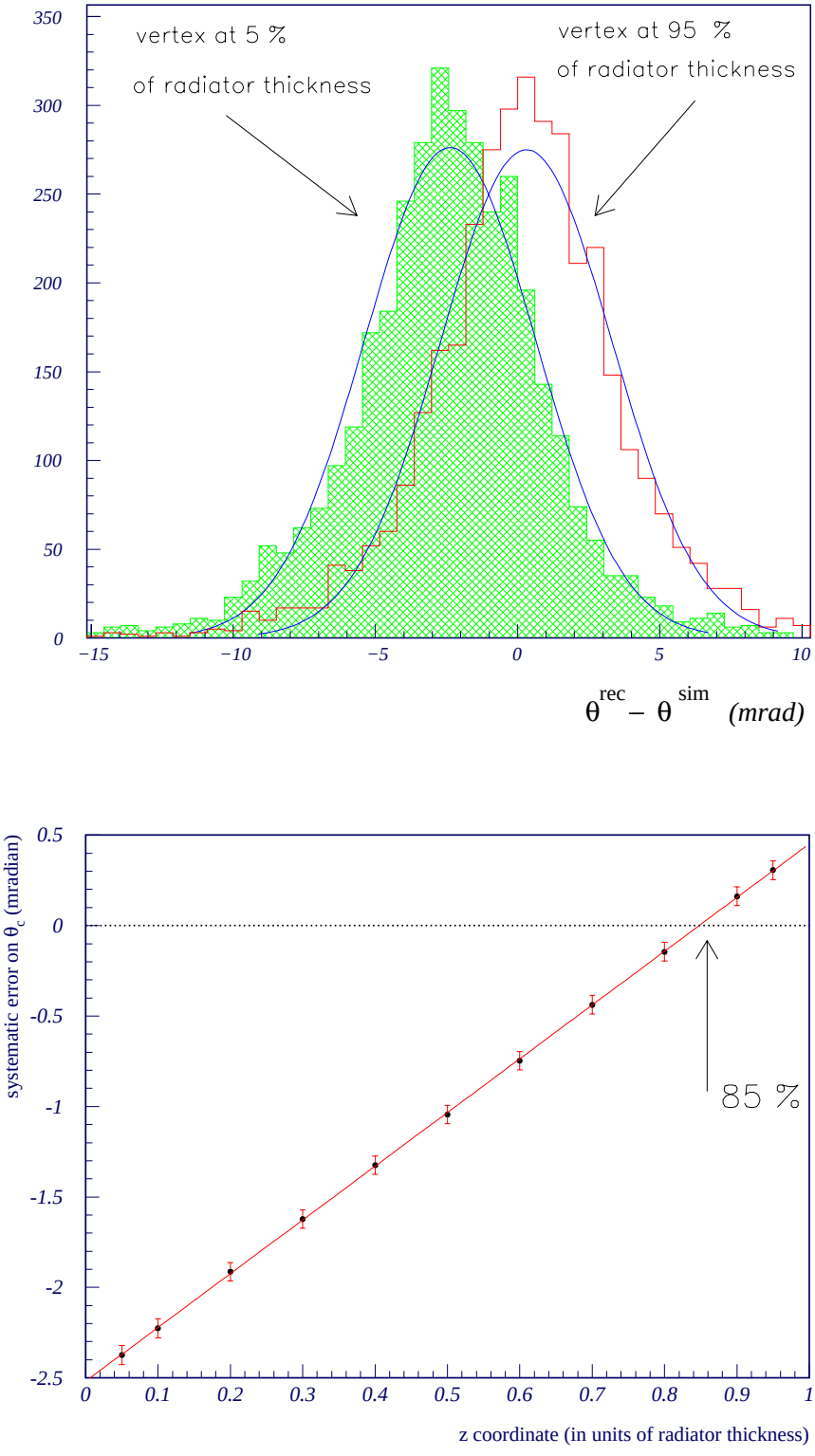

Figure 3.19: *Dependence of the systematic error (on the reconstructed θ_c) on the used emission point (NaF radiator).*

Table 3.2: *The systematic error on the reconstruction of θ_c as a function of the chosen photon emission point in the case of a 0.5cm thickness NaF radiator. These values are better appreciated in fig. 3.20. Note that the statistical error is independent of this emission point.*

vertex z coord. (in % of radiator thichkness)	systematic error (mradian)	statistical error (mradian)
5	-2.37 ± 0.05	3.02 ± 0.05
10	-2.23 ± 0.05	2.97 ± 0.05
20	-1.91 ± 0.05	2.91 ± 0.05
30	-1.62 ± 0.05	2.92 ± 0.05
40	-1.32 ± 0.05	2.90 ± 0.05
50	-1.04 ± 0.05	2.93 ± 0.05
60	-0.75 ± 0.05	2.93 ± 0.05
70	-0.44 ± 0.05	2.98 ± 0.05
80	-0.14 ± 0.05	2.98 ± 0.05
90	0.16 ± 0.05	3.00 ± 0.05
95	0.31 ± 0.05	3.02 ± 0.05

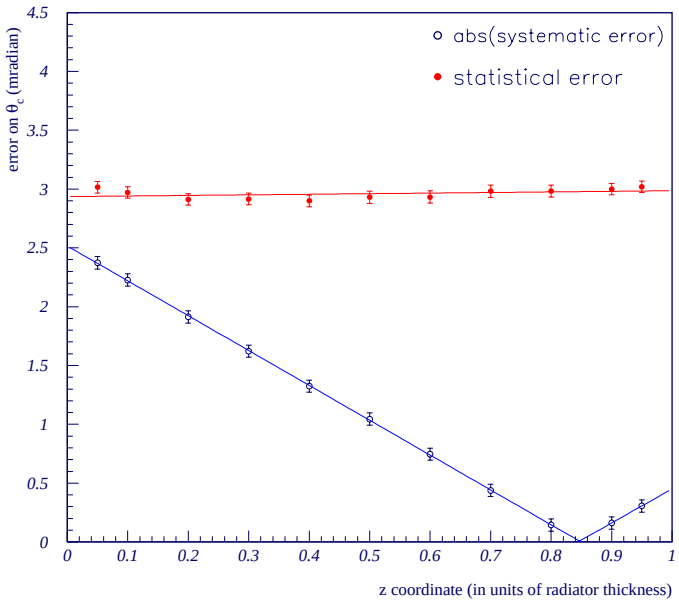

Figure 3.20: *Comparison of the sensitivity of the systematic error absolute value with the insensitivity of the statistical error on the used emission point.*

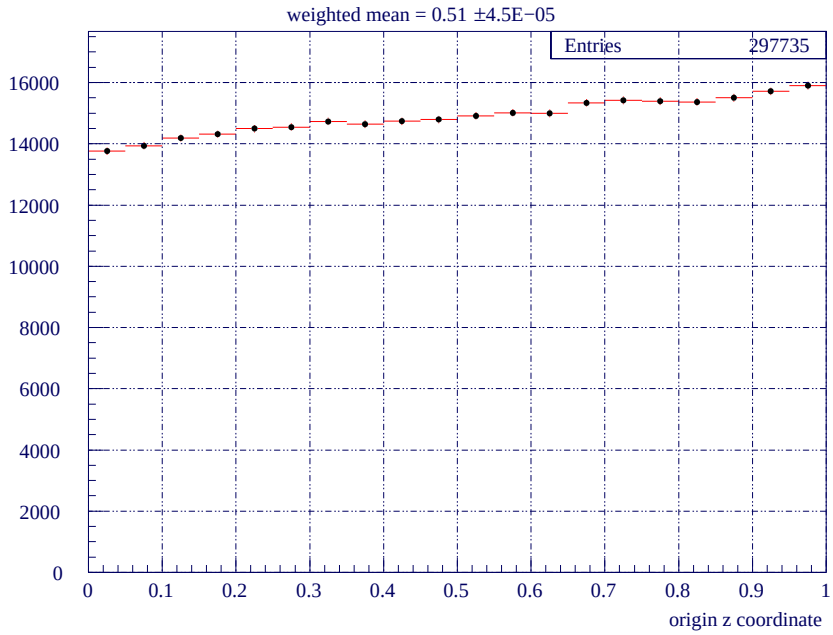

Figure 3.21: *Origin z coordinate distribution for the detected photons on the simulation (NaF radiator 1cm thickness).*

The found optimal tunning value of 85% in the NaF case (fig. 3.19) is a result somehow surprising because this material is very transparent and then it can't be understood on the basis of an absorption effect, like it was in the Aerogel case.

On the contrary, the histogram with the photon's origin z coordinates obtained in the simulation (fig 3.21) attests the idea of using a emission point at 51% of the radiator thickness; say the middle.

The reason for our lower optimal emission point may have to do with the larger chromaticity. When tracing the photons downwards, the reconstruction makes use of this value 1.334 for the refraction in the exit of the radiator. By these results, this refractive index nominal value seems to be too high, giving thus rise to lower Cherenkov angles in the reconstruction. And so this emission point pushed to 85% may appear as a correction to the previous effect.

In fact, the same explanation may account for the 5% discrepancy between the average given by simulation and the tunning optimal coordinate in the case of Aerogel.

3.3 Bayes Theorem and the Maximum Likelihood method

This section is intended for the reader not so familiar with the likelihood methodology. The maximum likelihood parameter estimation follows directly from the Bayes theorem that states the following relation for the conditional probabilities for the dependent events A and B,

$$P(A|B) = \frac{P(B|A)\ P(A)}{P(B)}$$

where $P(A|B)$ is read as "probability of A given the knowledge of B". In the *Bayesian* interpretation, one can apply this relation to the case where one of the random variabales is not a directly measurable quantity but rather a testable hypothesis for the value of an unknown parameter that we pretend to estimate. To illustrate this theorem aplication in a more precise way, let us consider the task of estimating the Cherenkov angle θ_c. This parameter gives rise to a given collection of detected hits and corresponding residuals X. And so we write down:

$$p(\theta_c|X) = \frac{p(X|\theta_c)\ p(\theta_c)}{P(X)}, \tag{3.11}$$

where the meaning of each term is the following:

- the p.d.f. $p(\theta_c)$ represents an *a priori degree of belief* for the occurence of a particular value of the parameter θ_c (i.e., without any knowledge of the values taken by the random variable X).
- $p(\theta_c|X)$ is interpreted as the *a posteriori* p.d.f. for θ_c .
- $p(X|\theta_c)$ is the p.d.f. for the variable X, given the knowledge of the value taken by the parameter θ_c (this is commonly called the likelihood).
- $P(X)$ is the total probability to get the value X, regardless the value of θ_c. $\left(P(X) = \int p(X|\theta'_c)\ p(\theta'_c)\ d\theta'_c\ \right)$

Equation 3.11 is so the probabilistic translation of the rather intuitive idea that our degree of belief for the value of θ_c must change from the *a priori* situation to the *a posteriori* situation, when more information is available (by the knowledge of the value(s) for X). In the usual and realistic situations one doesn't know $P(X)$. And

the a priori probability $P(\theta_c)$ is a rather subjective matter. However if one decides that it can be represented by a uniform distribution, being this way a constant value, one can write eq. 3.11 in a weaker but still useful form:

$$P(\theta_c|X) \propto P(X|\theta_c) \tag{3.12}$$

The equation 3.12 is useful because we may do not know how to compute $P(\theta_c|X)$ but we if we know how to compute $P(X|\theta_c)$, this relation can be used to estimate the best parameter for the observations X. Because the values of X depend on the parameter θ_c, we usually think of $P(X|\theta_c)$ as a function of θ_c only, $\mathcal{L}(\theta_c)$. In this Bayesian framework, the posterior p.d.f. $P(\theta_c|X)$ represents all the knowledge we can have about the parameter θ_c , and in view of eq. 3.12, a good estimation is given by the value $\widehat{\theta_c}$ that maximizes the likelihood function $\mathcal{L}(\theta_c)$. This is the basis of the maximum likelihood parameter estimation technique. For a more detailed and formal discussion, consult the reference [20] (sections 1.2 and 6.13).

Chapter 4

Application to the simulated Flight Setup

The results presented in this section have been collected in the framework of the standalone RICH simulation referred in chapter 2. The most fundamental parameters here used were:

- Aerogel refractive index: 1.03 (clarity: 0.009 $\mu m^4/cm$)
- radiator thickness: 3 cm
- expansion volume height: 45.8 cm
- light guide size: 34 mm ($\Rightarrow$ pixel size : 8.5 mm)
- light guide pitch: 37 mm
- A polyester foil of 0.75mm thickness has been included[1]

For the NaF radiator results, the radiator thickness is only 5 mm. The remaining parameters are kept unchanged.

Before comparing the results for these two different radiators, we note that the NaF radiator presents clearly a different residuals distribution from the one of Aerogel. This is illustrated in figure 4.1. Figure 4.2 shows the Likelihood p.d.f. in the case of NaF. The differences from the aerogel case (see fig 3.11) are the smaller

[1]This is a more absorbing plastic than the one that will be used in the real detector, so the statistics of the hits may be slightly underestimated in these results.

domain (D) that is basically half of the aerogel one and the larger Gaussian width that is around the double.

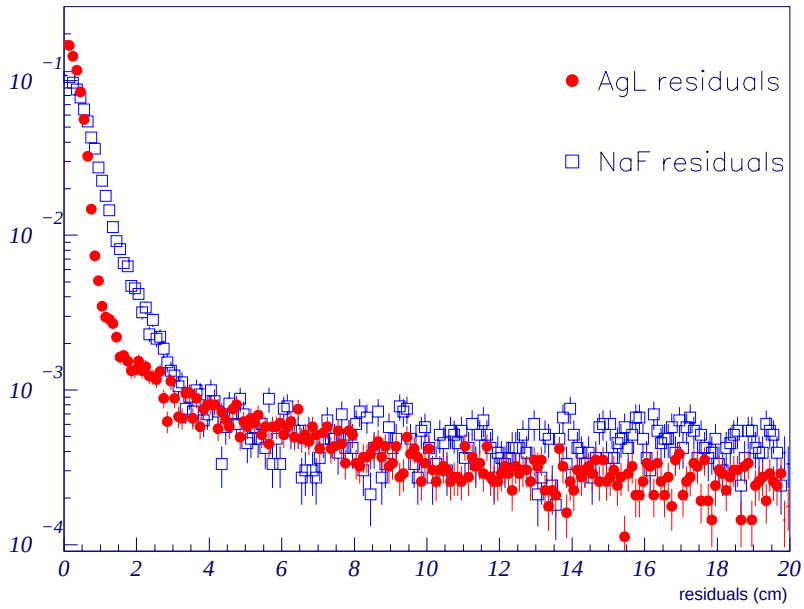

Figure 4.1: *Distributions of residuals for Aerogel and NaF, both normalized to the unit.*

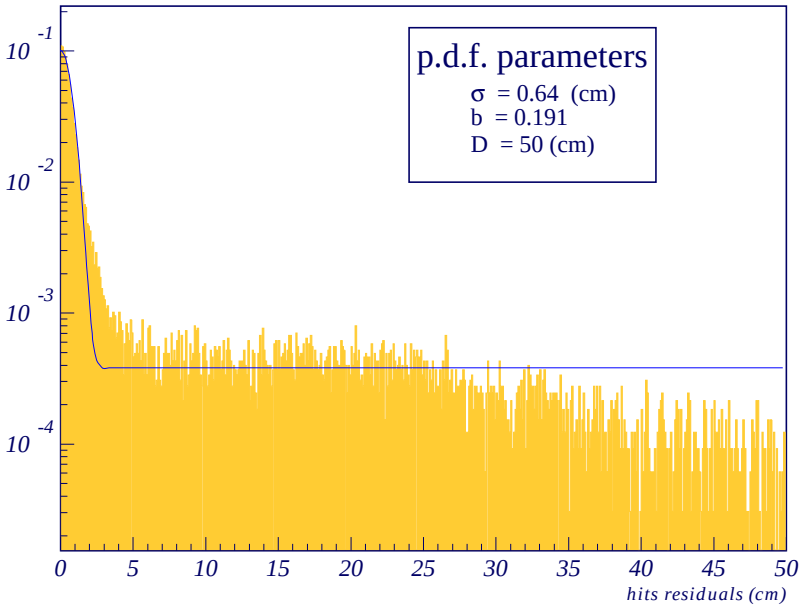

Figure 4.2: *Residuals distribution for NaF with the adopted Likelihood p.d.f. superimposed.*

Defining the number of degrees of freedom of the pattern fit as the number of hits on the reconstructed pattern[2] minus one (because the reconstruction has only one free parameter) one could think of accept reconstructions with at least 2 hits on the pattern. However, due to the background level introduced by the reconstructions with 2 hits, we restrict the acceptation criterion to at least *3 hits reconstructions*.

Figure 4.3 shows the number of hits in question, for the reconstructed heliums of 10 GeV/c/nuc starting from 10000 events in all AMS acceptance. This set of events is the statistical universe analyzed in the rest of the chapter for all the following plots.

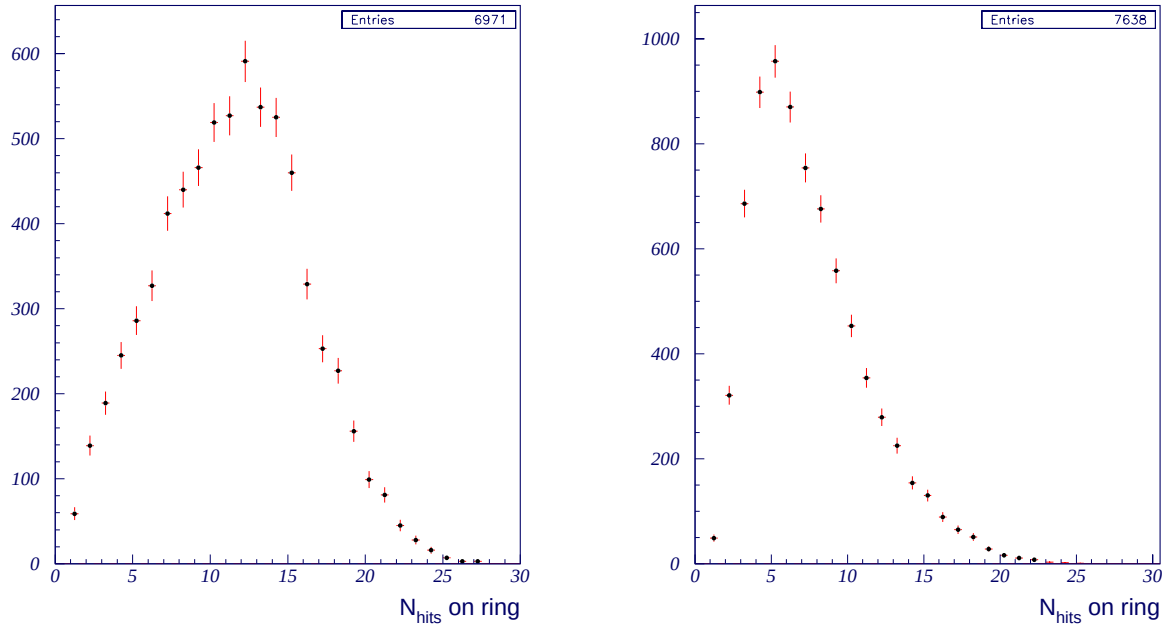

Figure 4.3: *Number of hits on reconstructed pattern (counting criterion: hits with residuals* $< 4\sigma_{\text{Likelihood p.d.f.}}$*)*

With such a basic criterion, figure 4.4 shows the corresponding results for the reconstruction of the Cherenkov angle θ_c for Aerogel and NaF radiators. The curves on top of the histograms are the respective Gaussian fits, which are used all trough this thesis to estimate θ_c^{rec} and β^{rec} resolutions. For an easier appreciation, figure 4.5 shows the same reconstruction results in the variable $\theta_c^{\text{rec}} - \theta_c^{\text{sim}}$. The achieved resolutions of about 2.3 and 3.4 *mradian* must not be directly compared as characterizing

[2]These hits are counted as the hits inside a distance window from the reconstructed pattern, such that they matter for the fit. This counting distance is naturally defined by 4 sigmas of the residuals Gaussian signal distribution.

the radiators, because of the different statistics entering the fits in the Aerogel and NaF cases.

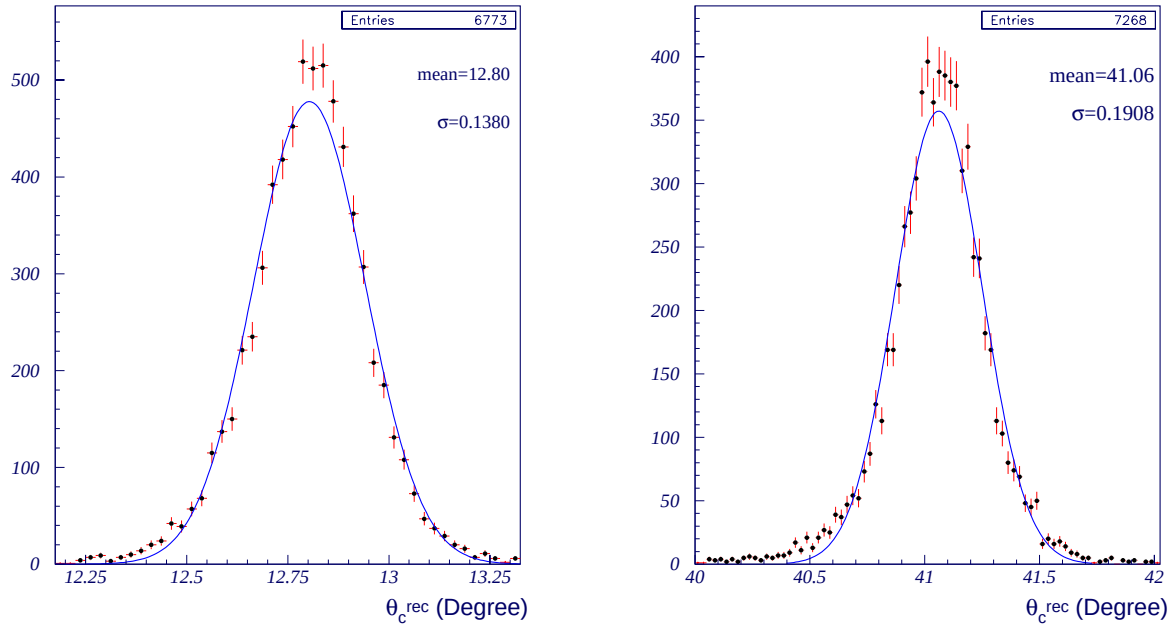

Figure 4.4: *Reconstructed θ_c histograms – Heliums 10 GeV/c/nuc in AgL* (Left) *and NaF* (Right).

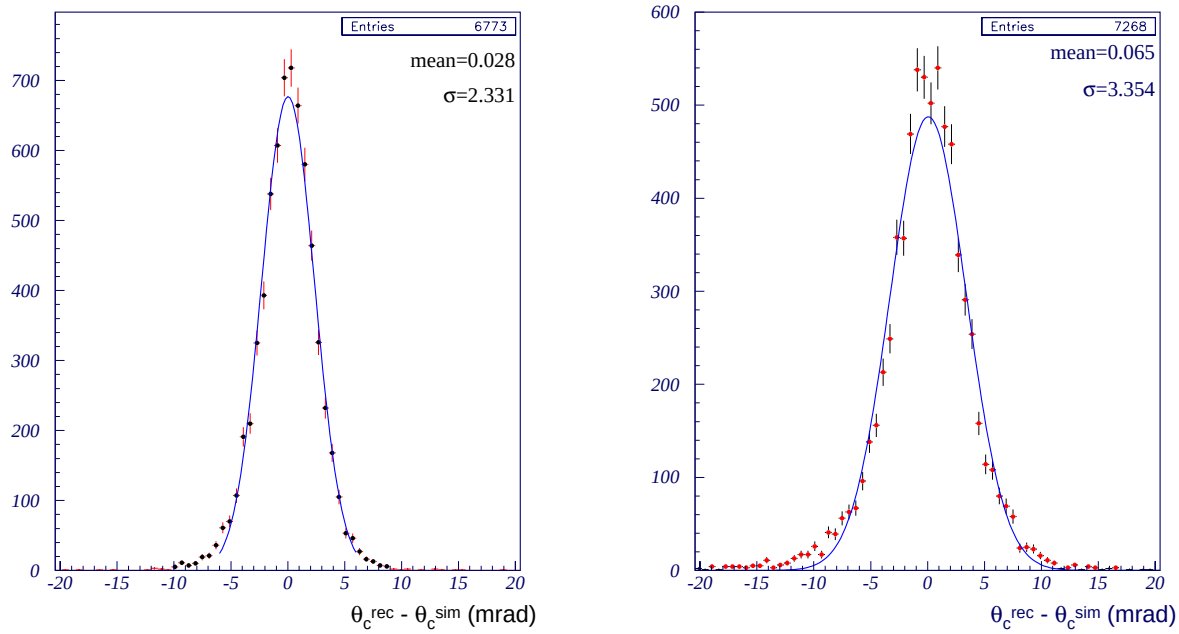

Figure 4.5: *Histograms of $(\theta_c^{rec} - \theta_c^{sim})$ for Heliums 10 GeV/c/nuc in AgL* (Left) *and NaF* (Right). *The scale is in 10^{-3} radian.*

The histograms that one can compare as giving the intrinsic resolution for the reconstructed Cherenkov angle of each radiator are the ones of figure 4.6. These last present an estimation of the *single hit* resolution. This estimator consists simply in multiplying the factor $\sqrt{N_{hits}}$ to the total resolution variable of figure 4.5 ($\theta_c^{\rm rec} - \theta_c^{\rm sim}$), in order to deconvolute the total resolution from the number of hits (remind eq. 2.9). As one can see, the single hit resolutions are not so different.

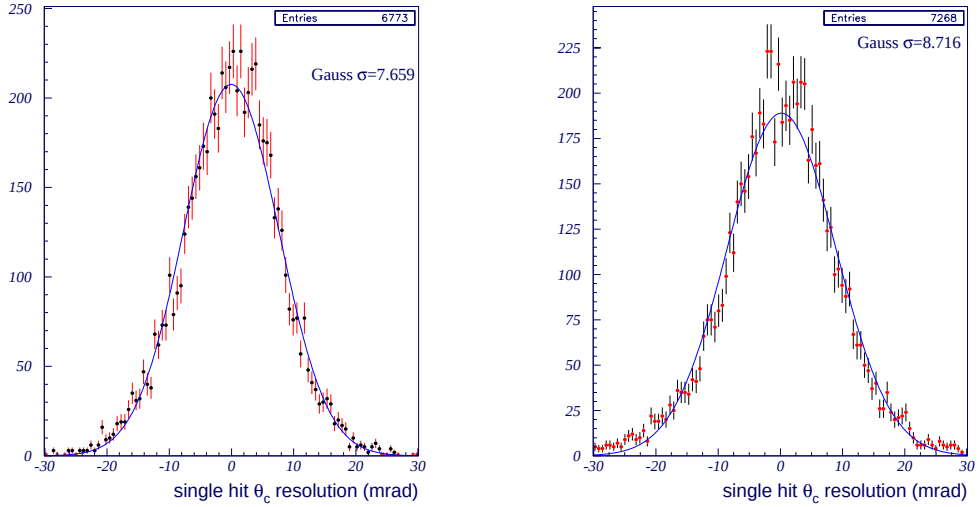

Figure 4.6: Single hit θ_c *resolutions for Heliums 10 GeV/c/nuc in AgL* (Left) *and NaF* (Right). *The unit of the scale is* 10^{-3} *radian.*

The big difference between the Aerogel and NaF radiators comes when one compares the single hit velocity resolutions presented in the histograms of figure 4.7 and this is so because of the scaling law of eq. (2.9) (page 36).

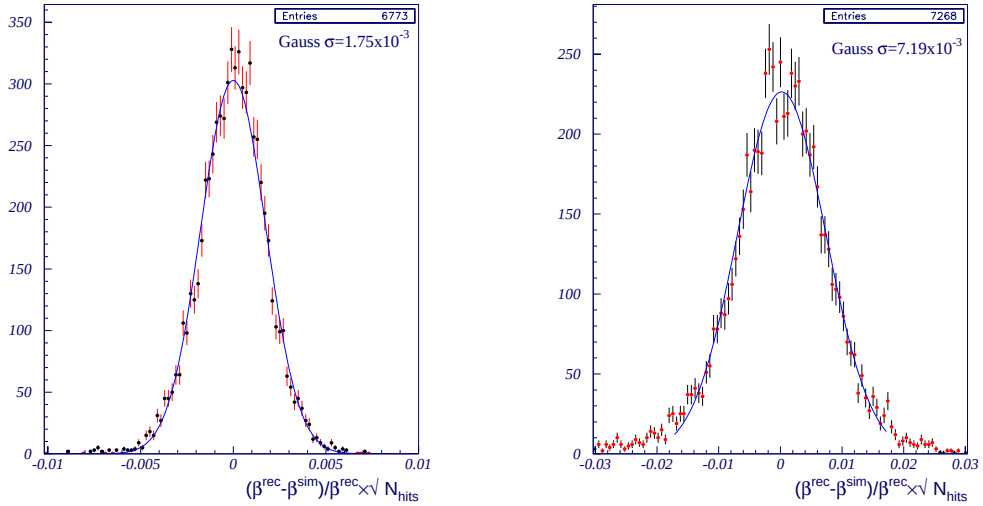

Figure 4.7: Single hit β *relative resolutions for Heliums 10 GeV/c/nuc in AgL* (Left) *and NaF* (Right).

To give an idea of the algorithm performance, we show in figure 4.8 the evolution of the mean value of the Cherenkov reconstructed angle with the particle velocity in units of momentum per nucleon, again for both radiators. This result corresponds for each momentum to a large statistics input of 10000 heliums in all AMS acceptance.

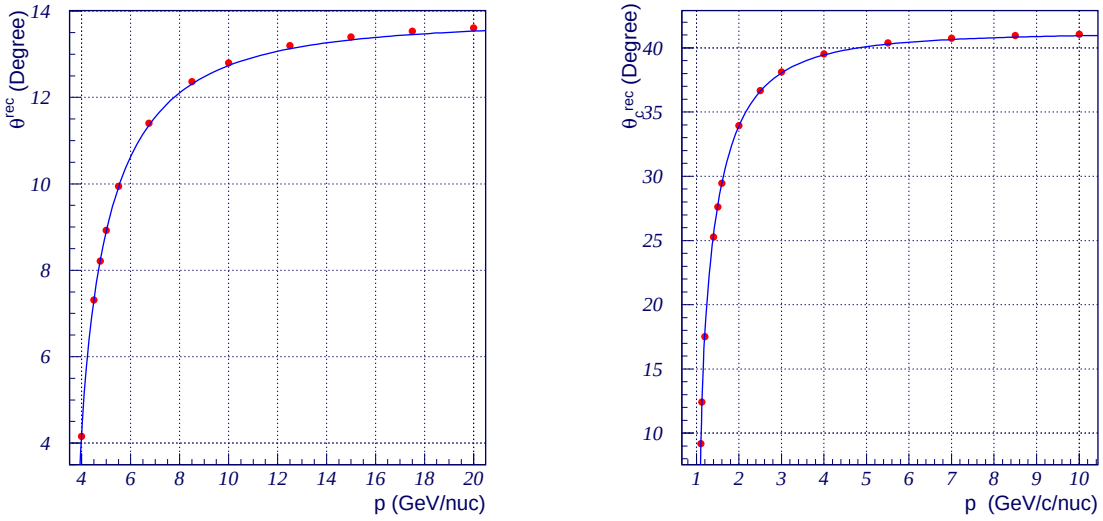

Figure 4.8: *Reconstructed θ_c as function of momentum per nucleon. The reconstruction of θ_c follows the Cherenkov scaling relation (depicted here by the line).* Left: *result for AgL .* Right: *result for NaF. The error bar is too small to be seen on this scale.*

In this wide vertical range, the agreement is most satisfactory but it is also interesting to note that we have a very small varying systematic error that is shown in the plots of figure 4.9. In these plots the variable in the y axis is the difference between the mean Cherenkov reconstructed angle of last plots and the expected Cherenkov angle.

This curious and surprising systematic error evolving with the velocity can however find an explanation in the chromaticity domain. As we have seen in section 2.3.1, the chromaticity gives rise to a asymmetric Cherenkov angle spectrum whose mean value is not coincident with the peak. The scaling of the chromaticity described by eq. (2.6) makes these 2 values come closer as one goes from lower to higher particle velocities. The fact that the shape of the curve can be well fitted by the model of eq. (2.6) is certainly not incidental.

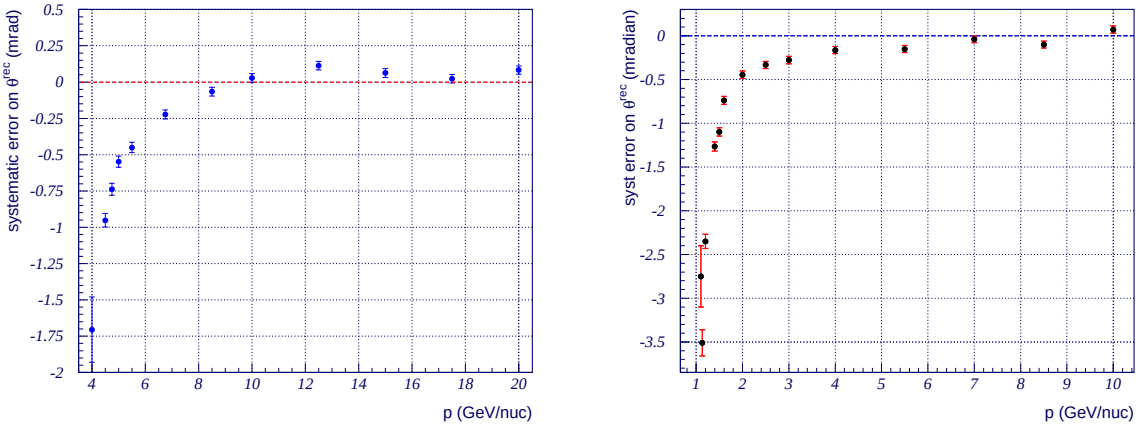

Figure 4.9: *Systematic error on $\theta_c{}^{rec}$ versus momentum per nucleon of the particle.* Left Plot: *Aerogel radiator result.* Right Plot: *NaF result.*

At last, we show the corresponding evolutions of the statistical error in the plots of figure 4.10. Note that the asymptotic values for the single hit θ_c resolution that we obtain here – around $7.5\,mrad$ – are slightly worst than the values estimated for the vertical incidence case – these were about 5.5 and $6.5\,mrad$ for the Aerogel and NaF respectively. This is what was generally discussed in the ending section of chapter 2.

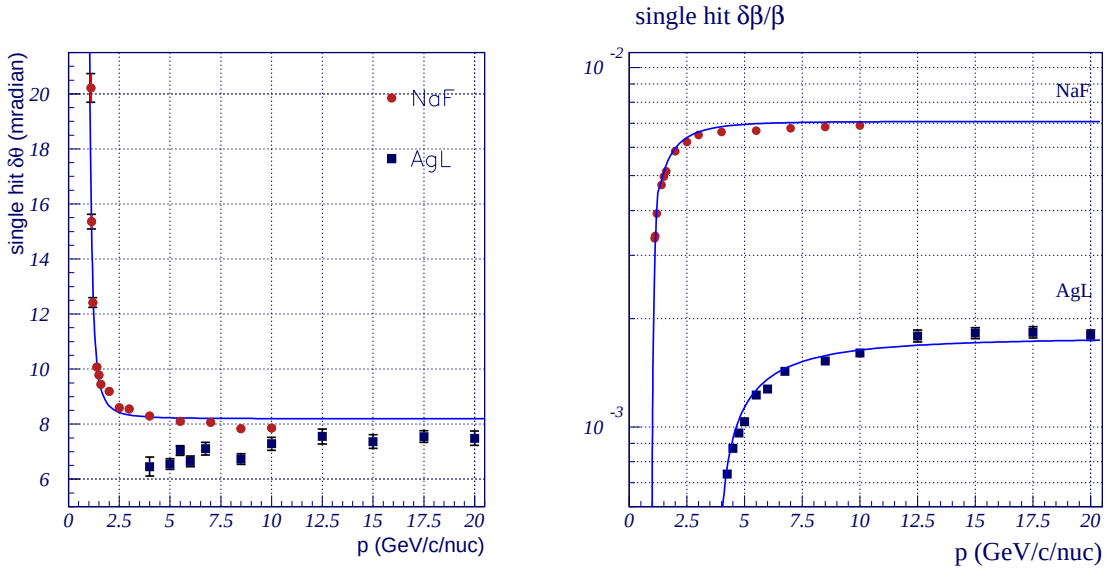

Figure 4.10: *Comparison of the single-hit θ_c resolutions and relative resolution on β for the two radiators in analysis.*

On the velocity single hit resolutions domain, the agreement of the obtained values – $\lesssim 0.2\%$ and 0.7% for the aerogel and NaF configurations respectively – with the expected values of chapter 2 is even better.

Chapter 5

Analysis of data collected with the RICH prototype

5.1 The RICH Prototype setup

In order to test the real components of the final detector, a prototype has been developed and assembled at ISN (Grenoble-France). This prototype has a much simpler mechanical design than the final flight setup. It essentially consists of a photomultipliers readout matrix - representing about one sixth of the final detector version (see fig. 5.1)- plus a radiator.

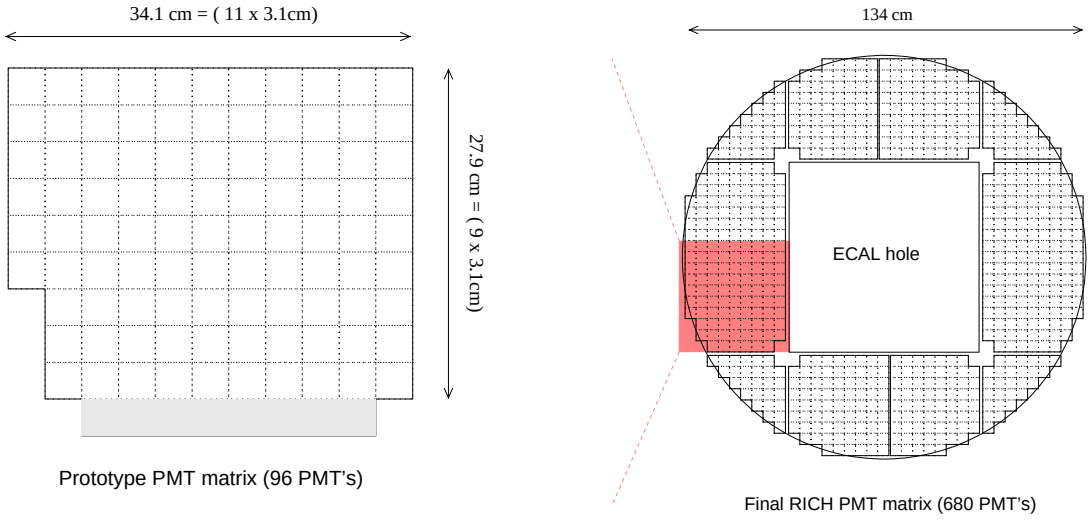

Figure 5.1: *Prototype and Flight setup PMT matrices. The Prototype PMT matrix consists approximately of one module of the final Setup. The shadowed row of the Prototype matrix doesn't contain PMT's.*

The PMT's are the Hamamatsu R7600-M16 (4×4 pixels); the same that will be used on the final detector. From the point of view of who is basically interested in using the detector to reconstruct Cherenkov rings, the main differences compared to the final setup are the absence of a mirror, the pitch and size of the light guides and generally speaking the lower dimensions of the whole set.

In the final setup, the dimension of the light guide set - 4×4 pixels - is $34mm$ and there is a pitch of $37mm$, leaving so a dead gap of 3mm between successive light guides sets. In the prototype setup, the pitch equals the light guide size, which is a bit smaller: $31mm$. The radiator has basically the dimensions of 3×3 tiles, giving a square of about $34.5 \times 34.5\, cm^2$. The PMT matrix has 11 per 9 PMT's units (4×4 pixels), giving an overall rectangle of about 34 cm per 28 cm.

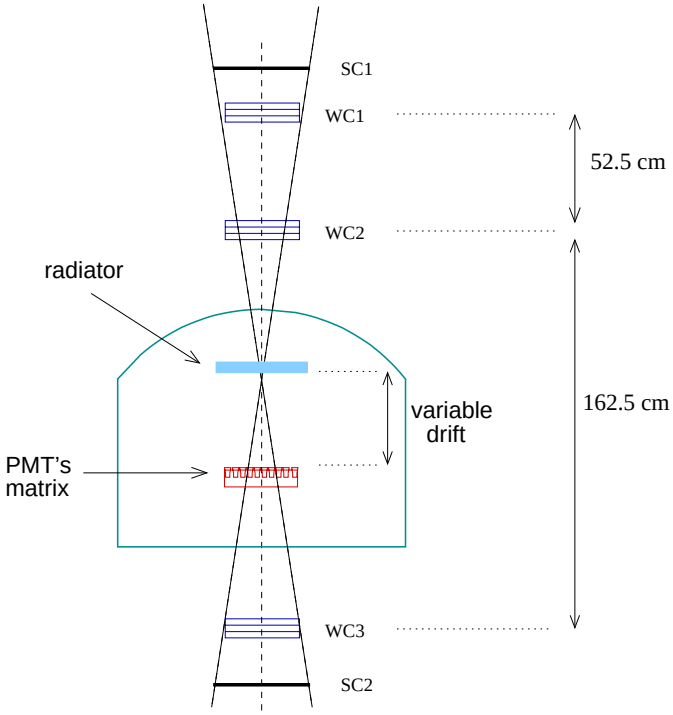

Figure 5.2: *Schema of the prototype setup with some dimensions. WC1,WC2 and WC3 depict the 3 wire chambers. SC1 and SC2 are the 2 scintillators used to trigger the acquisition after the muon passage. The expansion ring height (or drift) was varied along the runs. The values are given in table 5.1.*

Different radiator materials and thicknesses were used along the several runs. The expansion volume height (or drift height) has also been changed according to the radiator refractive index, taking the values 32 and 41 cm in whole numbers, and also 7.5 cm for a NaF run. About the radiator assembly, we have to signal that a polyester foil, of approximately 0.75mm thickness and a refractive index of 1.56, is

put under the aerogel tiles for mechanical support reasons. The effect of its presence has been tested by performing some runs with and some without it.
In order to keep the RICH detector isolated from the environment light, its main components {radiator+pmt readout matrix} are closed into a large "kitchen pot" kind of container.
The tracking system used was composed by a set of 3 wire chambers disposed under and above the RICH detector. The basic setup just described is schematized in the previous figure (fig. 5.2).

data summary

The data here analyzed have been taken by simply exposing the Prototype to the cosmic muons, with a trigger rate of 0.5 Hz, from end July to beginning September 2002 at the ISN laboratory. The main characteristics of these runs are summarized in table 5.1. Two aerogel refractive indexes were basically tested (n=1.03 and n=1.05). A different sample for each one of these indexes has also been studied in the runs 31 to 48. A run with a NaF tile has also been made. Whenever possible, runs with same characteristics had been added up to increase the statistics (case of runs 12 and 27, 24 and 25, 15 and 16 and the *Multi-radiator* runs - 31 to 48).

RUN	Radiator		Drift (cm)	Foil	Nb trigg evts
	index	thick. (cm)			
31, 32, 46, 48 [(a)]	1.02	3	41.65	No	
12, 27	1.03	3	41.65	Yes	124 477
20		3	41.65	No	59 806
31, 32, 46, 48 [(a)]		2	41.65	No	
22	1.05	3	32.65	Yes	58 419
24, 25		3	32.65	No	58 728
15, 16		2	32.65	No	61 131
10		2	41.65	Yes	52 495
31, 32, 46, 48 [(a)]		2	41.65	No	
29	NaF	0.5	7.5	No	108 767

Table 5.1: *Summary of the cosmic runs processed for this thesis. The runs indicated with [(a)] were taken with 3 different aerogel tiles (n=1.02,1.03 and 1.05).*

5.2 PMT signal and Noisy channels

When a photon hits the photocatode of a photomultiplier, an electron is expected to be emitted by photoelectric effect. For the PMT's used in the AMS RICH, this efficiency follows the probability curve of fig. 2.6. Then the photoelectron is amplified or multiplied through a cascade mechanism up to the situation of having collected a macroscopic electric charge. This charge corresponds typically to that of about $10^7 - 10^8$ electrons. This charge is collected to give an electric current which is then integrated in time and converted into a digital (discrete) signal that is usually called the ADC signal. This signal is so a measure of the intensity of light collected by the PMT (see ref. [21] for further details).

Indeed, the PMT electronics gives rise to a signal even in the absence of stimulating light. This signal - called pedestal - must be known and subtracted to get the physical signal, since it is always present. To access it, the followed routine is to turn on the acquisition without any light and registry the PMT signals. These are the pedestal runs, performed periodically in between the cosmic runs and used to do the pedestal calibration of the apparatus. As one can see by figure 5.3, where the result of such a pedestal run is shown for 16 channels of one PMT, this pedestal signal is different for every one the 1536 channels (96 PMT's $\times$ 16 pixels) of the Prototype. By an adequate fit to these distributions, a table of 1536×2 values (pedestal peak plus width) is then built and used to calibrate each channel reading of a real data run. The sigma is less varied than the peak and has an average value of 3 to 4 ADC counts. The peak is subtracted to the raw ADC signal, and ADC corrected readings lower than 4 sigmas of the respective pedestal are rejected.

A calibration is also needed to convert each ADC corrected signal in a number of photoelectrons[1]. These calibrations come from runs where the PMT's are illuminated with a light source so weak that we are sure no more than one photon arrives at each photocathode at a time. These runs provide the *single-photoelectron* spectrum, again for each channel. This photoelectron spectrum is again varied with an average value of 50 to 60 ADC counts. After these calibrations become available, one can start to study these PMT signals - the raw signal of the RICH detector.

[1] As only the corrected ADC has physical meaning, we short the designation to ADC signal from now on, meaning by this the signal with the pedestal subtraction already performed.

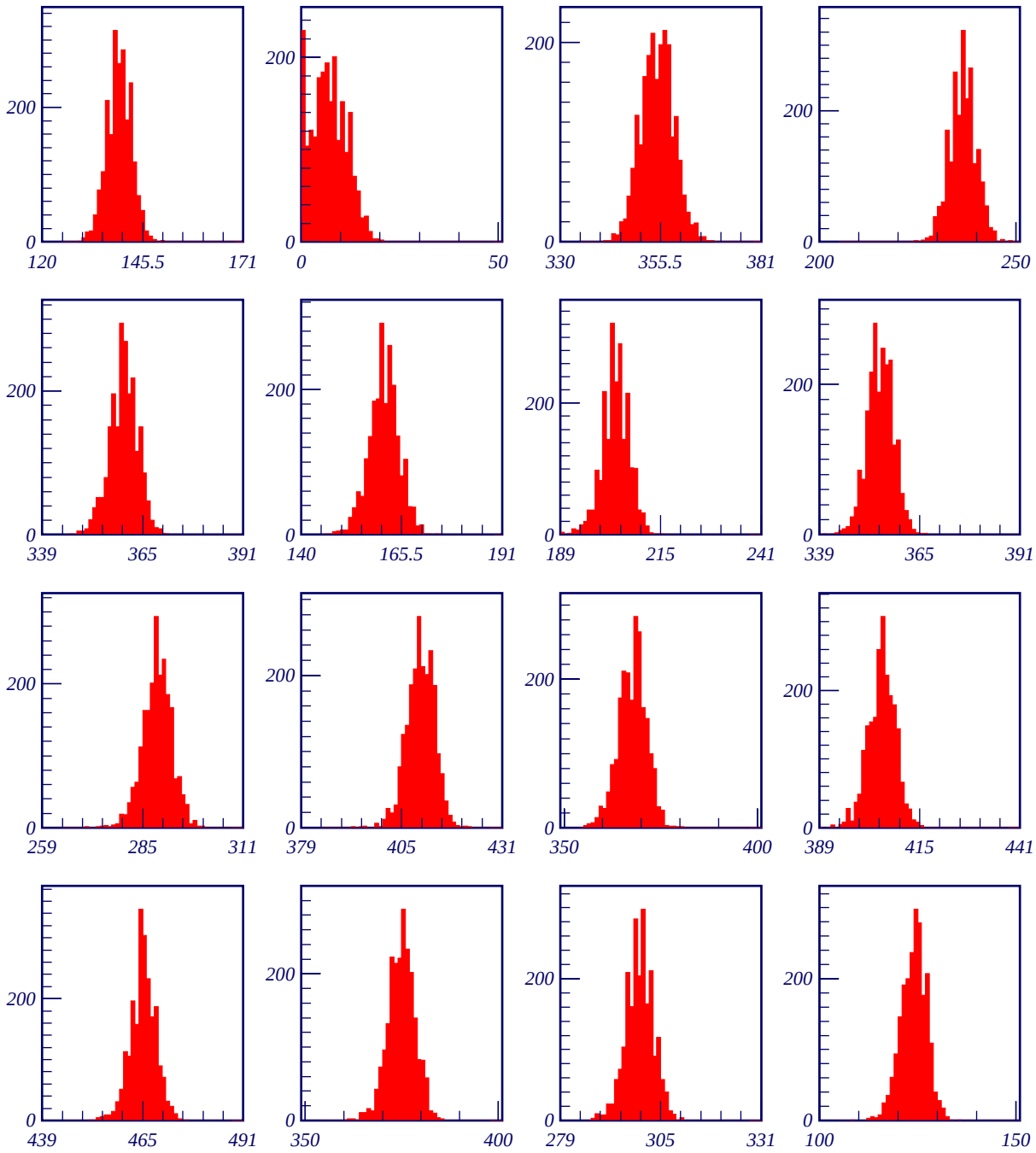

Figure 5.3: *pedestal ADC signal for 16 channels of PMT # 1 (pedestals for run 11 in high gain mode). Despite the shown covered ranges being different from each other, their widths is 50 ADC for all the 16 channels.*

The first thing to do is to remove eventual spurious readings. It can happen, for some PMT malfunctioning, that a given channel fires anomalously. A simple way to check this consists on counting how many times each one of the 1536 PMT channels triggers during a sufficient long period of time and build a map firing frequency for

all the pixel channels. Such a map is given in fig. 5.4. This clearly shows that the occupancy is not uniform but has a rather radial decreasing dependence. This is a reflexion of the total acceptance of the experiment. However, our concern is here about the anomalous high fluctuations on top of this global occupancy distribution, because these reveal anomalous trigger rates for the respective electronic channels.

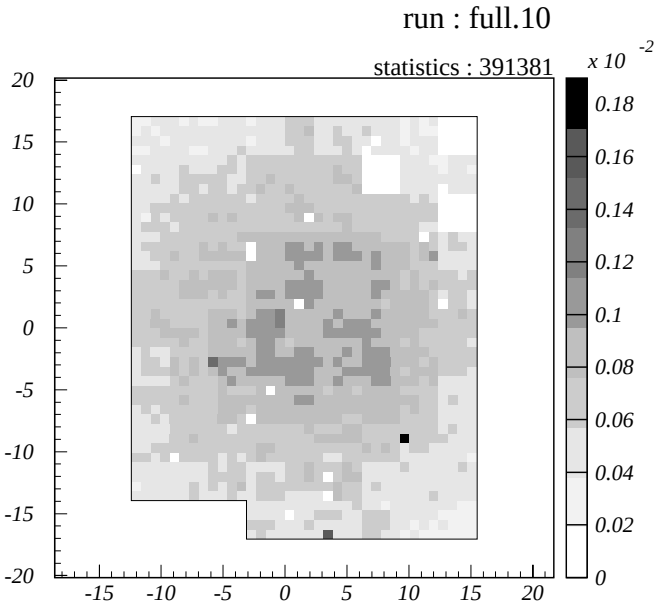

Figure 5.4: *Spatial analysis for the pixel PMT channel occupancy (or firing) frequency. For an easier comparison between runs with different statistics, the occupancy is normalized by dividing the accumulated number of hits for each pixel by the total number of hits of the whole run. This normalized occupancy gives an idea of the spatial probability distribution for a hit among the PMT matrix.*

The run used to build this occupancy map is the cosmic muons collecting run itself. The advantage in doing so, is that we are checking for the functioning of our electronics during the operating time of interest and not another time where some unknown conditioning variables could take on different values.

In figure 5.5, the same information of fig. 5.4 is provided, except for the spatial location of the 1490 fired channels during one of the data runs here analyzed (run 10). It gives however a clearer view of what might be considered an anomalous frequency. By a look to it, one gets the impression that the three higher frequencies are well above the normal end point of the main distribution. Simulation reproduces well the main distribution without any tails.

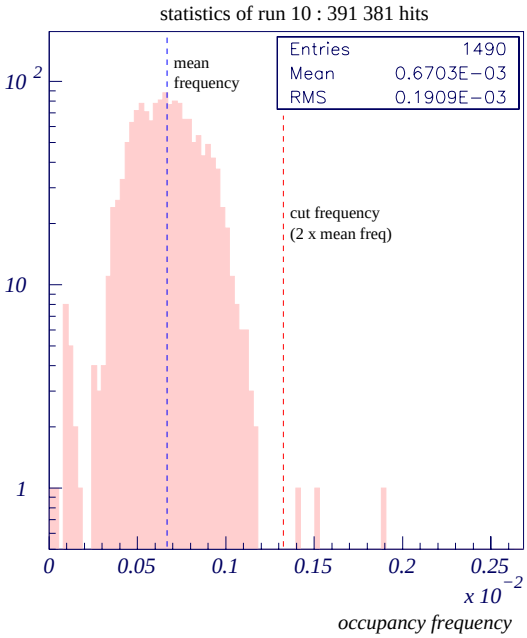

Figure 5.5: *PMT channel occupancy frequency analysis. This histogram plots the normalized occupancies for all fired pixels (1490) of run 10. Note that the mean of this histogram would correspond to a spatial uniform occupation of all the channels of the PMT matrix. There are 3 channels above cut frequency.*

It has so been decided to look the occupancy frequencies higher than twice the mean value as suspect and to reject them.

Table 5.2 collects these anomalous channels. Despite some more frequent channels (stressed in bold in the table), these change along the data runs, so it is important to perform this analysis for each data run before anything else.

run	10	12	15	16	20	22	24	25	27	29	31	32	46	48
anomalous pixels list	**306**, 688, **1154**	**1154**	1088, **1154**, 1157	**1154**, 1167	**306**, 814	**306**	**306**, 1312	**306**	261, **306**, 450, 453, 690, 824, 1014	(83 channels)	628, 1146, **1154**, 1163	628	98, **306**, 456, 480, 688, 880, 1280, 1319, 1447, 1508	**306**

Table 5.2: *Summary of the rejected channels during the cosmic runs. The pixel channel addresses go from 0 to 1535.*

5.3 Alignment of the prototype elements

We are now going to consider another feature that was not present in the simulation. The mechanical assembling of the different components of the RICH prototype may comprehend slight misalignments between each other. These possible misalignments, if not corrected, would damage the resolution of the Cherenkov reconstructed angle, because the reconstruction depends on the hits location relative to the particle track. So, the components that we must check out for these eventual misalignments, and then correct, are the tracking wire chambers and the PMT readout matrix. The radiator precise location doesn't play any role at this level.

5.3.1 Wire chambers inter-alignment

The x and y coordinates of the three points defining the muon track across the wire chambers are measured in two somehow independent systems. There are three wire chambers to measure the x coordinate at three fixed vertical levels, and another three juxtaposed chambers to measure the y coordinate. It is then convenient to decompose our 3-D track $\{x_i, y_i, z_i\}$ into two projected tracks: $\{x_i, z_i\}$ and $\{y_i, z_i\},\ i = 1, 2, 3$.

The misalignment we are searching for is simply a misalignment of the $x(y)$ axis origins of the different wire chambers between each other. The wire chambers are assumed to be parallel and perpendicular to the local vertical. The reference direction that we'll use to detect and correct for the misalignments is the track information itself. We start by fitting a straight line to the wire chambers hits coordinates, defined by the two parametric equations:

$$\begin{aligned} x &= a + bz \\ y &= c + dz\ . \end{aligned}$$

If the wire chambers are well aligned, the track fit residuals should be Gaussian distributed around a zero mean value. If this is not the case, like one can see in the residuals histograms of fig. 5.6, then it reveals misalignment between the wire chambers. We then proceed to a alignment software correction that consists in redefining the wire chambers coordinates by taking into account the systematic shifts.

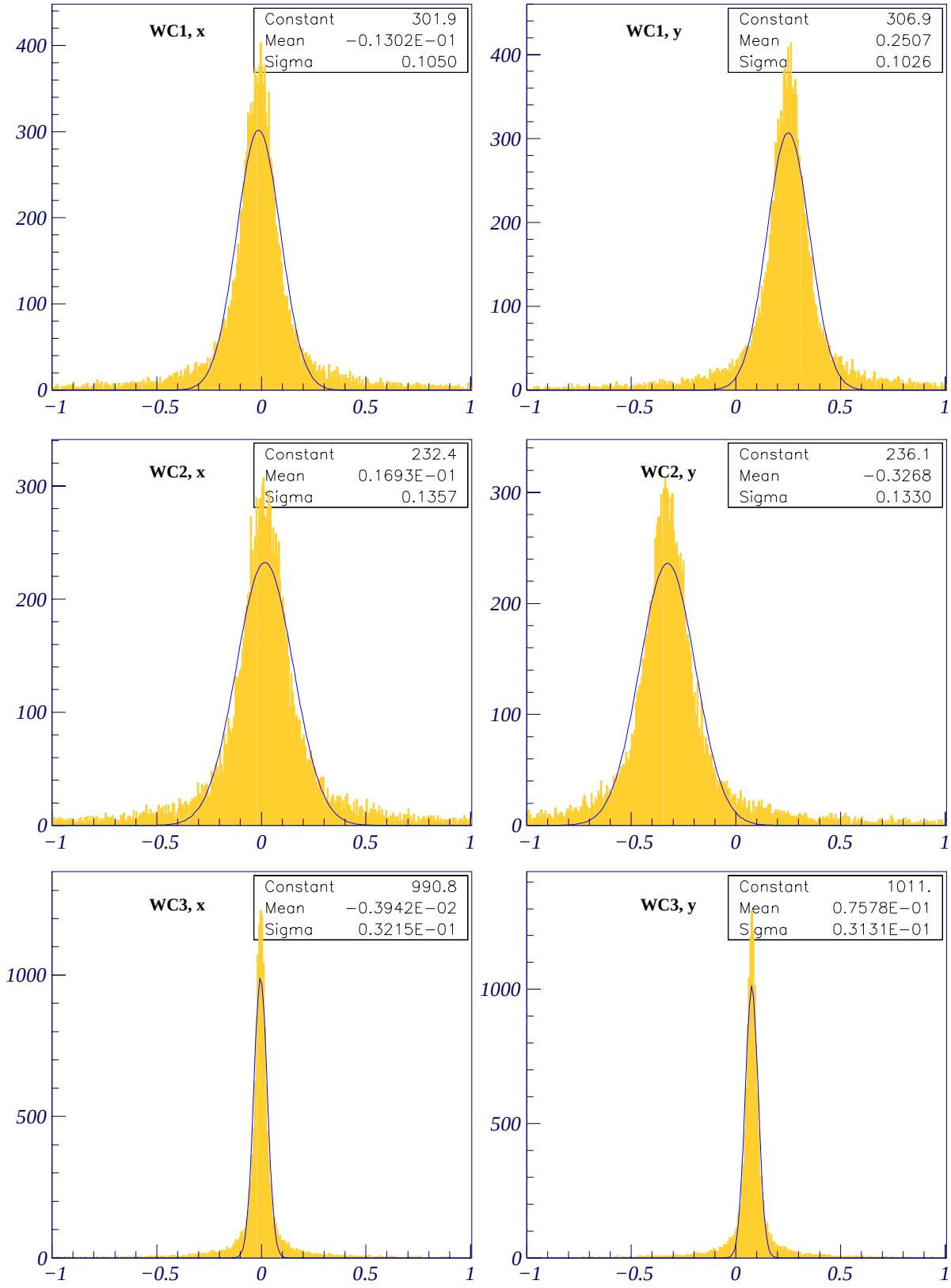

Figure 5.6: *Residuals distributions used to inter-align the 3 wire chambers on run 10 (given in cm). Residual is here defined as the extrapolated value coordinate from the track fit minus the measured coordinate. Left column stands for x coordinate. Right column stands for y coordinate.*

A remark is maybe worth to better understand the alignment procedure meaning. This has to do with the fact that as no external information is used, - external to the wire chambers - the alignment procedure may result in a non orthogonal reference frame as figure 5.7 illustrates. The point is that the only thing the described alignment procedure is able to do is to align the wire chambers origins in a straight line, but without any grant that this line is normal to the wire chambers.

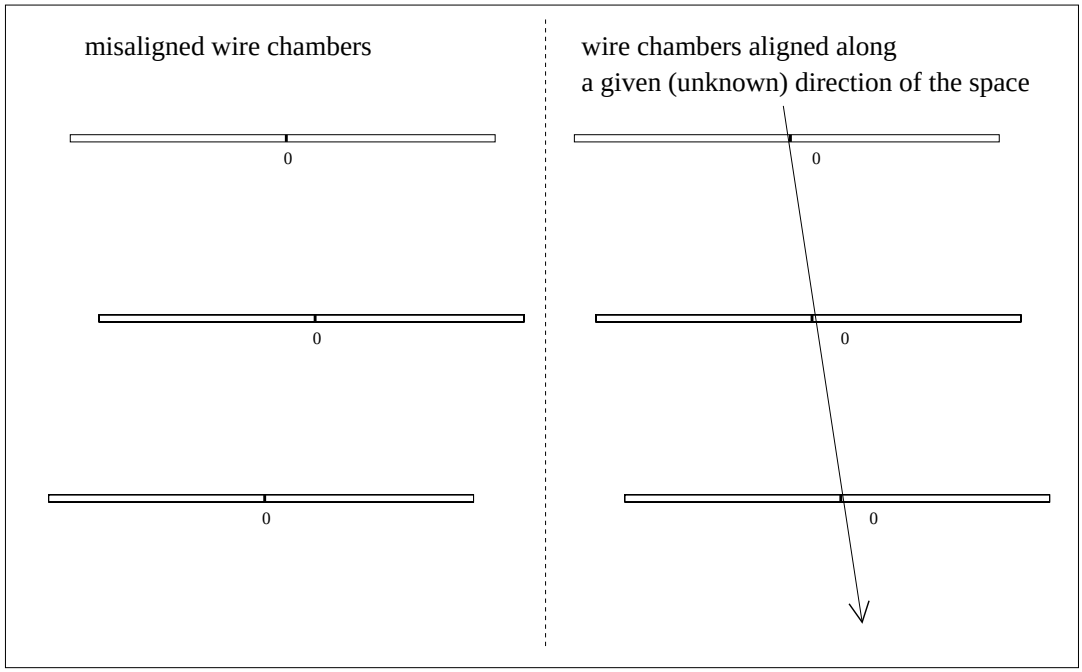

Figure 5.7: *Illustration of the misalignment between the wire chambers. While in the right (before alignment), there is 3 different Cartesian orthogonal reference frames, in the left case (after alignment), there is one single not orthogonal reference frame.*

Still, given the smallness of the misalignments, the final situation of the right above figure is preferred to the one of the left. The described alignment procedure has then been applied to all data runs. Table 5.3 summarizes the performed corrections along the runs. As expectable, the corrections are very nearly the same for all the runs.

Prototype misalignments (in cm)									
	Wire Chambers inter-alignment corrections							WC-PMT	
	WC1		WC2		WC3		check	corrections	
run	Δx	Δy	Δx	Δy	Δx	Δy	sum	Δx	Δy
10	-0.01	0.25	0.00	0.08	0.02	-0.33	0.7	0.20	-0.33
12	0.03	0.25	0.02	0.08	-0.04	-0.32	0.8	0.22	-0.33
15	-0.02	0.24	-0.01	0.07	0.03	-0.32	0.7	0.18	-0.34
16	-0.02	0.25	-0.01	0.07	0.03	-0.32	0.7	0.20	-0.33
20	-0.02	0.24	-0.01	0.07	0.03	-0.31	0.7	0.21	-0.35
22	-0.02	0.27	-0.01	0.08	0.02	-0.35	0.7	0.22	-0.32
24	-0.02	0.24	-0.01	0.07	0.02	-0.31	0.7	0.24	-0.35
25	-0.02	0.25	0.00	0.07	0.02	-0.32	0.7	0.22	-0.34
27	-0.01	0.24	0.00	0.07	0.02	-0.32	0.7	0.20	-0.34
29	-0.02	0.25	0.00	0.08	0.02	-0.33	0.7	0.18	-0.35
31	-0.02	0.24	0.00	0.07	0.02	-0.31	0.7	0.18	-0.37
32	-0.01	0.26	0.00	0.08	0.02	-0.34	0.7	0.19	-0.35
33	0.00	0.26	0.00	0.08	0.00	-0.33	0.7	-	-
34	-0.02	0.23	-0.00	0.07	0.03	-0.32	0.7	-	-
35	-0.01	0.26	0.00	0.08	0.00	-0.35	0.7	-	-
45	-0.02	0.27	-0.01	0.08	0.03	-0.36	0.8	-	-
46	-0.02	0.27	-0.01	0.08	0.03	-0.35	0.8	0.23	-0.34
48	-0.02	0.29	-0.01	0.09	0.02	-0.38	0.8	0.23	-0.31

Table 5.3: *We summarize here the corrections used for the misalignments between the RICH prototype components for the cosmic runs. The column* WC *refer to wire chambers inter-misalignments described in section 5.3.1. The* WC-PMT *values refer to the misalignment between the aligned WC frame and the PMT matrix frame described in section 5.3.2. The column "*check sum*", corresponding to the sum of the absolute values of all WC misalignments, shows that the WC inter-misalignment was constant during the runs.*

5.3.2 Alignment of the Wire chambers with the PMT matrix

Once the wire chambers are aligned with respect to each other, one must check for the eventual misalignment between the wire chambers reference frame just obtained and the frame where the PMT hits coordinates are given. For this, one simply has to use a point whose coordinates can be known in both reference frames and compare it. Such a point exists. It is given by the particle hits cluster, already described in section 3.2.1.

Due to the large signal developed in the PMT matrix by the particle passage through the light guides, it is possible to detect it in the PMT matrix reference frame. One just has to look for a sufficiently strong pixel signal to be sure it can't be due to a single photon coming from the radiator, and then compare the PMT matrix coordinates of this point to the coordinates obtained by the track extrapolation to the PMT matrix. The event display in next figure (fig 5.8) illustrates well what we're talking about.

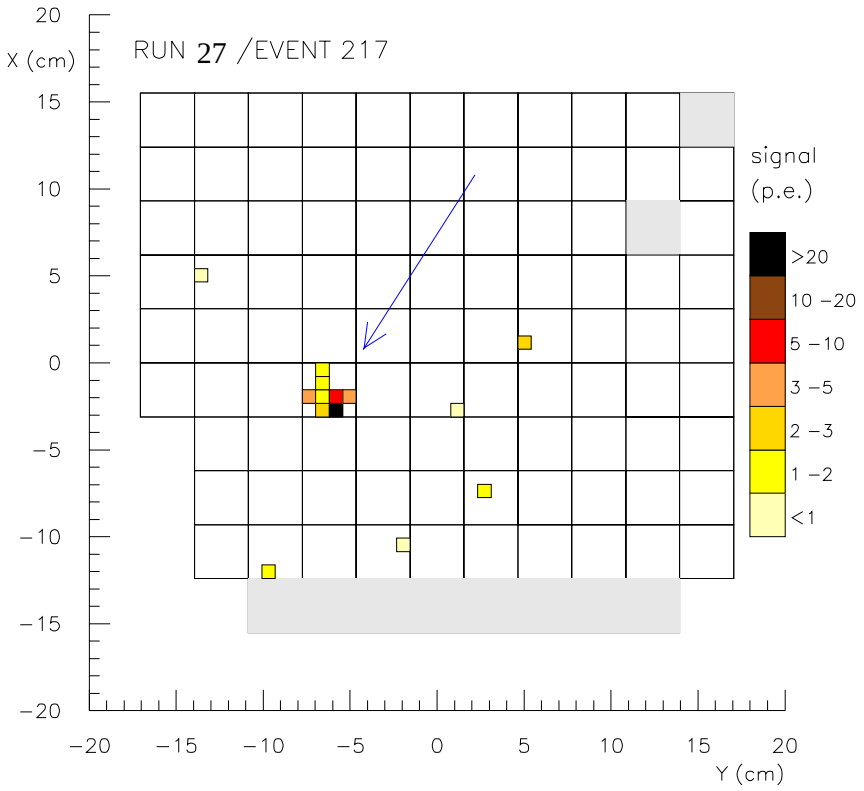

Figure 5.8: *Event display for event 217 of run 27. The particle track projection is depicted by the arrow. The particle cluster is well visible and far away from the track extrapolation. Its signal is spread over 8 pixels, summing more than 30 photoelectrons.*

This comparison is of course done for all the events of the run and *histogramed* in order to check for an eventual systematic shift from zero. In fact, the event of fig. 5.8 is an extreme example of occasional misalignment between the track and the particle cluster, maybe due to some occasional malfunctioning of the wire chambers. We'll come back to these events in next section. In general, what happens is more like in the event display of figure 5.9 and the misalignment is much smaller than the one suggested by figure 5.8.

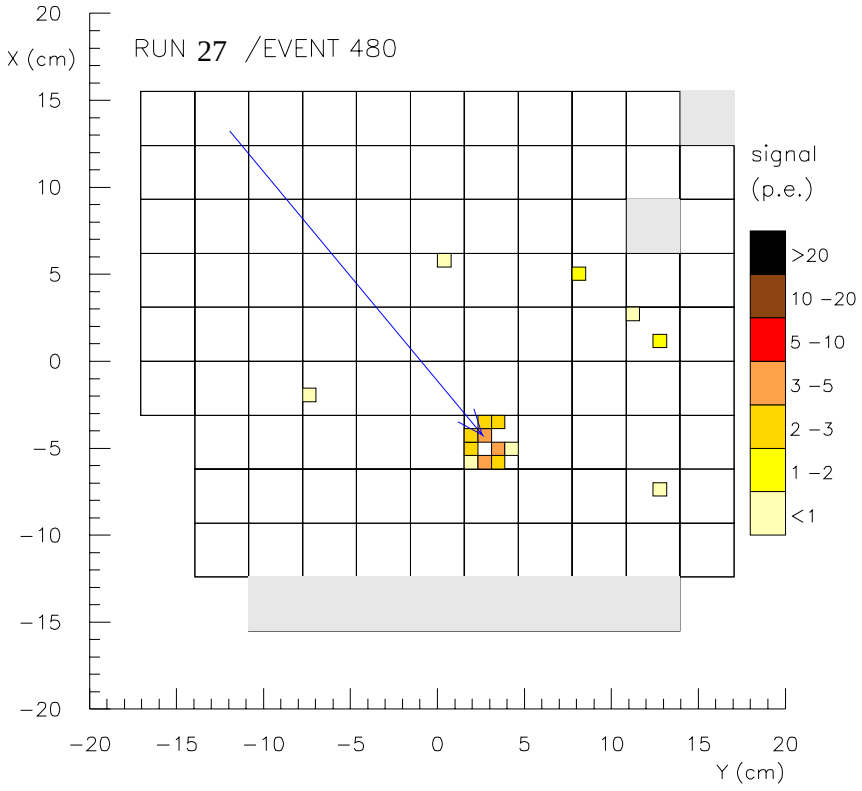

Figure 5.9: *Event display for event 480 of run 27. The particle track projection is depicted by the arrow. The particle cluster and the ring hits are well visible.*

The misalignment is searched for in x and y separately, like before in the wire chambers case. The minimum signal used to reveal the particle presence in the light guides was 5 photoelectrons. This value is object of study in the next section. The results of this misalignment study are summarized in the previous table 5.3, where we give the corrections applied to the PMT matrix frame in order to bring it coincident with the wire chambers frame. The systematic shift between the particle track and the particle cluster positions was in average of the order of 0.5 cm.

5.4 Event selection

We are now almost ready to reconstruct Cherenkov rings. Before that, we just have to apply some quality criteria to select "reconstructible" events.

track fit quality

Figure 5.10 shows the χ^2 distribution for the track fits for both data (dots histogram) and simulation (solid bars histogram) [2]. By the large tail of the data results, the resolution of the real wire chambers is clearly worst than the simulated. It has been considered reasonable to select particle tracks with a χ^2 lower than 1. This value means a efficiency for this selection cut that varies between 96.7% (run 12) and 84% (run 48). After selecting these events, one gets an acceptance distribution for the particle polar angle, which peaks at values between 4 to 5 degree, according to the setup of the run (see fig. 5.11).

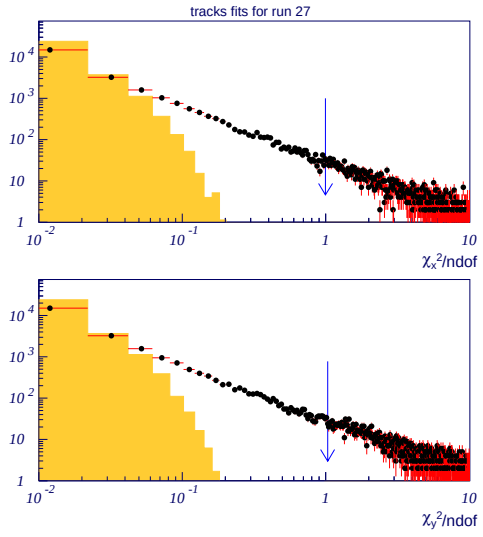

Figure 5.10: *χ^2 distribution for the linear fits to the particle tracks (both x-z and y-z fits illustrated). The tail requires a selection cut ($\chi^2_{cut} = 1$).*

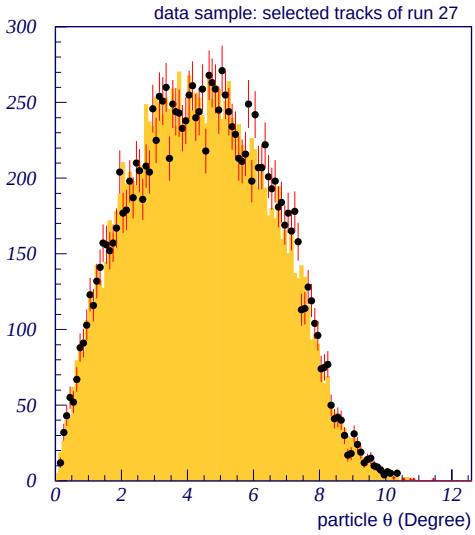

Figure 5.11: *The prototype polar angle acceptance has its maximum about 4 to 5 Degree.*

[2] From now on, except otherwise specified, this same convention is used to distinguish real data from simulation results.

matching between track and PMT matrix informations

By looking to some event-displays, like the one of figure 5.8, one sometimes finds events where the track doesn't agree at all with a perfectly visible particle cluster. This can be due to an occasional malfunctioning of the wire chambers.

These events should be looked as suspicious and rejected once there is no confidence about the track information. So, after having used the particle cluster to align the PMT matrix with the wire chambers, this is again used to better select the events we are going to reconstruct.

Figure 5.12 presents the *matching* residuals after correcting for the wire chambers-PMT matrix misalignment. These are more or less Gaussian distributed with a σ of about $0.6\,cm$. The curve of fig. 5.13 corresponds to the integration of the histograms of fig. 5.12 and so represents the variation of the efficiency in accepting events with the chosen value of the matching residual cut. For the real data, a matching cut of $1.5\,cm$ represents a selection efficiency rate of about 90%.

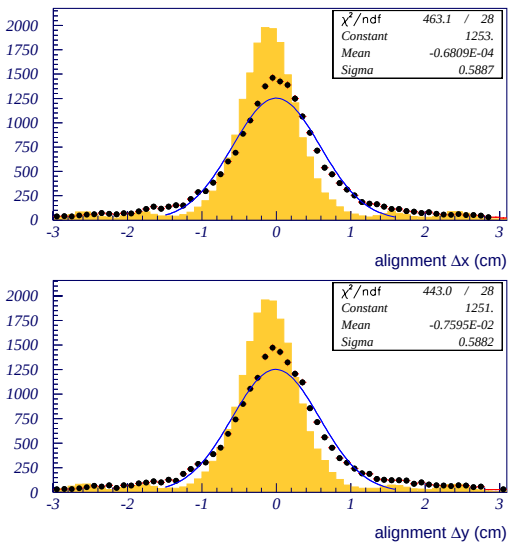

Figure 5.12: *Distribution of the matching residuals between particle track and particle cluster, after performing the WC-PMT matrix alignment that brings the peak to zero.*

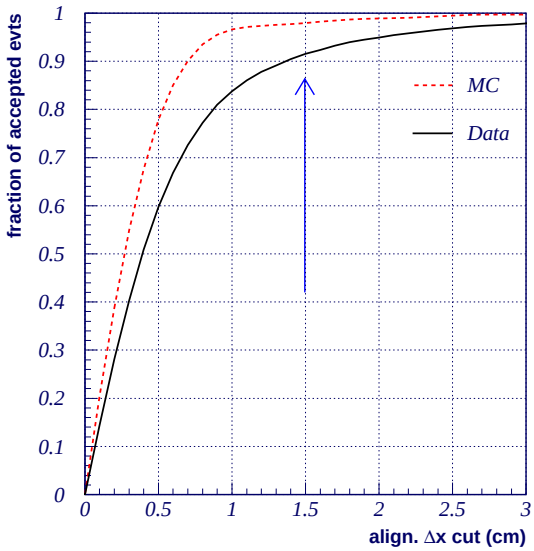

Figure 5.13: *Efficiency of the track-(particle signal) matching criterion. The cut of 1.5cm corresponds a little less than 3 sigma of the matching distribution.*

The meaning of this selection criterion is a bit like if we were adding a 4^{th} point to the wire chambers hits, in order to better define the track. Nevertheless, we

don't add it to the 3 wire chambers points in order to perform a 2^{nd} track fit, because the spatial resolution of this 4^{th} point is much worst than the one of the wire chambers hits. What's being done is simply to reject some events to get more confidence about the events selected sample, for which we are going to reconstruct the Cherenkov angle.

optimization of the particle PMT signal definition

After establishing a matching criterion, we now search to optimize the PMT signal definition for the particle cluster. We remind that up to now, the particle cluster coordinates were taken to be given by the pixel with a signal larger than 5 photoelectrons. Nevertheless, if one plots the matching residuals against the pixel signal taken to represent the particle cluster, one concludes that this last is a very spread variable. Even in the simulation, the particle can leave signals going from less than one up to almost 50 photoelectrons per pixel. When using this variable to estimate the particle presence, there is a region of confusion with the lower signals due to photons coming from the radiator. So, it is important to define what is the minimum value that grants the particle presence in the PMT matrix. This is the purpose of the next study.

For this, we split the highest PMT signal in two populations: signals that obey our matching criterion and signals that are farther than $5\,cm$ from the track extrapolation. These populations should correspond to the real particle PMT signals and the (truly) background PMT signals. If we superimpose these signal populations, one gets two distinct signal populations as can be seen from figure 5.14. Note that for each population, the results for simulation (bars histograms) and real data (dots histograms) are presented.

For the *non-matching* hits population, the signal distribution completely ends about 5 photoelectrons, while for the *matching* hits, the signal goes up to 50 photoelectrons. However, the degree of confusion is higher than desirable. This has motivated the search for another estimator of the particle cluster.

So instead of using the single highest pixel signal of the event, we can repeat the same study using the highest PMT integrated signal (meaning the sum of the 16 pixel signals). When doing so, one obtains the corresponding histograms of figure 5.15. It is interesting to note that this variable shows a better agreement between

the Monte Carlo simulation and the data.

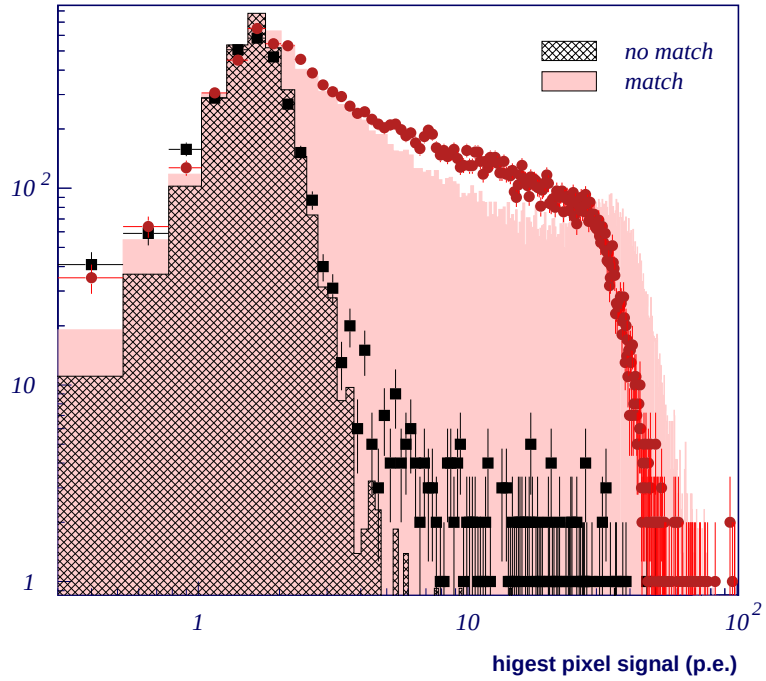

Figure 5.14: *Highest pixel signal for the* matching *and* non matching *populations.*

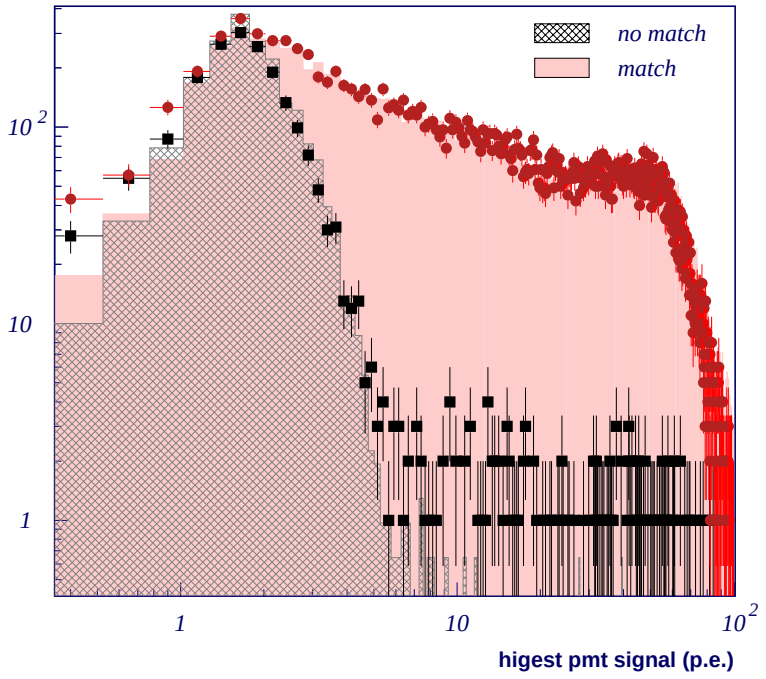

Figure 5.15: *Highest integrated PMT signal for the* matching *and* non matching *populations.*

To compare the efficiency of these two different estimators, we show plots 5.16 and 5.17, obtained from integration of the previous histograms. We can see that for a same background level of about 10% (background is here defined as non-matching hits accepted by the cut signal), the estimator based on the highest integrated PMT signal is a bit more efficient than the highest pixel signal: $\sim$ 84-85% against 80%. In view of this, we have chosen the highest PMT integrated signal as our estimator to reveal the particle cluster presence, with a minimum value of 4 photoelectrons.

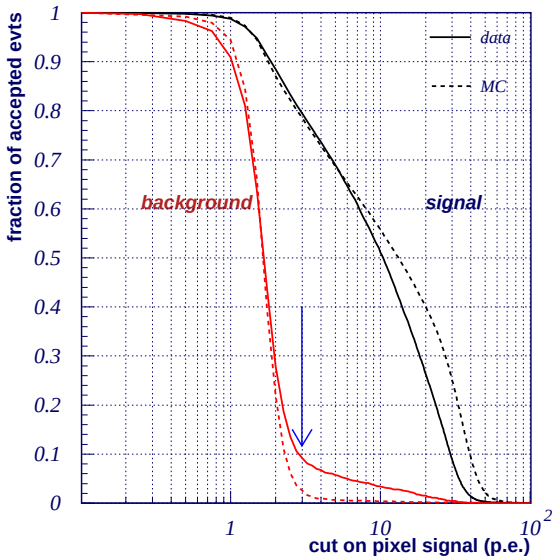

Figure 5.16: *Efficiency of particle selecting criterion using highest pixel PMT signal (background "efficiency" is also plotted).*

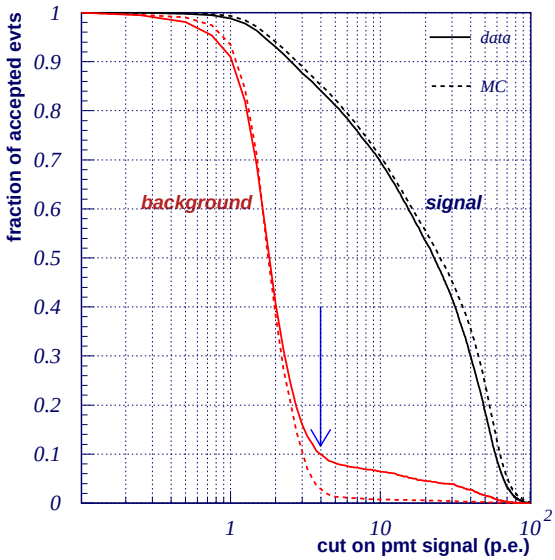

Figure 5.17: *Efficiency of particle selecting criterion using highest integrated PMT signal (background "efficiency" is also plotted).*

Summarizing this section, our events selection criteria are:

- A good track fit χ^2 ($\chi^2 < 1$);
- A strong signal revealing the particle passage through the light guides (this is taken as a PMT integrated signal of at least 4 photoelectrons);
- A good match between the particle cluster position and the track extrapolation (distance lower than 1.5 cm in each coordinate)

5.5 Reconstruction Results

5.5.1 The cosmic muons spectrum

In order to compare between the Monte Carlo and real data results, the simulation has been feed with ed with the muons velocity spectrum taken from reference [22] (page 359). This corresponds to the fit to a large survey of experimental measures valid in a range between 0.2 and 20 GeV/c (in muon momentum), at the sea level and low North latitude. The specific flux law is given by:

$$\frac{dN}{dp} = 3.09 \cdot 10^{-3} p^{-0.4854 - 0.3406\ ln(p)} \quad [cm^{-2} s^{-1} sr^{-1} (GeV)^{-1}]$$

Figure 5.18 shows this flux law (in momentum and velocity).

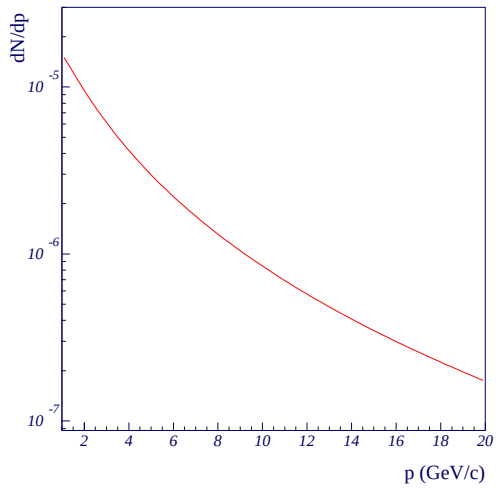

Figure 5.18: *Cosmic Muons momentum spectrum at sea level (latitude 12º North).*

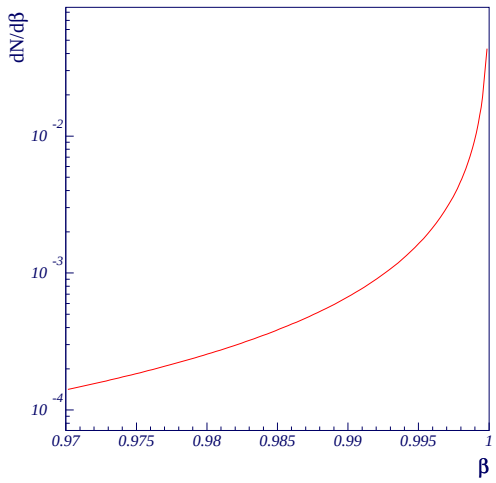

Figure 5.19: *Corresponding Cosmic Muons β spectrum.*

The knowledge of this velocity spectrum shape was also useful in the following. The processed data runs 31, 32, 46 and 48 had a radiator composed by 3 different aerogel tiles, with an unknown spatial disposition to the author of this thesis. The used tiles were a Novosibirsk aerogel sample with a refractive index 1.02 (3cm thickness), and two other tiles with indexes of 1.03 and 1.05, both 2cm thick.

The first step to process these runs was to proceed to the spatial mapping of the radiator tiles. For this, and taking into account the velocity distribution of the cosmic muons (see fig. 5.19), we looked for $\beta = 1$ rings, which are the most of the

events, with at least 3 hits and we mapped the particle *impact points* at the radiator level.

This ring search was done using the pattern tracing package of the reconstruction, imposing θ_c corresponding to $\beta \sim 1$, instead of searching for it through a minimization. The obtained map is given in figure 5.20.

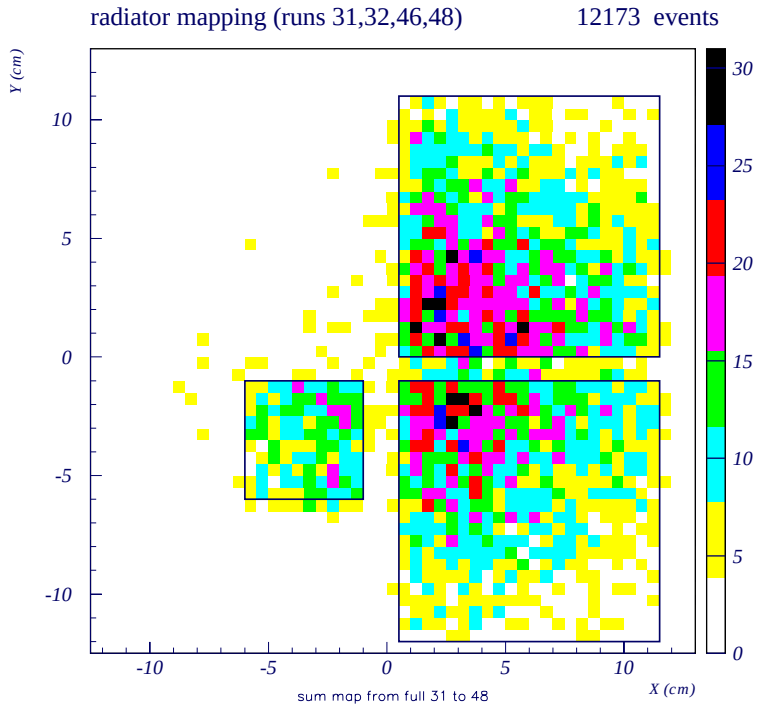

Figure 5.20: Multi-radiator *configuration runs mapping. One can clearly distinguish the 3 tiles.*

The identification of which tile is which, is then possible by trying the reconstructions with the 3 different radiator indexes, and then see which index better adjusts to the muons velocity spectrum (with a peak for $\beta \simeq 1$). We illustrate this for the top tile, which turns out to be the aerogel 1.03 as we can conclude from the 2 reconstructed spectra of figure 5.21.

The left bottom tile is the aerogel 1.05 and the small tile corresponds to the aerogel 1.02. In the following, the results for the 1.02 tile are not presented due to the lack of statistics (the accumulation of the 4 *Multi-radiator* runs give less than 1000 events in this tile). For 1.03 tile, there are about 5000 events available, and something like 4500 events for the 1.05 tile (this radiator gives a smaller ring acceptance due to the larger Cherenkov angle).

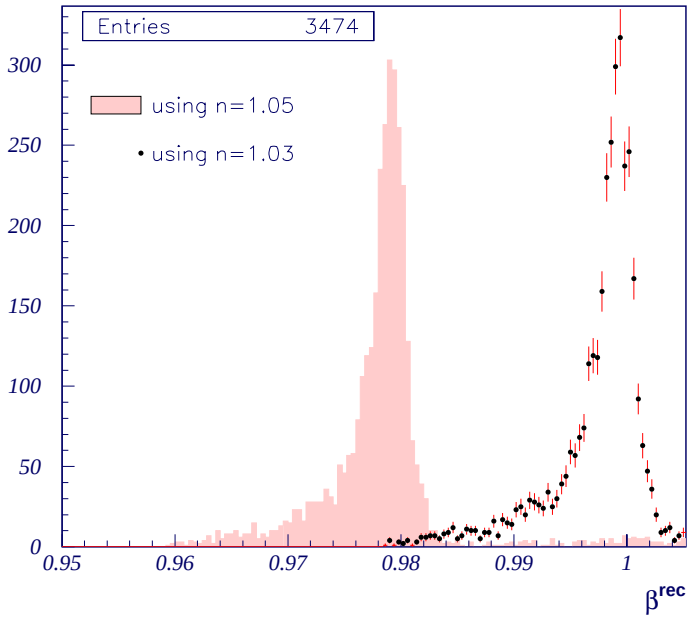

Figure 5.21: *Two resulting muons velocity spectra, used to identify one of the tiles of the* Multi-radiator *configuration runs (this one is for the tile located in the positive quadrant of the coordinates of fig. 5.20).*

5.5.2 Reconstructions selection (Kolmogorov test to the azimuthal hits distribution)

Before studying the reconstructed velocity spectrum, some more selection may be convenient as we next show. Reconstructions like the ones in figure 5.22 should be rejected on the basis of a given criterion, once they clearly correspond to odd reconstructed rings compared to the nice one given in figure 5.23. These *odd* events present a kind of clusterization of the ring hits.

Such a clusterization is in principle detectable by accessing to the azimuthal angle corresponding the concerned hits. Remember that the Cherenkov emission is uniform on the azimuthal angle φ (see fig. 3.2), leading thus directly to the possibility of testing this feature, since the reconstruction of this work provides us with this precise azimuthal emission angle for each hit of the pattern (see description of the photon tracing in section 3.1.1, pages 41 to 42).

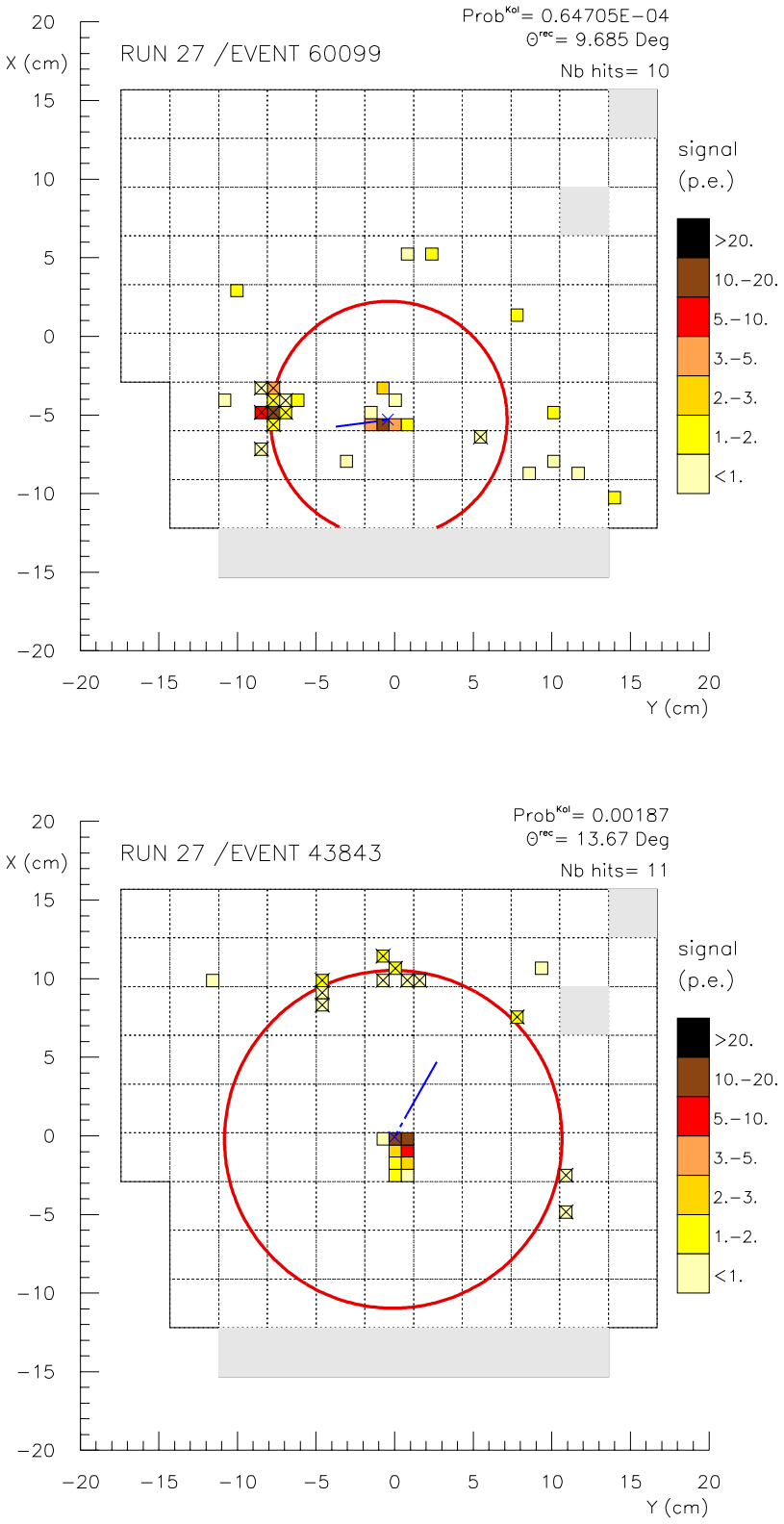

Figure 5.22: *Odd reconstructed rings. Top event corresponds maybe to a coincidence of two muons. The asymmetry on the spread of the hits on the bottom reconstructed ring makes it a suspect Cherenkov ring. Such reconstructions should be rejected on some basis.*

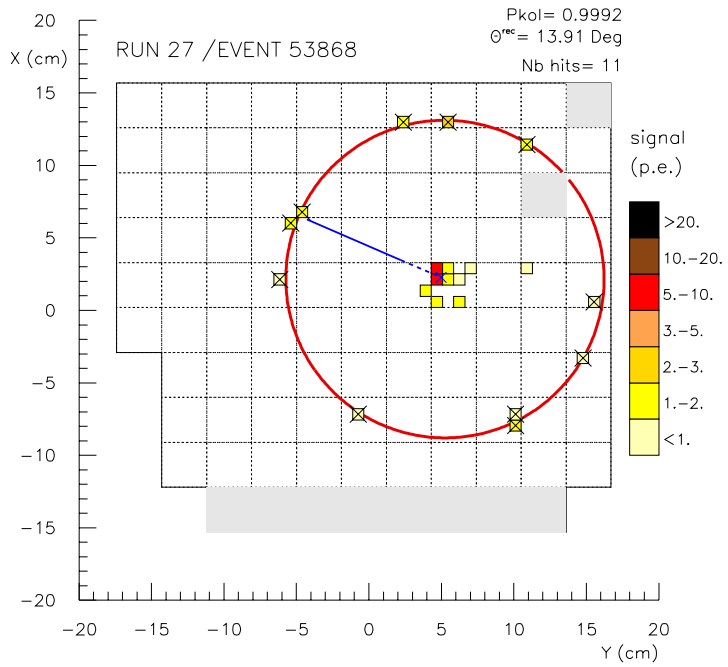

Figure 5.23: *A nice Cherenkov ring. Here the hits are well uniformly spread along the ring, which makes it a more likely true Cherenkov ring than the reconstructions of figure 5.22.*

The tool used to do this is the Kolmogorov test which can be used to test the compatibility between the φ distribution of the hits obtained in the reconstructed ring and the uniform model. The resulting compatibility-test probabilities for the reconstructions of runs 12,27 are shown in histogram of fig. 5.24.

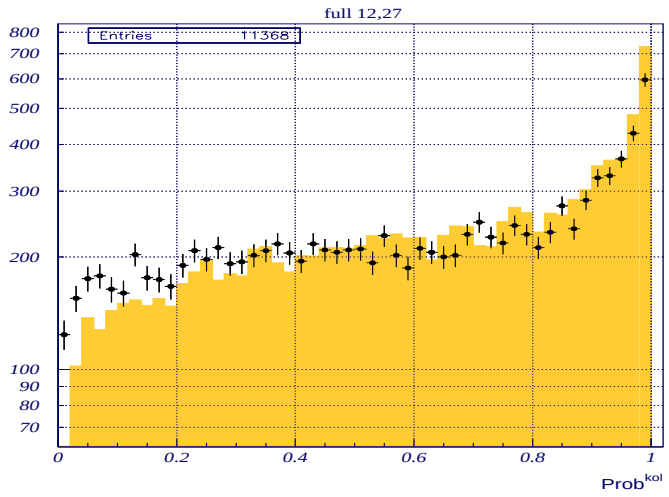

Figure 5.24: *Distribution of the compatibility-Kolmogorov-test probabilities for the reconstructions of runs 12 and 27.*

Obviously this probability spectrum is not as much discriminative as we would like, in the sense there are not two separated populations. The following question then arises. How small must be the Kolmogorov-test probability in order to safely indicate an odd reconstruction? In order to establish the value of this cut, it was proceeded as follows.

Different samples of the reconstructed velocity spectrum were selected based on different Kolmogorov probability cuts and the compatibility of the resulting spectra with a reference one was tested.

If the low probabilities reconstructions correspond to purely background events, the resulting velocity spectrum should have a completely uncorrelated shape compared to the muons velocity spectrum. This reference spectrum was taken as corresponding to reconstructions with a Kolmogorov probability higher than 50% and having at least 5 hits in order to be sure about the reconstructions.

The candidate samples to *pure background* were taken by selecting reconstructions with probability lower than a given value. The reference sample and three of these background candidate samples (all normalized to unit) are given in figure 5.25 and left fig. 5.26. It can be appreciated that the shape of the selected samples is quite different from the reference spectrum.

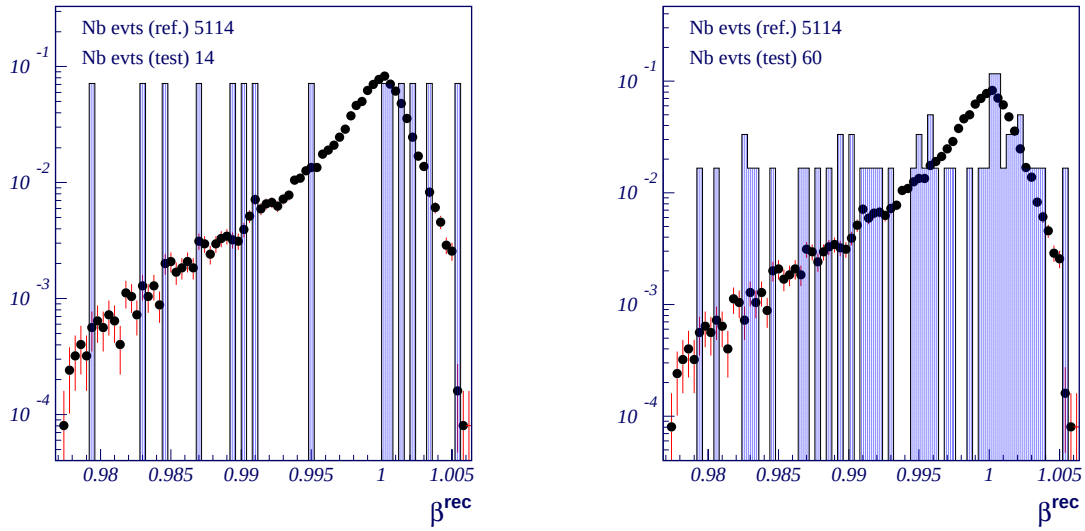

Figure 5.25: *Comparison between two samples of the reconstructed velocity spectrum selected by small Kolmogorov probabilities (bars histograms) and a reference (dots histogram). The background samples correspond to reconstructions with probability lower than* 5×10^{-4} *and* 5×10^{-3}*, respectively for the histograms of left and right. All histograms are normalized to the unit.*

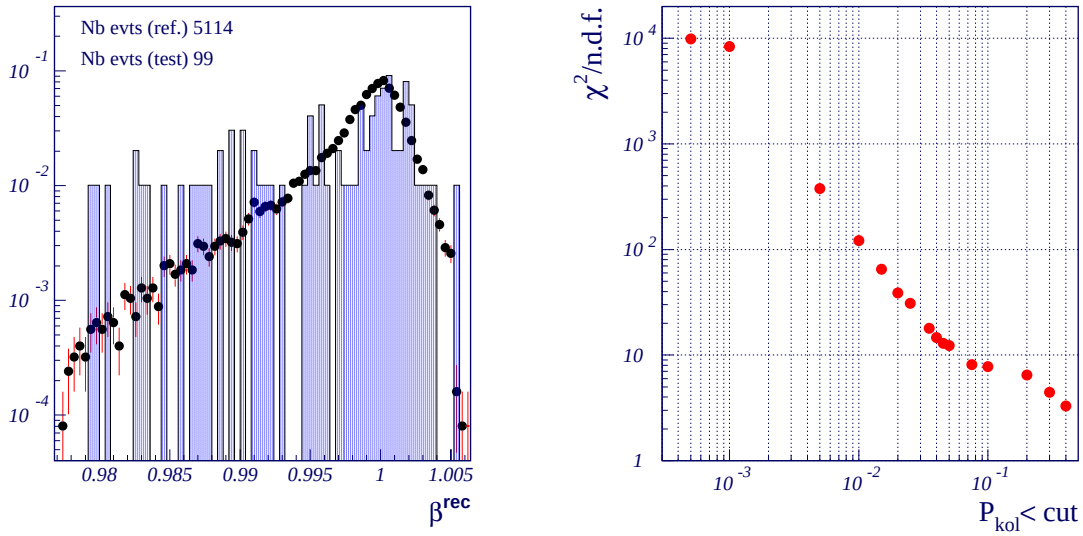

Figure 5.26:

Left: background sample with probability lower than 5×10^{-2}.

Right: computed χ^2 *between the different background samples and the reference spectrum.*

The right plot of figure 5.26 is the constructed "$\chi^2 - test$ curve" for the different samples [3]. It clearly shows that as the upper value of the Kolmogorov probability used to select the background samples increases, the compatibility between the comparing spectra increases. However, it is not correct to perform a real "χ^2 test" with these histograms since the selection criterion is quite opposite for the reference and the background spectrum histograms, and so a true compatibility must be hardly expected. To pick up a value separating reasonable from *odd* events from the Kolmogorov-test point of view, the χ^2 curve of last figure is however not helpful.

Instead of selecting reconstructed rings with a Kolmogorov probability lower than a given value and then test for its *non compatibility* with a reference spectrum, we can select events with Kolmogorov probability higher than a given value and then test for *compatibility* with the reference spectrum.

That's the result of this Chi-square test that is given in the next figure 5.27. One can see that the compatibility probability drops about a Kolmogorov probability of about 2×10^{-2}, and although it doesn't drop down to a zero probability compatibility value, it shows that bellow this critical value for the Kolmogorov probability, a certain degree of contamination of the selected velocity spectrum starts to occur. The fact that this contamination is low in statistical terms, reflects itself on the still high asymptotic value for the χ^2 probability.

[3] see chapter 12 of reference [23] for this $\chi^2 - test$ issue

By looking at some individual reconstructions and their Kolmogorov probabilities, one gets the feeling that events like the ones of figure 5.22 always correspond to really small probabilities (6×10^{-5} and 2×10^{-3} respectively). That's these reconstructions that we want to reject, and the "curve" of fig. 5.27 gives us the rejection criterion corresponding to let's say, events with a Kolmogorov probability lower than 10^{-2}.

For this value, the signal selection efficiency is about 98%. It should be emphasized that the Kolmogorov test gets of course more significant as the number of hits of the reconstructed ring gets higher. However, as we only use it to reject very anomalous events (with very low probabilities) and not to establish continuous levels of quality among the reconstructions, its use may be considered acceptable.

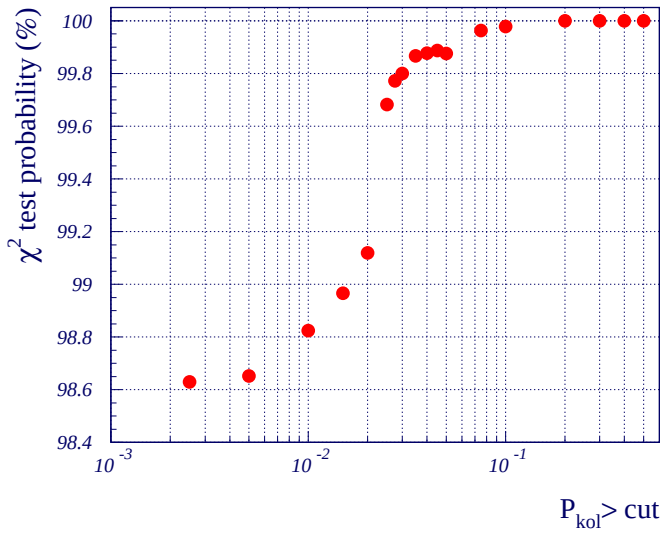

Figure 5.27: *Chi-square test result used to establish the Kolmogorov test probability cut value (bellow which value we reject a Cherenkov reconstruction). The testing hypothesis is here that the tested spectrum is a sampling from the reference spectrum. This hypothesis is clearly rejected for Kolmogorov probabilities lower than about* 2×10^{-2}.

As a final note on this issue, we show the distribution of the number of hits (on the reconstructed ring) for events with a Kolmogorov probability bellow the rejection cut value ($< 10-2$) and for events with a K. probability above 10^{-1}; see figure 5.28. It is satisfactory to verify that these two populations are also distinct from the point of view of the number of hits, being the cluster events (low K. probabilities) associated to a higher mean number of hits.

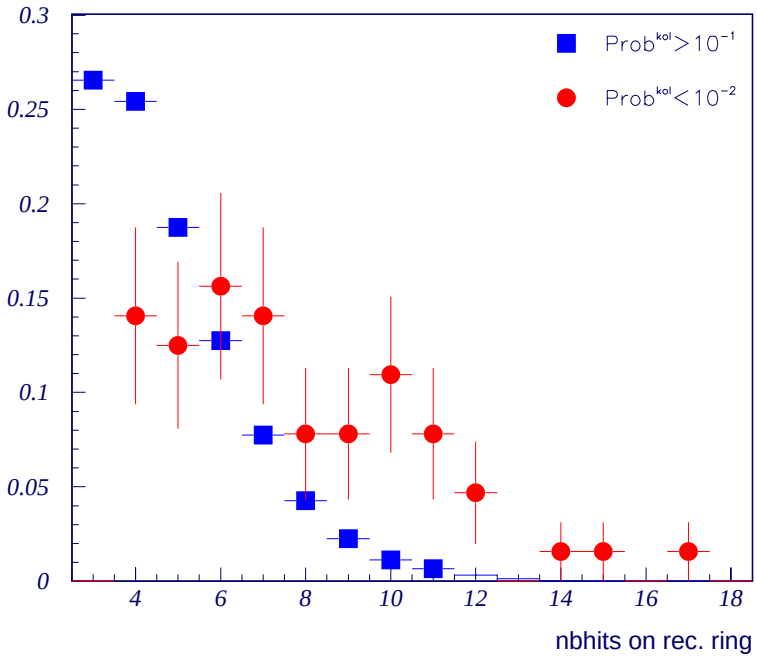

Figure 5.28: *Distributions of the number of hits for the reconstructed Cherenkov rings with low and high Kolmogorov test probability.*

5.5.3 Velocity resolution results

Now that the events selection criteria are established and presented, we can move on to the velocity reconstruction results. Because one doesn't know the muon's velocity, one can not really evaluate the velocity resolution with the data. Nevertheless, due to the muons velocity spectrum of fig. 5.19, it is possible to have a rough estimator.

If one considers that most of the reconstructions with $\beta > 1$ are due to $\beta = 1$ muons, then we just have to fit the ending part of the muons reconstructed spectrum with a Gaussian function.

The single hit resolution is also evaluated just as we did in chapter 4, with the obvious difference that instead of fitting the distribution of the variable $(\beta^{\text{rec}} - \beta^{\text{sim}}) \times \sqrt{Nb_{\text{hits}}}$, we fit the ending part of the reconstructed spectrum on $(\beta^{\text{rec}} - 1) \times \sqrt{Nb_{\text{hits}}}$. This is a better estimator of the intrinsic resolution to each prototype configuration (radiator plus drift volume) than the total resolution. This estimation is shown in figures 5.29 and 5.30 for two different radiators.

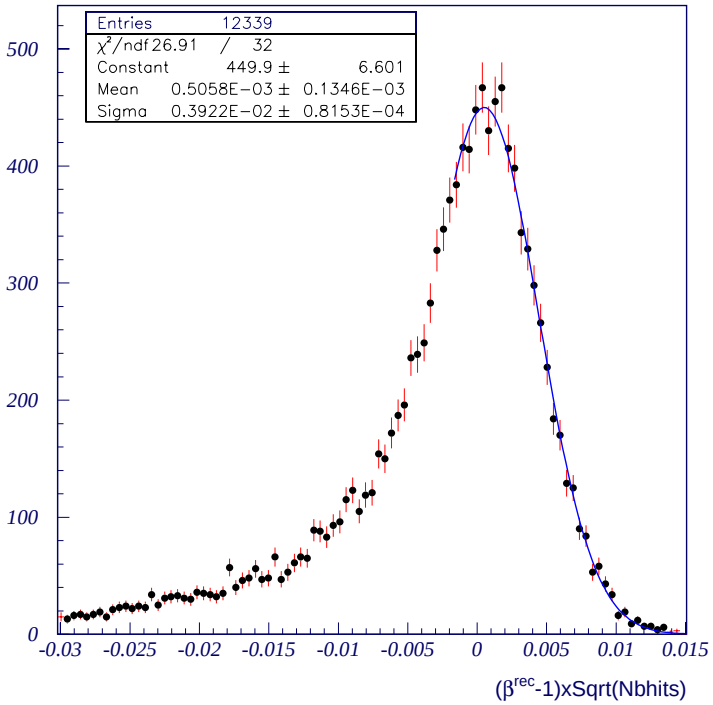

Figure 5.29: *Single hit velocity resolution estimation for summed data of runs 12 and 27 (n=1.03(3cm thick.),drift=41.65cm)*

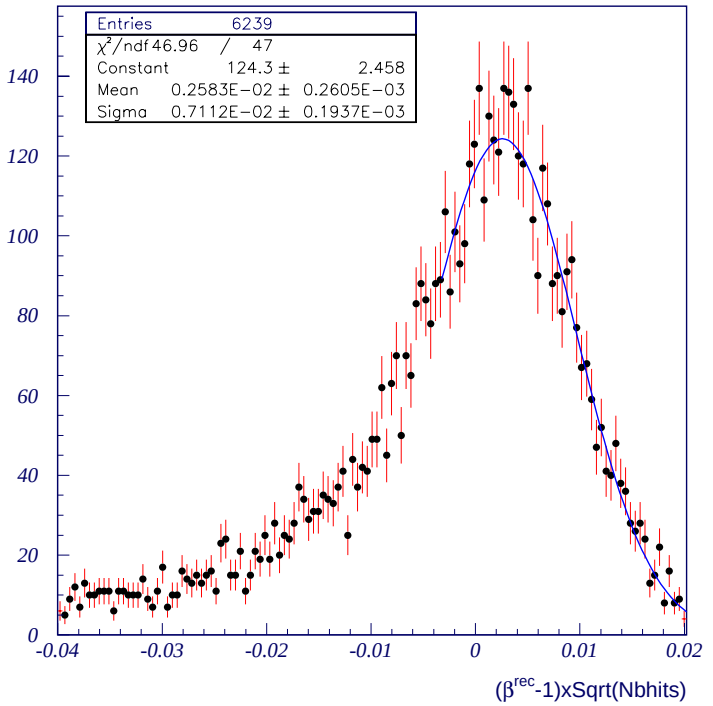

Figure 5.30: *Single hit velocity resolution estimation for summed data of runs 15 and 16 (n=1.05(2cm thick.),drift=41.65cm)*

Tables 5.6 and 5.5, at the end of this section summarize the total and single hit velocity resolutions. Next figures 5.31 and 5.32 gather the same information in a more readable form.

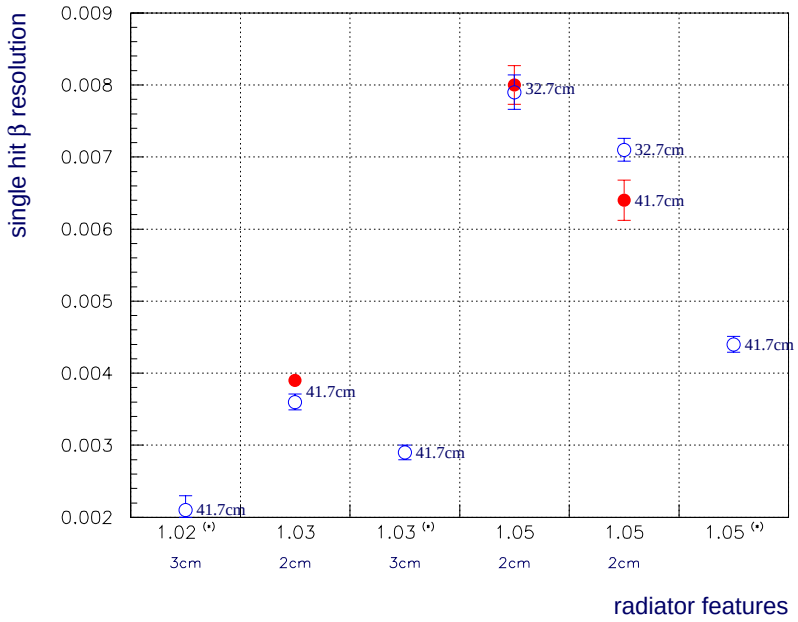

Figure 5.31: *Single-hit resolutions for the analyzed aerogel runs. Full dots represent runs with the plastic foil present under the radiator, and hollow without. The aerogel radiators signaled with (*) are different samples (*multi-radiator *runs). The drift volume is also indicated.*

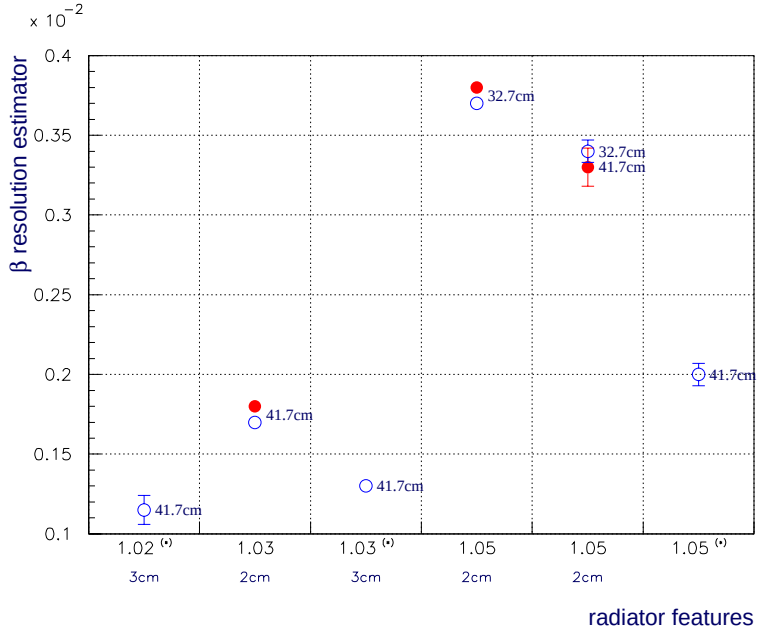

Figure 5.32: *Resolutions for the analyzed aerogel runs. The same symboling of fig. 5.31 is used.*

A comment for the worst resolution here obtained, even in the case of simulation, compared to the results of last chapter is needed. The main reason for this is due to the poor track resolution of this setup. The resolution in the wire chambers hits is considered to be of 2mm. Remind that the silicon tracker will have a much better resolution - of the order of $10\mu m$.

From the reading of the results given in figure 5.31 (or 5.32), one can conclude about the following items:

As expectable, the lower refractive index sample of aerogel 1.02 achieves the best resolution. Nearly following comes the 1.03 sample of runs 31-48. The worst resolution is achieved by the $3\,cm$ sample 1.05.

The foil has no appreciable effect on the velocity resolution and although measurable, the radiator thickness is also not a critical issue.

An additional remark goes for the surprising fact that the change in the drift volume in the 1.05 runs (runs 10 and 15-16, with drifts of $41.65\,cm$ and $32.65\,cm$ respectively), didn't show to have any appreciable effect in the resolution. If we neglect the foil effect, run 10 should have a resolution value about 80% from the 15-16 runs. This effect must be masked by other effects.

Besides these estimators, another interesting mode to compare the different setup characteristics is to compare the pattern fit residuals distributions for each of the runs.

In the prototype setup, it is possible and easy to define the *inside* and the *outside* of the pattern ring. This is why the residuals distributions of figure 5.33 are complete and not just one-sided as in the flight setup. This complete residual distributions are much more satisfactory to define the Likelihood Gaussian width than the one-sided distributions.

Table 5.4 compiles these residuals widths. The systematically larger values found for data compared to simulation indicates some feature not well described in the simulation like for instance the chromaticity.

Just like the final resolution, this variable describes the radiator setup, once the larger values are associated to the 1.05 runs, and it seems to distinguish the thickness of the radiator by giving also larger valuers to the thicker radiator setups.

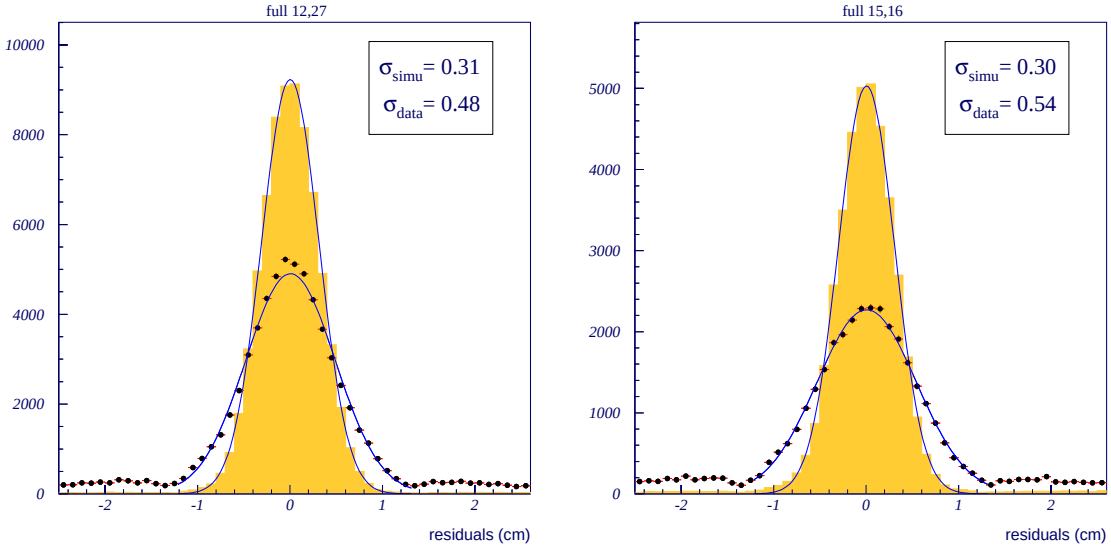

Figure 5.33: *Pattern fit residuals distributions. Left: runs 12-27 (AgL 1.03 - MC plus data). Right: runs 15-16 (AgL 1.05 - MC plus data)*

☞ pattern residuals and velocity resolution tables

				Data	Simulation
RUN	rad index	drift (cm)	thick (cm)	σ (cm)	σ (cm)
31, 32, 46, 48	1.02	41.7	3	0.61	n.av.
12, 27	1.03	41.7	3	0.50	0.31
20		41.7	3	0.49	0.31
31, 32, 46, 48		41.7	2	0.49	n.av.
22	1.05	32.7	3	0.59	0.35
24, 25		32.7	3	0.58	0.35
15, 16		32.7	2	0.55	0.30
10		41.7	2	0.54	0.30
31, 32, 46, 48		41.7	2	0.54	n.av.
29	NaF	7.5	0.5	0.75	0.54

Table 5.4: *Pattern fit residuals for the cosmic runs. From runs 24,25 to 15,16 the decrease of the residuals width in the simulation follows the decrease of the radiator thickness from 3 to 2 cm.*

		Data	Simulation		
RUN	rad. index	$\widehat{\delta\beta}_{\text{single hit}}$	$\widehat{\delta\beta}_{\text{single hit}}$	$\delta\beta_{\text{single hit}}$	$\frac{\delta\beta}{\widehat{\delta\beta}}$
31, 32, 46, 48	1.02	$0.21{\cdot}10^{-2}$	—	—	—
12, 27	1.03	$0.39{\cdot}10^{-2}$	$0.22{\cdot}10^{-2}$	$0.18{\cdot}10^{-2}$	0.8
20		$0.36{\cdot}10^{-2}$	$0.23{\cdot}10^{-2}$	$0.18{\cdot}10^{-2}$	0.8
31, 32, 46, 48		$0.29{\cdot}10^{-2}$	$0.24{\cdot}10^{-2}$	$0.19{\cdot}10^{-2}$	0.8
22	1.05	$0.80{\cdot}10^{-2}$	$0.38{\cdot}10^{-2}$	$0.32{\cdot}10^{-2}$	0.8
24, 25		$0.79{\cdot}10^{-2}$	$0.39{\cdot}10^{-2}$	$0.33{\cdot}10^{-2}$	0.8
15, 16		$0.71{\cdot}10^{-2}$	$0.35{\cdot}10^{-2}$	$0.29{\cdot}10^{-2}$	0.8
10		$0.64{\cdot}10^{-2}$	$0.28{\cdot}10^{-2}$	$0.23{\cdot}10^{-2}$	0.9
31, 32, 46, 48		$0.44{\cdot}10^{-2}$	$0.33{\cdot}10^{-2}$	$0.26{\cdot}10^{-2}$	0.8
29	NaF	$2.3{\cdot}10^{-2}$	$1.6{\cdot}10^{-2}$	$1.5{\cdot}10^{-2}$	0.9

Table 5.5: *Velocity single hit resolution estimation for the cosmic runs. $\widehat{\delta\beta}$ is the estimator of the β resolution. $\delta\beta$ is the β resolution available on simulation (based on the $\beta^{rec} - \beta^{sim}$ distribution). By comparing the estimator and the resolution in simulation, one sees that the resolution is generally overestimated in about 10 to 20%.*

		Data		Simulation	
RUN	rad index	N^{rec}	$\widehat{\delta\beta}$	N^{rec}	$\widehat{\delta\beta}$
31, 32, 46, 48	1.02	478	$0.11{\cdot}10^{-2}$	–	—
12, 27	1.03	11 182	$0.18{\cdot}10^{-2}$	22 207	$0.11{\cdot}10^{-2}$
20		5 953	$0.17{\cdot}10^{-2}$	24 609	$0.10{\cdot}10^{-2}$
31, 32, 46, 48		4 105	$0.13{\cdot}10^{-2}$	5 581	$0.10{\cdot}10^{-2}$
22	1.05	4 930	$0.38{\cdot}10^{-2}$	25 307	$0.17{\cdot}10^{-2}$
24, 25		5 040	$0.37{\cdot}10^{-2}$	27 228	$0.16{\cdot}10^{-2}$
15, 16		5 571	$0.34{\cdot}10^{-2}$	25 204	$0.16{\cdot}10^{-2}$
10		3 177	$0.33{\cdot}10^{-2}$	19 127	$0.14{\cdot}10^{-2}$
31, 32, 46, 48		3 699	$0.20{\cdot}10^{-2}$	5 671	$0.12{\cdot}10^{-2}$
29	NaF	1 142	$1.3\ {\cdot}10^{-2}$	4 133	$0.81{\cdot}10^{-2}$

Table 5.6: *Velocity resolution estimation for the cosmic runs. $\widehat{\delta\beta}$ is the estimator of the β resolution.*

5.6 Light Yield

In this final section, an attempt to analyze and compare the light yields of the different radiators is performed. Light Yield is here used in a more broad sense than the intrinsic radiator light yield that only accounts for the production of Cherenkov photons (see eq. 2.2). In this study, only the detected photons can be used to evaluate the radiator light yield. By means of an appropriated efficiency correction, the number of hits on the reconstructed ring is a fair measure of the radiator light yield.

Besides the velocity dependence of equation 2.2, there is also the ring acceptance[4] that matters to determine the number of photons to be detected in a RICH event. Observing the plots of fig. 5.39 (page 116 at the end of this section), where the computed ring acceptances spectrum are plotted against the reconstructed velocities for the muons RICH events, one figures out the difficulty to give a reference value for the mean number of hits for each run.

If all the runs had the same *acceptance-velocity spectra*, and the same efficiency reconstruction, one could directly compare the average of the number of hits on the reconstructed rings obtained with the different radiators. Once this is not feasible, one has to disentangle the number of hits from the acceptance and the velocity.

The reference value will be an estimation of the light yield for the limit velocity ($\beta = 1$) and a ring acceptance of 100%, called $\mu_{(1,1)}$ from now on. This will not be done by selecting the events on these reconstructed variables, due to the lack of statistics for the above reference values, and even nonexistence at all of such events on runs 10, 31-48 (n=1.05) and 29. Instead of that, the procedure next described was used.

In principle, the histogram for the number of hits for each run results from the combination of Poisson distributions intrinsic to each acceptance-velocity configuration (α, β) with different weights (see figure 5.34).
The mixture of these Poisson distributions is expressed by the following relation

$$P(n) \propto \int\int \quad \frac{\partial^2 N}{\partial\beta\,\partial\alpha} \quad Poiss(n;\mu_{\{\beta,\alpha\}}) \quad \mathrm{d}\alpha\,\mathrm{d}\beta \tag{5.1}$$

$$\text{with } \mu(\beta,\alpha) = \mu_{(1,1)}\,\frac{f(\beta)}{f(\beta=1)}\,\alpha\ .$$

[4]The Ring acceptance is a measure of the fraction of emitted photons that end in a detectable area. For a detailed description of the ring acceptance calculation, refer to [16]

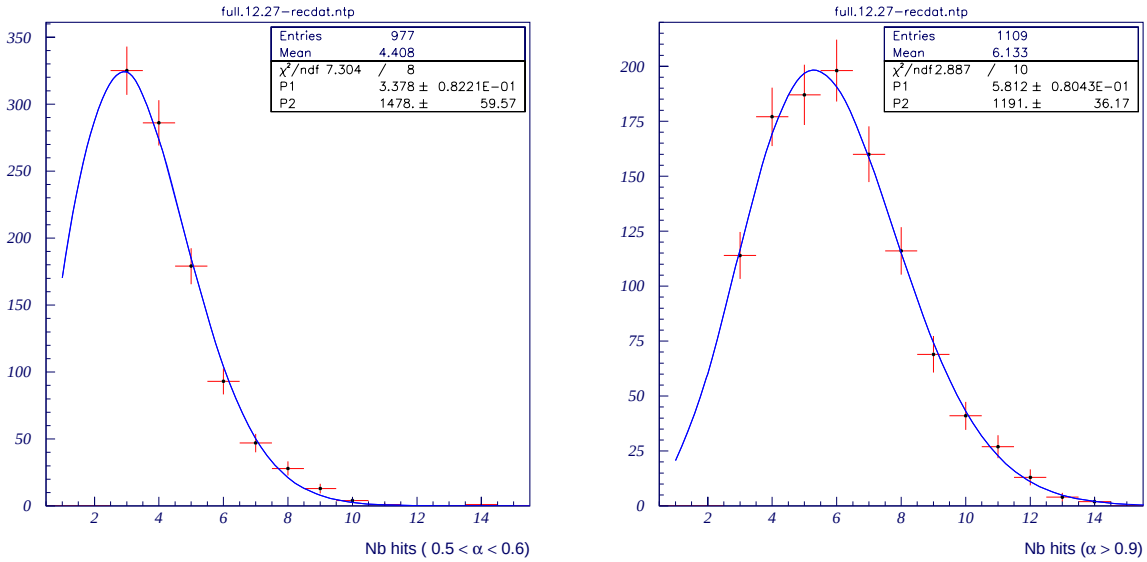

Figure 5.34: *Number of hits for two acceptance-velocity configurations and respective Poisson fits (data runs 12-27). Left:* $0.5 < \alpha < 0.6$ *Right:* $0.9 < \alpha < 1.0$ *($\beta^{rec} > 0.999$ for both configurations)*

This gives the final distribution function $P(n)$ as a function of the usual Poisson distribution function $Poiss(\mathrm{n};\mu) = \dfrac{\mu^{\mathrm{n}}\, e^{\mu}}{n!}$ with mean value μ. This mean value depends on the velocity (β) and the ring acceptance (α) by the above scaling relation $\mu(\alpha,\beta)$ where $f(\beta)$ is the factor $(1-(n\beta)^{-2})^{-1}$ of equation 2.2.

The different Poissons are weighted by the p.d.f. function $\dfrac{\partial^2 N}{\partial\alpha\partial\beta}$ associated to the biplots of fig. 5.39. In practice, the integrals are substituted by sums and the continuous p.d.f. by indexed weights W_{ij}, leading to the following 2 parameters **fit-model**:

$$P(n) = N_0 \sum_{i,j} W_{ij}\, Poiss(n,\mu_{ij}) \qquad (5.2)$$

$$\text{with}\quad \mu_{ij} = \mu_{(1,1)} \frac{f(\beta_i)}{f(\beta=1)}\,\alpha_j\ ,$$

where the weights W_{ij} are directly taken from the acceptance-velocity spectra of figure 5.39 and the fit parameters are N_0 and $\mu_{(1,1)}$.

Given its meaning, the ring acceptance factor (α) in the scaling law of 5.1 is natural and it is fairly supported in view of the plot of fig. 5.35, where the events were separated into different acceptance populations and a Poisson fit was performed to obtain the mean number of hits for each acceptance section - see fig. 5.34.

The linearity is well established, despite the constant parameter of the linear fit being significantly different from zero.

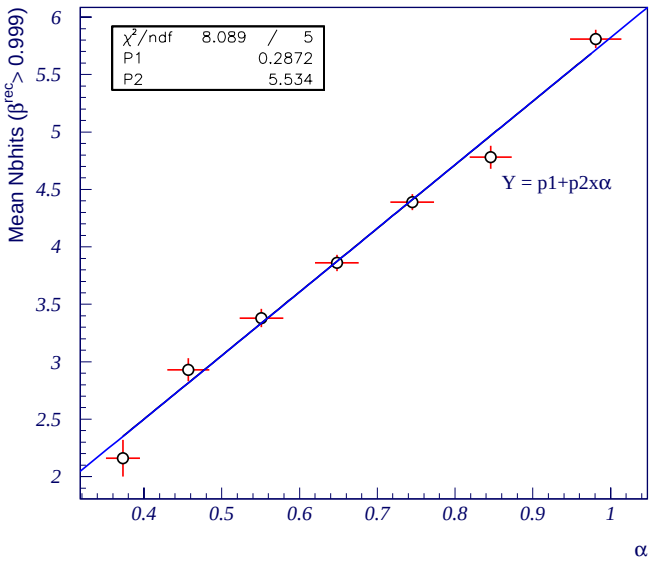

Figure 5.35: *Mean number of hits for different acceptances of run 12-27 (data). The means correspond to Poisson Fits of the respective histograms.*

So, applying the fit of eq. 5.2, one gets the next fits of figure 5.37, with the results summarized in figure 5.36 and table 5.7 (page 113).

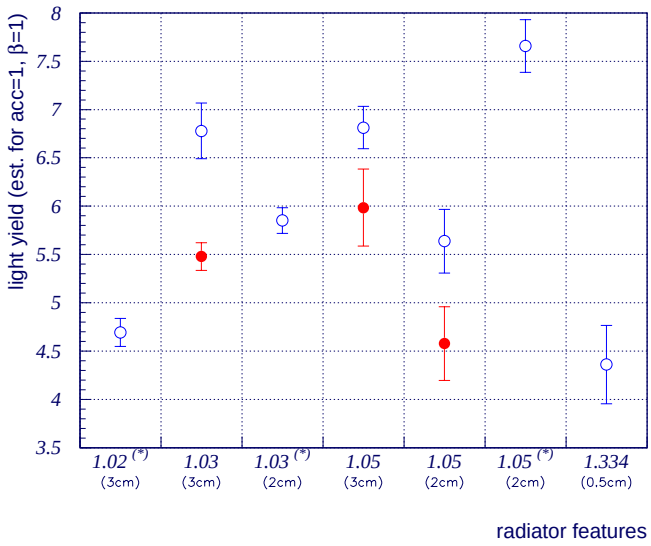

Figure 5.36: *Results for the light yield estimator for the different radiators. Full dots represent runs with the plastic foil present under the radiator, and hollow without. The aerogel radiators signaled with (*) are different samples.*

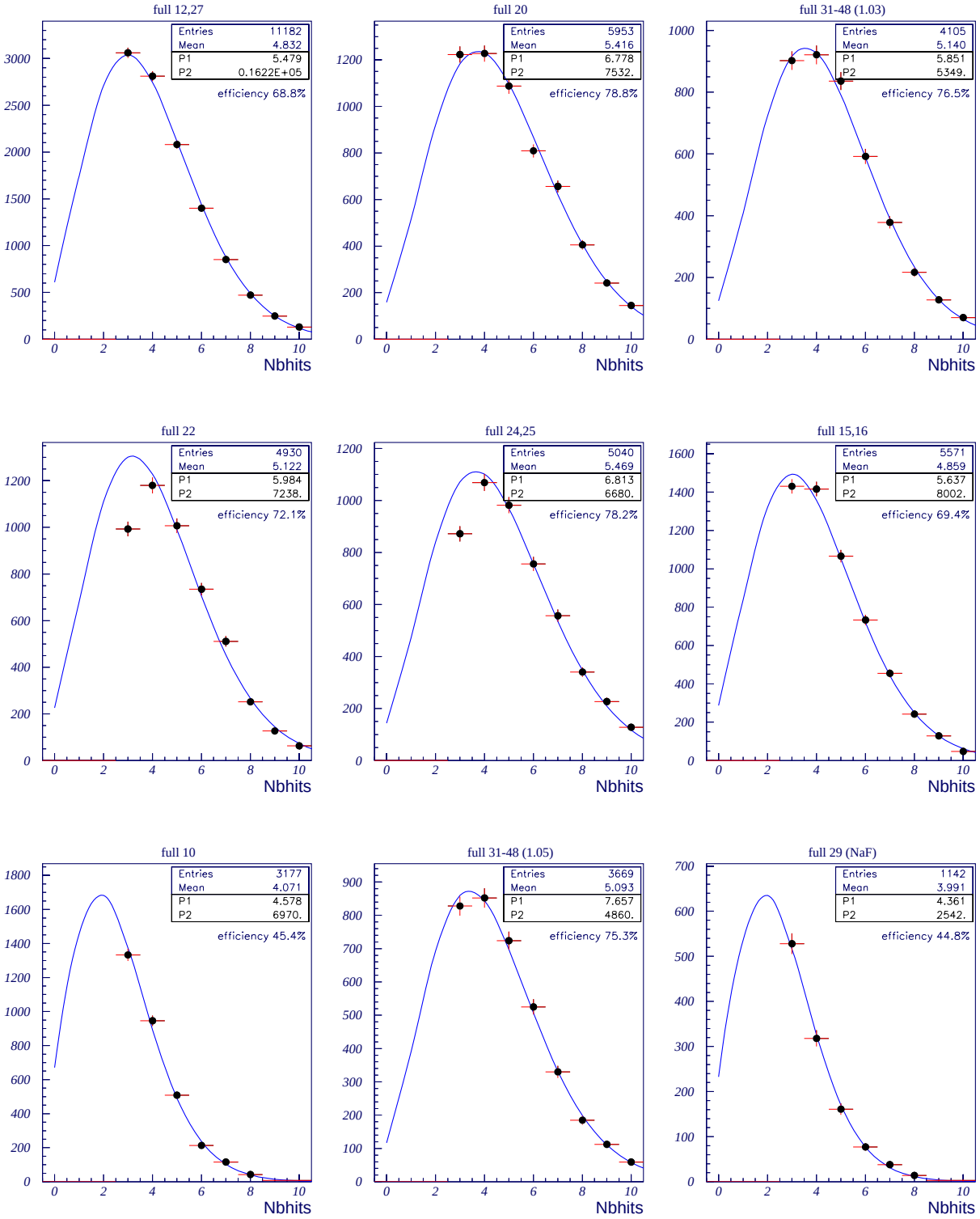

Figure 5.37: *Fits to the ring hits counting distributions for the data runs, using model of eq. 5.1. The 1st bin has not been considered for fits of runs 22 and 24-25.*

RUN	Radiator		Foil	$\mu_{(1,1)}$	χ^2/ndf	Number reconst.	Efficiency %
	index	thick. (cm)					
31, 32, 46, 48 [(a)]	1.02	3	No	4.7 ± 0.1	0.6	478	75.9 ± 1.0
12, 27	1.03	3	Yes	5.5 ± 0.1	2.1	11 182	68.8 ± 1.4
20		3	No	6.8 ± 0.3	1.1	5 953	78.8 ± 2.0
31, 32, 46, 48 [(a)]		2	No	5.9 ± 0.1	0.8	4 105	76.5 ± 1.0
22	1.05	3	Yes	6.0 ± 0.4	1.4	4 930	72.1 ± 3.4
24, 25		3	No	6.8 ± 0.2	1.4	5 040	78.2 ± 1.3
15, 16		2	No	5.6 ± 0.3	1.3	5 571	69.4 ± 1.8
10		2	Yes	4.6 ± 0.4	2.4	3 177	45.4 ± 2.9
31, 32, 46, 48 [(a)]		2	No	7.7 ± 0.3	0.8	3 699	75.3 ± 1.7
29	NaF	0.5	No	4.4 ± 0.4	0.6	1 142	44.8 ± 2.6

Table 5.7: *Light Yield table summary.* $\mu_{(1,1)}$ *is the estimator of the mean number of hits for events of 100% acceptance and velocity* $\beta = 1$. *Efficiency is defined as the fraction of events that give at least 3 hits.*

A note on the presented error is worth to mention. This accounts not only for the statistical fit error but also for a kind of systematic error of the method.

This *systematic* error should be understood as a measure of a certain degree of disagreement between the used fit model and the fitted distributions.

In order to avoid the errors present on the data acceptance-velocity spectra, the corresponding simulation spectra have been used to provide the weights W_{ij}, instead of the data runs spectra. However, due to a possible slight discrepancy between the acceptance-velocity spectra of data and simulation, both spectra have been used on the fit, in order to estimate the error introduced in the method. When using the smooth simulated spectra, the result of the fit is fairly independent of the chosen bin; the same is not completely true about the data spectra.

On the other hand, in the case of the real data, the counting of the ring hits may be affected by some amount of noisy hits that can randomly appear into the ring. In particular, this background must be of worst effect in the case of reconstructions with the acceptance threshold value of 3 hits compared to the others. In fact, in two of the data runs - runs 22 and 24,25 - this bin has been removed from the fit (see 1st point of 4^{th} and 5^{th} plots in fig. 5.37). Due to these possible sources of

divergence between the fit model and the data, the error of this fit procedure has also been evaluated by doing the fit to different samplings of the total hits counting histogram and measuring the difference on the final result. The two last procedures have been used to evaluate the systematic error of the light yield fit.

Another advantage of this fit technique is to allow to infer the expected distribution for the number of hits bellow the "3 hits threshold". This way, one can define efficiency as the fraction of the events having at least 3 hits. These efficiencies are plotted in next fig. 5.38.

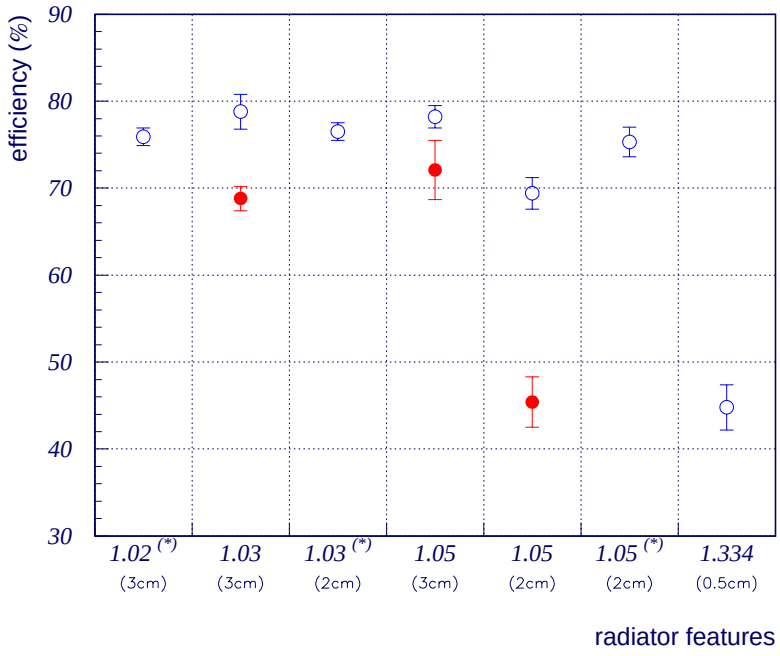

Figure 5.38: *Efficiency of having at least 3 hits (result for the different radiators obtained by the fit of eq. 5.1). The full and hollow dots have the same meaning of fig. 5.36 and so it goes for the radiators signaled with (*).*

To conclude this section and this analysis, let us take some final notes. By the reading of the comparative light yield plot of figure 5.36, one would be compelled to choose the Aerogel radiator (n=1.05) used in runs 31-48 indicated with $1.05^{(*)}$ in the horizontal axis labels, with a mean number of almost 8 hits. However, having in mind the resolution results of figure 5.32, the choice of the 1.03 aerogel radiator sample of runs 31-48 (label $1.03^{(*)}$) may be the best, given the fact that the efficiencies in question are quite comparable (about 75%, see fig. 5.38).

On the effect of the thickness and foil the following conclusions are clear. The foil neatly decreases the light yield (and the efficiency) by a significant amount, although not the same for the different radiator runs. For radiators 1.03 (3cm) and 1.05(2cm), the decreasing effect in the light yield is of about 18%, while for the radiator 1.05(3cm) it is only about 12%. The thickness also has an important role in the light yield. For the radiator 1.03, the light yield is increased by about 18%, when thickness goes from 2cm to 3cm. For the radiator 1.05, two situations occur, with foil and without foil. The radiator thickness seems to be more critical when the absorbing effect of the foil is present. With foil the light yield increase is of about 30%, whithout it is only of about 20%. We note however that the plastic foil to be used in the final detector has lower absorption characteristics than the one here used.

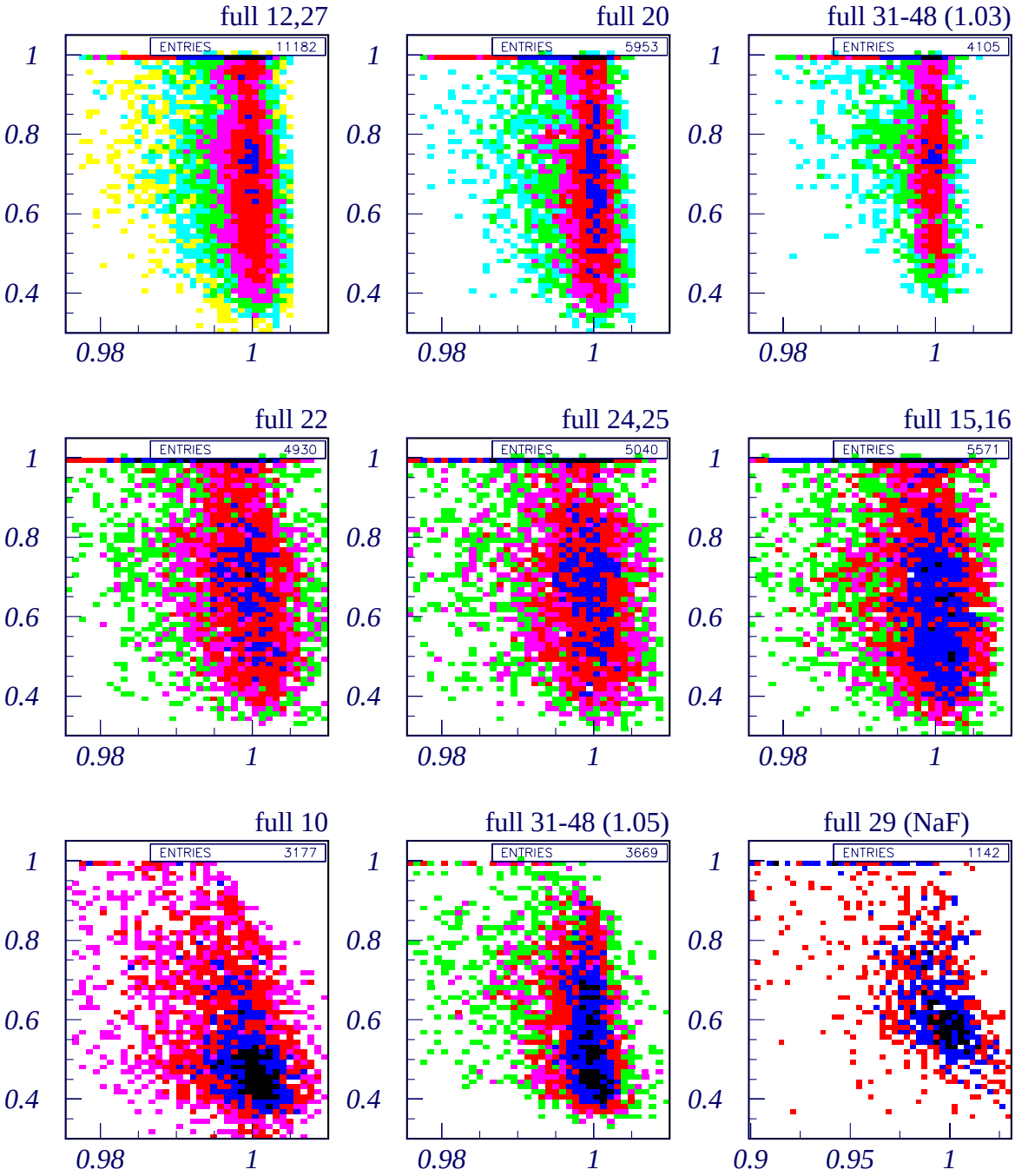

Figure 5.39: *Palette of scatter-plots "Ring acceptance (in y scale) versus $\beta_{\rm rec}$" for all the data runs. The bin occupancy increases from lighter to darker colors.*

Conclusions

In this work, an effective reconstruction algorithm has been presented. This algorithm has been successfully tested on both simulated and real data. On the simulated data, the algorithm has achieved the expected *single hit* velocity resolution of about 2×10^{-3} (asymptotic value for $\beta \simeq 1$) in the case of an Aerogel radiator.

The reconstruction algorithm has allowed to analyze a series of cosmic data runs used to perform the first "real conditions" tests to the the AMS RICH prototype. From this analysis it is worthwhile to mention that for the same radiator thickness, aerogel 1.03 gives roughly a resolution twice better than aerogel 1.05. In the meanwhile, the RICH prototype has already been tested on beam at CERN, with new aerogel radiators that seem to be better than the ones here studied.

This algorithm has nonetheless an unpleasant feature.It has to do with the successive minimizations performed to reconstruct one event, that make the algorithm computationally heavy and somehow slow. A goodness-of-fit statistical test is still not yet implemented in the reconstruction/analysis software. The implementation of an effective test could perhaps improve the results as it has been observed on the cosmic run data that a lot of noise seems to be present. It would be good if it can be eliminated. As a additional remark, we note that the rigorous effect of a non perfectly specular mirror on the spreading of the ring photons is still unknown. Yet, because of the high requisites asked to the manufacturer, it is expected to be a negligible effect.

Appendix A

Refraction effect on the θ_C geometrical resolution

In the vertical particle incidence case of next figure, we depict the refraction of the Cherenkov photons in the radiator-air interface, where the Snell relation takes place:

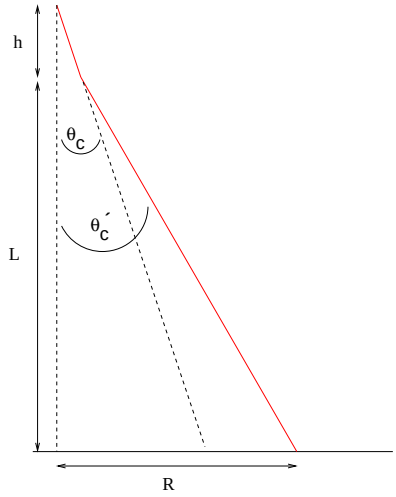

$$n \sin\theta_c = \sin\theta\,'_c.$$

An exact equation relating the Cherenkov ring radius R to the Cherenkov angle θ_c can be written as:

$$\left(h + \frac{n\ L}{\sqrt{1 + (1 - n^2)\ \tan^2\theta_c}}\right) \tan\theta_c = R\ .$$

This equation takes into account the refraction effect on the radiator-expansion volume interface. Taking $n = 1$ necessarily leads us to the case where refraction is neglected. In the NaF case ($n = 1.334$), this factor is relevant, as one can conclude for instance by the comparison of the graphics of the functions $R(\theta_c)$ computed when one takes refraction into account and when not (see fig. A.1).

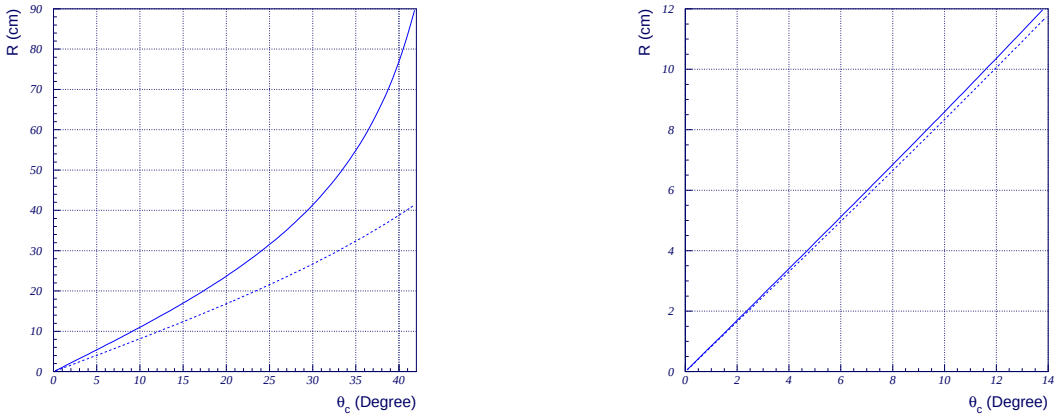

Figure A.1: *Effect of the refraction on the radius of the Cherenkov ring for a vertical particle incidence. Full line function neglects refraction effect, dashed line function doesn't.* Right*: NaF radiator (5mm thickness);* Left *Aerogel radiator (3cm thickness)*

When differenciating previous relation, one obtains the following expression:

$$\delta\theta_c \;=\; \cos^2\theta_c \;\; \frac{\delta R}{n\,\mathcal{R}(\theta_c)\,L + h}$$

$$\text{with}\;\; \mathcal{R}(\theta_c) \;=\; \frac{1}{\sqrt{1+(1-n^2)\tan^2\theta_c}} - \frac{(1-n^2)\tan^2\theta_c}{(1+(1-n^2)\tan^2\theta_c)^{\frac{3}{2}}}$$

Neglecting the refraction effect, one would end up with the same expression, but with $\mathcal{R}(\theta_c) = \text{constant} = 1$. The effect of this non-constant correction factor is illustrated in the following figure, where the resolution on θ_c coming from the geometrical sources is plotted when refraction is neglected (dashed line)and when taken into account (continuous line). This illustration is for the NaF radiator, where the correction is significant.

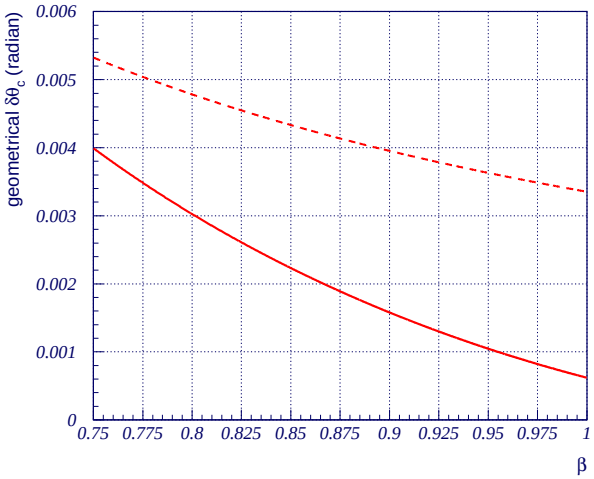

Figure A.2: *Effect of refraction on the θ_c geometrical resolution.*

Appendix B

Photon's crossed distance inside RICH radiator

The derivation of formula 2.11 is here given in two different ways. The first derivation is less straight-forward than the second, but is still included for pedagogical reasons. Besides, both derivations follow from a common ground that consists in using two coordinate systems. One is the RICH cartesian frame, the other is a cartesian frame attached to the particle trak.

The problem consists in computing the distance $d(\varphi)$ indicated in figure B.1. This corresponds to the distance that a photon emitted at the radiator top travels down to its bottom (radiator thickness $= h$). In the particle reference frame, the parametric equations for a point P belonging to the surface of the cone are given by:

$$P(d,\varphi) = \begin{cases} x' = d\ \sin\theta_c\ \cos\varphi \\ y' = d\ \sin\theta_c\ \sin\varphi \\ z' = d\ \cos\theta_c \end{cases} \qquad \text{(B.1)}$$

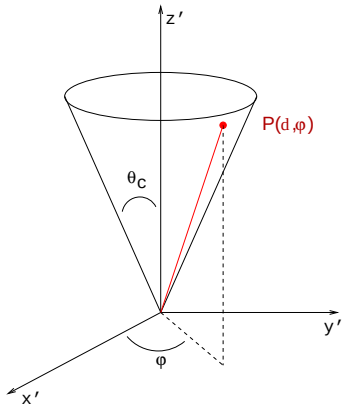

where d is obviously the distance between P and the origin ($d = \|\vec{P}\|$).

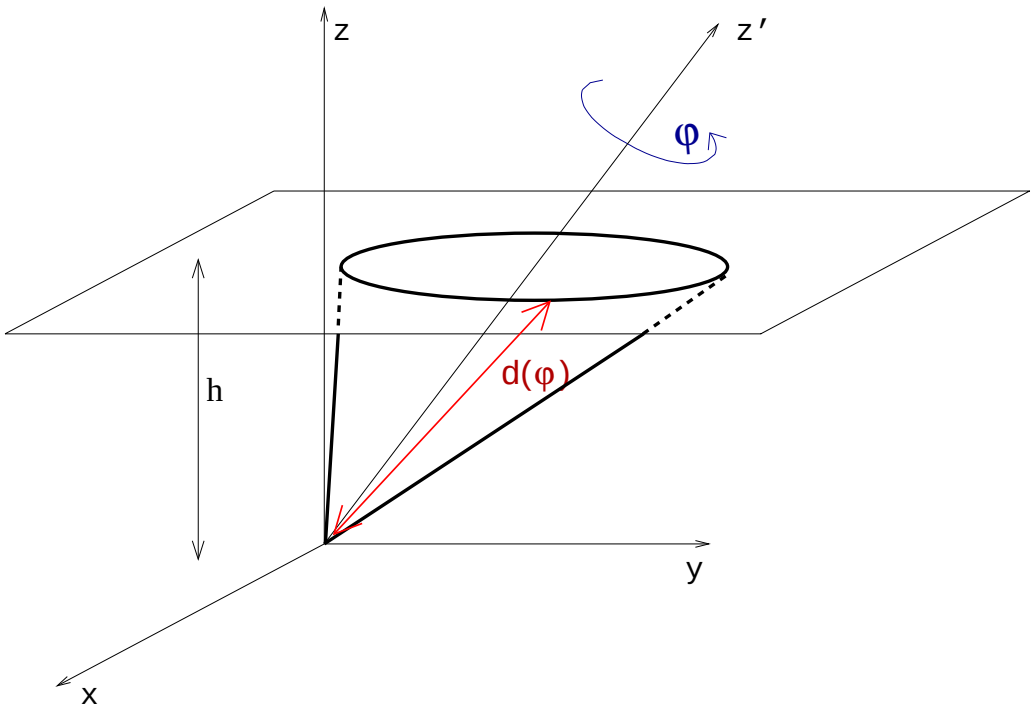

Figure B.1: *Distance crossed by a photon emitted at the top of the radiator inside it. The pretended distance, $d(\varphi)$, corresponds to the intersection of the Cherenkov cone with the plane $z = h$. The cone has a semi-aperture angle θ_c, and its axis directed along the particle direction (θ,ϕ).*

The transformation for the coordinates of a point given in the particle reference frame (x', y', z') into the outside reference frame (x, y, z) is given by [1]:

$$\begin{pmatrix} x \\ y \\ z \end{pmatrix} = \begin{pmatrix} -\cos\theta\cos\phi & \sin\phi & \sin\theta\cos\phi \\ -\cos\theta\sin\phi & -\cos\phi & \sin\theta\sin\phi \\ \sin\theta & 0 & \cos\theta \end{pmatrix} \begin{pmatrix} x' \\ y' \\ z' \end{pmatrix} \tag{B.2}$$

[1] This transformation matrix corresponds (without any loss of generality) to the choice of having the axis y' belonging to the plane xOy. For a derivation of this, see for instance chapter 4 of reference [16]

first proof:

Inserting conditions $z = h$ and (B.1) into relation (B.2), one gets a set of simultaneous linear equations in the variables $\{d, x, y\}$ depending on the parameters $\{\theta_c, \theta, \phi, \varphi\}$:

$$\begin{pmatrix} \sin\theta_c \cos\varphi & \cos\theta\cos\phi & \cos\theta\sin\phi \\ \sin\theta_c \sin\varphi & -\sin\phi & \cos\phi \\ \cos\theta_c & -\sin\theta\cos\phi & -\sin\theta\sin\phi \end{pmatrix} \begin{pmatrix} d \\ x \\ y \end{pmatrix} = \begin{pmatrix} h\sin\theta \\ 0 \\ h\cos\theta \end{pmatrix}$$

with the following solution for $d(\varphi)$:

$$d(\varphi) = \frac{h}{\cos\theta\cos\theta_c + \sin\theta\sin\theta_c\cos\varphi}$$

second and much more straightforward proof:

In the next reasoning, one gets $d(\varphi)$ as being given by $\dfrac{h}{\cos\theta_i}$, where θ_i is the angle of the photon with respect to the normal (This θ_i obviously has a dependence on φ). Dividing parametric eq. B.1 by the unknown distance $d(\varphi)$, one obtains the components of the unit vector for the photon direction in the particle frame ($\vec{u'}$). Applying the rotation transformation to this unit vector, one obtains the same unit vector expressed in the RICH frame ($\vec{u}$). In particular the z component is transformed according to:

$$\begin{aligned} u_z &= \sin\theta\ u'_x + \cos\theta\ u'_z \\ &= \sin\theta\sin\theta_c\cos\varphi + \cos\theta\cos\theta_c \end{aligned}$$

As $\vec{u}$ is a unit vector, the pretended director cosine $\cos\theta_i$ corresponds exactly to u_z.

Bibliography

[1] K.H. Kampert. *astro-ph/0101331*, 2001.

[2] Balebanov et al. AMS proposal to DOE, approved, April 1995.

[3] S.P. Ahlen et al. An antimatter spectrometer in space. *NIM-A (Nucl. Instrum. and Methods in Physics Research A)*, 350:351–367, 1994.

[4] http://lheawww.gsfc.nasa.gov/docs/balloon.

[5] Sakharov, A.D. *JETP Lett.*, 5:24, 1967.

[6] A.G. Cohen et al. A matter-antimatter universe? *the Astrophysical Journal*, 495:539–549, 1998.

[7] Hagiwara et al. Review of Particle Physics. *Physical Review D*, 66:010001, 2002.

[8] F. Donato. Antideuterons as a signature of supersymmetric dark matter. *Phys. Rev. D*, 62(4), July 2000.

[9] Lukasiak et al. *the Astrophysical Journal*, 423:426–431, 1994.

[10] S.C.C. Ting. Experimental results and future opportunities in Particle Physics. *Physics Reports*, 279:203–250, 1997.

[11] AMS collaboration. The Alpha Magnetic Spectrometer (AMS) on the International Space Station: Part I – results from the test flight on the space shuttle. *Physics Reports*, 366:331–405, 2002.

[12] I. Tamm and I. Frank. *Compt. Rend. Acad. Sci. USSR*, 14:109, 1937.

[13] G. Barbiellini et al. Performance of the CAPRICE RICH detector during the 1994 balloon flight. *Nuclear Instruments & Methods in Physics Research - section A*, 371:169–173, 1996.

[14] G.Poelz, R.Riethmüller. Preparation of Silica Aerogel for Cherenkov counters. *Nuclear Instruments and Methods*, 195:491–503, 1982.

[15] E.Nappi. Aerogel and its applications to RICH detectors. *Nucl. Physics – Proceedings Suplements*, 61:270–276, 1998.

[16] Maria L. Arruda. Čerenkov Ring Acceptance in the RICH detector of the AMS experiment (Optimization of a Dual Radiator Configuration). Master's thesis, I.S.T, Portugal, 2003.

[17] Hamamatsu Photonics (http://www.hamamatsu.com).

[18] http://wwwae.ciemat.es/ams.

[19] W.Vanghan W.G.Driscoll. *Handbook of Optics*. McGraw Hill, New York, 1995.

[20] Glen Cowan. *Statistical Data Analysis*. Oxford University Press, 1998.

[21] Willian R. Leo. *Techniques for Nuclear and Particle Physics Experiments*. Springer-Verlag, 1987.

[22] Peter K.F. Grieder. *COSMIC RAYS AT EARTH-Researcher's Reference Manual and Data Book*. Elsevier, 2001.

[23] John R. Taylor. *An introduction to Error Analysis, 2nd edition*. University Science Books, 1997.